Dynamics of Electron Beam and Dark Current in Photocathode RF Guns

Dissertation
zur Erlangung des Doktorgrades
des Fachbereichs Physik
der Universität Hamburg

vorgelegt von
Jang-Hui Han
aus Seoul

Hamburg
2005

Gutachter der Dissertation:	Prof. Dr. J. Roßbach Prof. Dr. W. Wurth
Gutachter der Disputation:	Prof. Dr. J. Roßbach Prof. Dr. P. Schmüser
Datum der Disputation:	4.11.2005
Vorsitzender des Prüfungsausschusses:	Prof. Dr. G. Heinzelmann
Vorsitzender des Promotionsausschusses:	Prof. Dr. G. Huber
Dekan des Fachbereichs Physik:	Prof. Dr. G. Huber

Abstract

The emission processes of electron beams from Cs_2Te photocathodes have been experimentally studied at the photoinjector test facility at Zeuthen (PITZ) and the results have been compared with simulations. Low charge electron beams have been generated in order to minimize the space charge influence. Drive-laser pulses with a short length have been used to generate the bunches in order to maximize the emission phase sensitivity. As a function of emission phase and rf gradient, the Schottky effect, the thermal emittance variation, and the secondary electron emission processes have been investigated. The results for the low charge beams have been extended to analyze the beam dynamics for typical operating conditions of PITZ. Characteristic field emission sources for dark current and its dynamics with respect to the rf gradients and the solenoid field configurations have been studied. Electron multipacting occurring at the photocathode has been measured systematically and the multiplication process has been numerically modeled. Finally, the thermal emittance of the beam, dark current and multipacting for the X-ray free electron laser (XFEL) gun have been estimated.

Zusammenfassung

Die Emissionsprozesse von Elektronenstrahlen aus Cs_2Te Photokathoden wurden am Photoinjektor Teststand in Zeuthen (PITZ) experimentell untersucht und die Ergebnisse wurden mit Simulationen verglichen. Elektronenstrahlen mit geringer Ladung wurden erzeugt, um den Einfluss der Raumladung zu minimieren. Zur Erzeugung des Strahls wurde ein Photokathodenlaserpuls mit einer kurzen Pulslänge verwendet, um die Empfindlichkeit der Dynamik zur Emissionsphase zu maximieren. Der Schottky-Effekt, die Änderung der thermische Emittanz und die Emissionsprozesse von Sekundärelektronen wurden als Funktion der Emissionsphase und des HF-Gradienten untersucht. Die Ergebnisse mit niederenergetischen Strahlen wurden erweitert, um die Strahldynamik für typische Betriebsbedingungen von PITZ zu analysieren. Charakteristische Feldemissionsquellen von Dunkelstrom und ihre Dynamik hinsichtlich der HF-Gradienten und der Feldkonfiguationen der Solenoiden wurden untersucht. An der Photokathode auftretendes Elektronenmultipacting wurde systematisch gemessen und der Vervielfachungsprozess wurde numerisch modelliert. Abschließend wurden die thermische Emittanz des Strahls, Dunkelstrom und Multipacting für die Elektronenkanone des Freie-Elektronen-Röntgenlasers (XFEL) abgeschätzt.

Contents

1 Introduction **1**

2 Experimental setup **5**
2.1 Components for electron beam generation 6
2.1.1 RF cavity 6
2.1.2 Photocathode 6
2.1.3 Drive-laser 7
2.1.4 Solenoids 8
2.2 Diagnostics 9
2.2.1 Drive-laser measurement 9
2.2.2 Electron beam measurements 9

3 Physics of electron emission **11**
3.1 Field emission 11
3.2 Photoemission 17
3.3 Secondary emission 23

4 Effective emission mechanisms **27**
4.1 Low charge beam dynamics 27
4.1.1 Single electron dynamics 28
4.1.2 Electron beam dynamics 34
4.1.3 Secondary emission in electron dynamics 37
4.1.4 Effective photoemission for low charge beams 44
4.2 Beam dynamics for normal operating conditions 51
4.2.1 Beam dynamics dependence on emission phase 51
4.2.2 Effective electron emission for high charge beams 53
4.2.3 Effective emission at the optimum phase 54

5 Dark current **57**
5.1 Dark current source 58
5.1.1 Trajectories of the field-emitted electrons 58
5.1.2 Empirical approach of source characterization 61
5.2 Momentum spectrum 66
5.3 Dependence on the solenoid field 67

5.4 Dependence on the states of cathodes and cavities 73
5.5 Dark current history 77

6 Multipacting **79**
6.1 Measurements 81
6.1.1 General description of observations of multipacting 81
6.1.2 Dependence on the maximum rf field 82
6.1.3 Dependence on the solenoid setting 85
6.2 Model of the mechanism 89
6.2.1 Electron dynamics at low rf field strength 90
6.2.2 Electron dynamics at low rf field strength and solenoid field . 91
6.2.3 Multiplication of the field-emitted electron 93

7 XFEL gun **97**
7.1 Requirements 97
7.2 Thermal emittance 98
7.3 Dark current 98
7.4 Multipacting 102

8 Conclusion **103**

A Cathodes parameters **105**
A.1 Specifications 105
A.2 Aging of cathodes 106

B An approximation of the Nordheim parameter **111**

Acknowledgments **119**

Chapter 1

Introduction

When charged particles with a relativistic speed travel on a curved path, electromagnetic radiation is emitted into the tangential direction of the trajectory. This is known as synchrotron radiation. Electrons circulating in a storage ring with an energy higher than about 2 GeV, produce intensive radiation over a broad range of wavelengths extending from the infrared to hard X-rays in the electromagnetic spectrum (for instance, PETRA II at DESY, BESSY II, PLS at PAL, SLS at PSI, etc.). Synchrotron radiation is a powerful tool for studies in molecular biology, surface science, medicine, geology, chemistry, physics, and also for technologies like X-ray lithography, micro-machining, and nano-structure analysis. Very narrow spectra can be amplified by an undulator inserted into the storage ring.

In Free-Electron Lasers (FELs), an electron beam radiates photons by transverse oscillations in an undulator and interacts with the radiation emitted by the beam itself. In the process of coherent interactions between the beam and the radiation, the radiation becomes highly directional and is stimulated into a narrow frequency band. In combination with a linear accelerator (linac), an FEL can generate shorter and brighter radiation by self-amplified spontaneous emission (SASE), because linacs do not have a limitation of the beam emittance caused by quantum fluctuation [1]. In SASE FELs, the achievable wavelength of the coherent radiation is defined by the beam emittance [2].

Photocathode rf guns have been proven to be excellent electron sources for very high quality beams required for vacuum ultra-violet (VUV) and X-ray FELs [3, 4]. In photocathode rf guns, electron beams are generated at the photocathode by the drive-laser pulses and they are accelerated immediately by the rf field in the gun cavity. Since the electron bunches after emission from the photocathode are of very high density and have a velocity close to zero, the beam quality gets worse due to the high space charge force. The beam quality can be optimized by means of a laser pulse with a well-defined three-dimensional (3D) profile, which is composed of the two transverse and one temporal directions. Therefore, the expansion and non-linearity of the electron bunch in the phase space can be minimized with the optimized initial electron distribution. The initial profile of the beam after extraction

from the cathode undergoes a modification under the rf and the solenoid fields as well as the space charge force.

The electron beam dynamics after extraction from the cathode can be understood analytically [5, 6] and numerically with simulation codes like ASTRA [7] and PARMELA [8]. On the other hand, electron emission processes from the Cs_2Te photocathode under the rf gun operation conditions are not fully understood because the emission processes must be studied with a strong electric field of the order of 10 MV/m but there is no state-of-the-art instrument for that purpose yet. Since the emission processes cannot be monitored directly in the gun cavity, the properties of the accelerated beams have been studied in order to extract the information of the emission processes of the beam.

Due to the strong accelerating field in the gun cavity, electrons can be field-emitted from the copper cavity surface and the photocathode. This is called dark current. Dark current at the gun can be accelerated together with the electron beams and make severe hazards, radiational activation and even mechanical damage, to vacuum components like diagnostic systems and undulator sections. The amount of dark current can be reduced with rf conditioning. Nevertheless, due to a maximum rf pulse length of several hundreds μs, the amount of dark current emitted with 1.3 GHz might be comparable to the electron beam which has a repetition rate of only 1 MHz in the rf pulse. Even after conditioning, a new field emitter can appear. For example, exchanging the cathodes may make new scratches on the side of the cathode plug and the scratches behave as new strong field emitters. Any unexpected dusts on the front surface of the cathode may be strong field emitters as well. Therefore, critical dark current sources and the dark current dynamics have to be investigated.

During gun operation, multipacting peaks are found at the beginning and/or at the end of the rf pulses. The multipacting depends strongly on the solenoid field profile. In order to control the multipacting, the point where the multipacting takes place and the multiplication process have to be found.

In this thesis, effective electron emission processes in the photocathode rf guns at PITZ are discussed. In Chap. 2, the experimental setup for the beam generation and diagnostics is described. In Chap. 3, three electron emission processes from solid, i.e. field emission, photoemission and secondary emission, are reviewed.

In Chap. 4, effective photoemission and secondary emission processes in the photocathode rf gun cavity are studied. First, in order to compare the measurements to simulation, single electron dynamics is numerically studied. Second, the information of the single electron dynamics is applied to the analysis of the electron beam which has a short initial pulse length and a small bunch charge. With the small bunch charge, the space charge force influence on the beam dynamics can be minimized. With the short bunch length, the emission phase sensitivity can be maximized, where the emission phase is defined as the rf phase when electrons are emitted from the photocathode. With these conditions, secondary electron emission, the Schottky effect and thermal emittance of the Cs_2Te photocathode are discussed. Finally, the results of the low charge beams studies are extended to analyze the beam dynamics

for typical operating conditions of PITZ.

In Chap. 5, measurements of dark current are shown in order to find the characteristic source. The dark current strength is measured with changing machine parameters like the rf gradient and the solenoid field configuration. The dependence on the photocathode and on the gun cavity are also shown.

In Chap. 6, electron multiple impacting (multipacting) occurring in the photocathode rf gun is measured systematically. Then, the multiplication process is modeled numerically.

In Chap. 7, the thermal emittance of the beam, dark current and multipacting for the XFEL gun are estimated with considering the discussion of the previous chapters.

Chapter 2

Experimental setup

The experiments presented in this thesis have been performed at the Photo Injector Test Facility at DESY in Zeuthen (PITZ) [9]. The aim of PITZ is to develop electron sources which can produce high density electron beams with small transverse emittance and short bunch length as required for FEL operation. The gun and the downstream beamline with the diagnostic components are schematically shown in Fig. 2.1. The setup consists of a 1.5 cell rf Cu gun cavity, a coaxial rf coupler, two solenoids for emittance preservation, a photocathode with a cathode plug made from molybdenum, a drive-laser with a wavelength of 262 nm, and various diagnostics components. The Mo cathode plug is partially covered with a photoemissive Cs_2Te film on the front surface. The transversal and temporal profiles of the drive-laser beam pulse are adjustable.

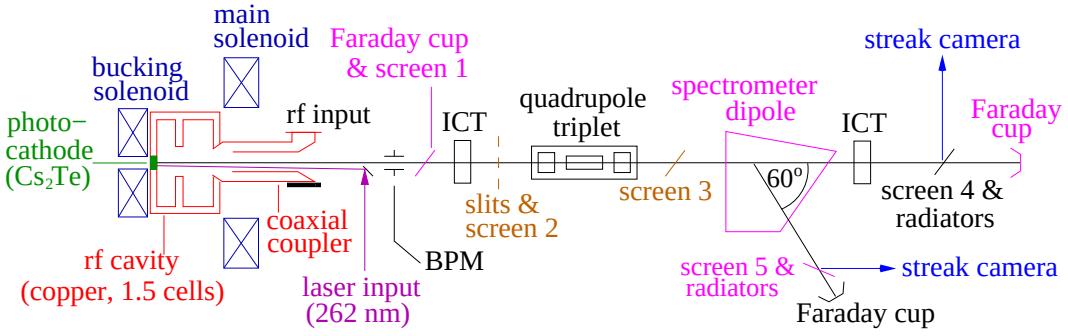

Figure 2.1: Schematic view of the gun and diagnostic sections.

2.1 Components for electron beam generation

2.1.1 RF cavity

A 1.5 cell copper cavity is used to accelerate the electrons emitted from the photocathode. The geometry of the PITZ gun cavity is shown in Fig. 5.2 with the rf field distribution. The gun cavity is operated at a resonance frequency of 1.3 GHz. The rf input coupler transfers rf power from the klystron (through the waveguide) into the gun cavity. The gun cavity and the coupler components are designed to have a perfect cylindrical symmetry in order to avoid dipole or higher order fields in the cavity. Asymmetry of the rf field may increase the beam emittance [10].

The first PITZ gun cavity named prototype #2 was used in 2002 and 2003. The cavity was commissioned to operate with 900 μs long rf pulses at 10 Hz repetition rate and an rf gradient at the cathode of 42 MV/m. This cavity has been installed and is presently used for the operation of the VUV-FEL at the TESLA Test Facility (TTF2) at DESY in Hamburg. A second rf gun cavity dating from an earlier production with almost same geometry (called prototype #1) has been installed at PITZ in January 2004 and it is being commissioned to further progress toward the European X-ray Free Electron Laser (XFEL) requirements (an rf pulse length about 700 μs at 10 Hz repetition rate and an rf gradient at the cathode of 60 MV/m).

2.1.2 Photocathode

In photocathode rf guns, the cathode emits electrons when illuminated by the drive-laser. The figures of merit for the photocathode characterization are the operative lifetime, the achievable current density, the extracted charge, the quantum efficiency (QE), and the uniformity of the emissive layer [11]. At present, the best photocathode for PITZ is thought to be cesium telluride (Cs_2Te) [14] for the following reasons: Cs_2Te is less sensitive to gas exposure than other alkali semiconductors, it can generate a high current density electron bunch when deposited on a metallic substrate, and it can also provide a reasonable QE of the order of 1%. Cs_2Te has a band gap energy of 3.3 eV and an electron affinity of 0.2 eV. Since Cs_2Te is almost "blind" to visible light, UV light is required for photoemission. Therefore, dark current photoemitted from the cathode by visible light background is negligible.

The photocathodes used at PITZ have been prepared at INFN Milano-LASA [12, 13]. The cathode plug is made from pure molybdenum (Mo) in order to minimize interaction between the emissive materials and the metal substrate [15]. It consists of a cylindrical rod with a diameter of 16 mm. The front surface of the Mo plug is cleaned and polished to optical quality. The edge of the plug is rounded to avoid strong field emission. Thin layers of Tellurium (Te) and Cesium (Cs) are, one after the other, deposited onto the polished plug surface through a mask (with a diameter of 5 mm or 10 mm) in ultrahigh vacuum. During the deposition, the cathode plug is heated to 120°C so that Te and Cs react to produce Cs_2Te. The geometry of the cathode is described in Sec. 5.1.2.

The main reason to change cathodes during the accelerator operation was the growth of dark current to high values at the first phase of the TESLA Test Facility (TTF1) [11] (see Sec. 5.5 for more discussions) or mechanical damage of the Cs_2Te film at PITZ (see Appendix A). Even with the mechanical damages, the cathodes showed a QE of about 0.5% after the final use. The parameters of the photocathodes used at PITZ are summarized in Appendix A.

2.1.3 Drive-laser

In photocathode rf guns, the drive-laser system plays a significant role for the electron beam quality, because the 3D distribution of the electron bunch emitted from the photocathode is determined by the 3D profile of the laser pulse.

Figure 2.2 shows the layout of the laser system of PITZ in 2004, which has been developed by Max-Born-Institute (MBI). The laser material is Neodymium-doped Yttrium-Lithium-Fluoride (Nd:YLF). Its fluorescence bandwidth supports the generation of picosecond pulses with a duration down to 1.5 ps. Even though Nd:YLF has a relatively low thermal conductivity and a low stress fracture limit, it is still able to support the requirement on long trains of laser pulses. Since the Nd:YLF lases at 1047 nm, two nonlinear crystals are used in order to generate the fourth harmonics ($\lambda = 262$ nm) [16]. A flat-top temporal laser pulse profile, required to minimize the transverse emittance of the generated electron beams, is achieved with a pulse shaper.

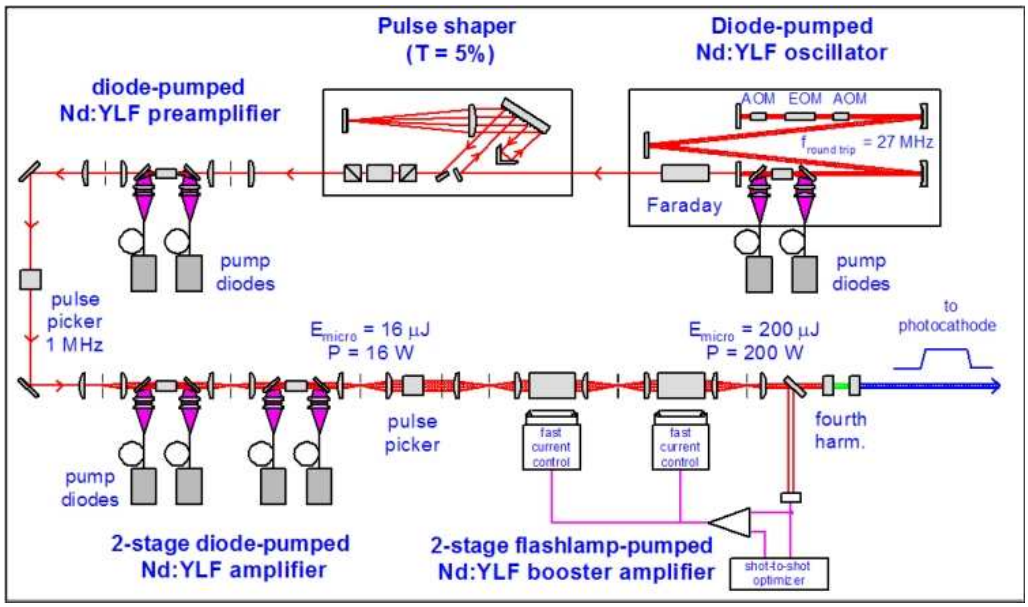

Figure 2.2: Layout of the laser system (from Ref. [17]).

To transport the laser pulse to the photocathode, a telescope system is used. In the telescope system, a beam-shaping aperture is mounted. The aperture selects the central part of the laser pulse so that the aperture can change the laser spot size and produce a truncated Gaussian profile in the transverse direction as well.

2.1.4 Solenoids

Around the rf gun two solenoids are mounted for the compensation of the space charge induced emittance growth [6]. The center of the main solenoid is located 0.276 m downstream from the cathode. The peak field of the main solenoid $B_{z,\,\mathrm{main}}$ has a relation to the solenoid current I_{main} as: $B_{z,\,\mathrm{main}} = 5.86 \times 10^{-4}\ I_{\mathrm{main}}\ [\mathrm{T/A}]$. The power supply of the main solenoid provides a maximum current of 500 A. A typical peak solenoid field for PITZ is about 0.17 T.

Since the tail of the main solenoid field extends to the cathode position, the bucking solenoid has to be used in order to compensate the remaining field at the Cs_2Te cathode. When the remaining field exists at the cathode, the electron beam has an angular momentum which increases the emittance. Since the velocity of the electrons around the cathode is very small, the influence of the weak remaining magnetic field to the beam dynamics is strong.

The peak of the bucking solenoid field is located 0.037 m upstream from the

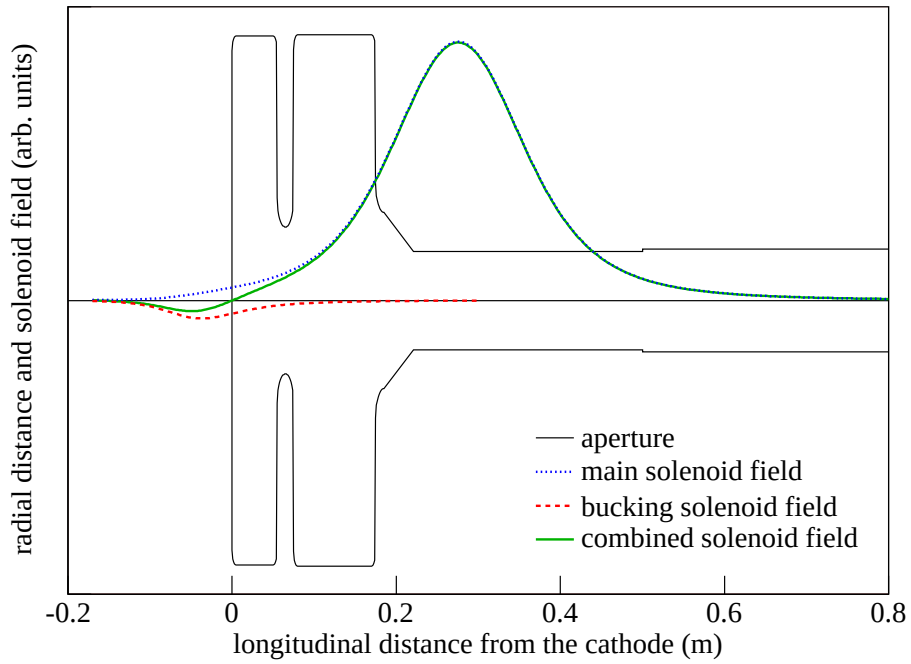

Figure 2.3: Solenoid field distribution at the rf gun [18].

cathode and has the opposite polarity of the main solenoid field. The peak field of the bucking solenoid $B_{z,\,\mathrm{bucking}}$ has a relation to the current I_{bucking} as: $B_{z,\,\mathrm{bucking}} = 5.35\ \times 10^{-4}\ I_{\mathrm{bucking}}\ [\,\mathrm{T/A}\,]$. In order to get vanishing magnetic field at the cathode front surface, the bucking solenoid current has to be chosen as $I_{\mathrm{bucking}} = 0.076\ I_{\mathrm{main}}$. The solenoid fields have been measured with a Hall probe and the field distributions are shown in Fig. 2.3 [18].

2.2 Diagnostics

2.2.1 Drive-laser measurement

Laser energy

The energy of the laser pulses has been measured with a pyroelectric detector (Newport model 818J-09) and a power/energy meter (Newport model 1825-C). The detector is lithium tantalate based and provides a microjoule to millijoule measurement capability in the spectral range from 0.19 to 20 μm [19]. Since some energy is lost in the laser beamline, from the laser room to the vacuum window in front of the accelerator, the energy measurement has been performed just before the vacuum window.

Transverse profile

A charge-coupled device (CCD) camera (JAI model CV-M10 RS) has been installed in an image plane (called virtual cathode) which has the same distance and optics to the laser source as the photocathode in order to monitor the transverse profile of the laser pulse. Using a beam splitter, a small part of the laser pulse is guided to the CCD camera and the other part is guided to the photocathode. Therefore, an *in situ* monitoring of the laser transverse profile is possible.

Longitudinal profile

The temporal profile of the laser pulse is monitored with a streak camera. A small intensity fraction of the laser pulse is transported to the streak camera. The Hamamatsu streak camera module consists of a C5680 streak unit, an M5675 synchroscan sweep unit with a C4742-95 digital camera, and an M5679 dual time base extender unit. The streak unit provides a measurement range from X-rays to near infrared with a temporal resolution of 2 ps [20].

2.2.2 Electron beam measurements

Charge measurement

Two integrating current transformers (ICTs) (Bergoz model ICT-120-070-20:1) have been installed 0.9 m and 6.3 m downstream from the cathode (see Fig. 2.1). Both ICTs are working passively and have a sensitivity of 1.25 V·s/C. The voltage signal

is connected to the data acquisition system and to an oscilloscope in the control room. The ICT allows non-destructive measurements of the bunch charge, but is not sensitive enough for charges below 100 pC. The working condition of the ICT is optimized for 1 nC bunch charge which is a typical charge of PITZ.

A Faraday cup at the diagnostic cross (0.78 m downstream from the cathode) is used to measure low beam charges and dark current. The signal from the Faraday cup is sent to an oscilloscope in the control room. The Faraday cup has an excellent sensitivity down to less than 1 pC. However, measured bunch charge was about 30% lower than the charge determined by the ICT. It might come from scattering of electrons or secondary electron generation at the Faraday cup. Another possibility is that during the transport from the Faraday cup to the oscilloscope, some part of the signal might be reflected somewhere.

Momentum measurement

The momentum of the electron beam is measured by means of a spectrometer dipole 3.45 m downstream from the cathode. A Yttrium-Aluminum-Garnet (YAG) screen is installed 0.7 m downstream from the dipole. The screen is installed in the dispersive arm which is inclined by an angle of 60° to the main beamline. A special control software [21] makes it possible to combine images taken at various dipole currents in order to effectively increase the momentum acceptance of the spectrometer. More detailed information on momentum measurement can be found in Ref. [22] and [23].

Emittance measurement

Among several techniques for transverse emittance measurements, a single slit mask has been used. A small slice of the beam (beamlet) passes through the slit mask located 1.6 m downstream from the cathode. To get information on the divergence of the beam, the size of the beamlet is measured at a YAG screen located 1.01 m further downstream from the slit mask. The slit position has been scanned over the beam in order to get the divergence at different transverse positions of the beam. The emittance measurement procedures can be found in Ref. [24].

Chapter 3

Physics of electron emission

3.1 Field emission

Field emission of electrons is the main source of dark current in photocathode rf guns. Field emission is defined as a liberation of electrons from the surface of materials by high electric fields [25, 26]. The field emission current density increases with the surface electric field strength and depends on the material characteristics as well as the condition of the surface.

Field emission from metals

In metals, the conduction band is filled up to the Fermi level at room temperature, while all the higher energy levels are almost empty. Hence, in case of field emission from metals, electrons near the Fermi level escape from the surface to the vacuum. The electrons have to overcome a surface potential barrier. The form of the potential barrier is, in some distance of the surface, described by the interaction between the electron located at $+x$ outside the metal and an image charge located at $-x$ inside the metal (mirror charge). Thus, the potential barrier has the form $-e^2/(16\pi\epsilon_0 x)$ as shown in Fig. 3.1. Very near to the surface the form of the potential barrier has to change due to the divergence of the mirror charge potential [27]. The detailed form is not known but anyhow irrelevant for our purpose. The external field with strength F in the $-x$-direction is described by a potential $-eFx$ outside the metal. Therefore, the effective potential is written as [28, 29]

$$V(x) = \phi - eFx - \frac{e^2}{16\pi\epsilon_0 x}, \tag{3.1}$$

where ϕ is the work function of the metal and ϵ_0 is the dielectric constant in vacuum. For example, to decrease the height of the potential barrier by 1 eV, an external field of 0.7 GV/m is necessary.

Fowler and Nordheim [25] solved the Schrödinger equation with the Wentzel-Kramer-Brillouin (WKB) approximation in order to calculate the transmission coefficient through the triangular potential barrier. The Fowler-Nordheim equation

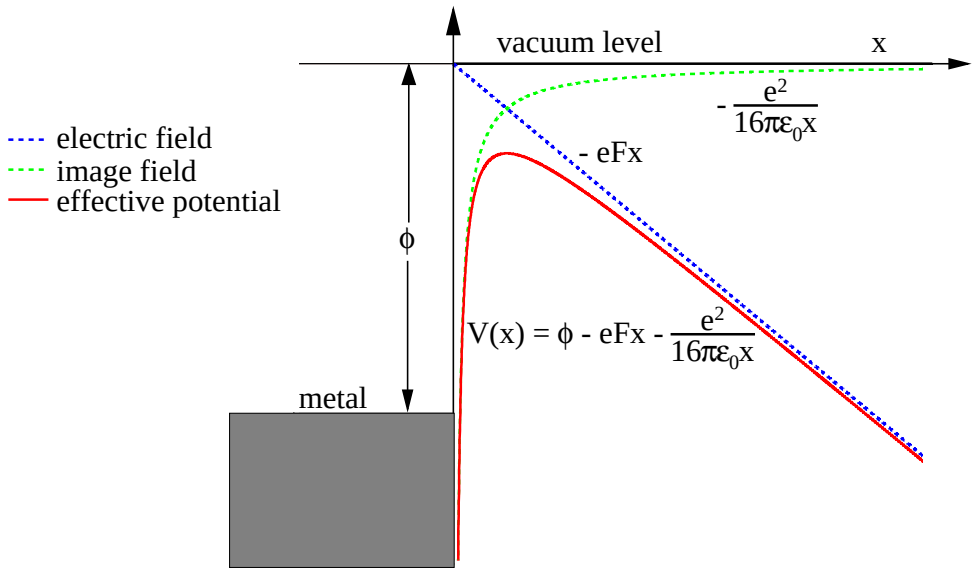

Figure 3.1: Effective potential at field emission of an electron.

gives the magnitude I_{F} of the field emission current in A as [29, 30, 31]

$$I_{\mathrm{FN}} = \frac{e^3}{8\pi h}\frac{A_{\mathrm{e}}\,F^2}{\phi\,t(y)^2}\,\exp\left(-\frac{4}{3}\frac{(2m)^{1/2}}{e\hbar}\frac{\phi^{3/2}\,v(y)}{F}\right)$$
$$= 1.54\times10^{-6}\frac{A_{\mathrm{e}}\,F^2}{\phi\,t(y)^2}\,\exp\left(-6.83\times10^{9}\frac{\phi^{3/2}\,v(y)}{F}\right) \qquad (3.2)$$

where A_{e} is the effective area of field emission in m^2, ϕ is the work function (in eV) of the emitting surface assumed to be uniform over the emitting surface and independent of the external field, F is the field strength in V/m, e is the electron charge in C, m is the electron mass in kg, and h is Planck's constant. $t(y)$ and $v(y)$ are tabulated functions, where y is the Nordheim parameter [32] (see Appendix B). Here, an empirical field enhancement factor β_{field} has to be introduced in order to account for the observation that field emission takes place already at a field strength of the order of 10 MV/m instead of 1 GV/m. The field enhancement factor β_{field} is related to the topology of the local emission site. With the field enhancement factor, the field strength F is re-written as $F = \beta_{\mathrm{field}}\,E$, where E is the surface electric field in V/m. With the approximation $v_a(y)$ of $v(y)$ obtained in Appendix B, the Fowler-Nordheim equation (Eq. 3.2) can be simplified as

$$I_{\mathrm{FN}} = \frac{1.54\times10^{-6}\exp(9.35\,\phi^{-1/2})\,A_{\mathrm{e}}\,(\beta_{\mathrm{field}}E)^2}{\phi\,t(y)^2}\,\exp\left(-\frac{6.32\times10^{9}\,\phi^{3/2}}{\beta_{\mathrm{field}}E}\right). \qquad (3.3)$$

Assuming $t(y) \simeq 1$, the simplified equation (Eq. 3.3) does not include the Nordheim parameter y.

The dependence of the field emission current on the rf phase is determined by the field emission current (Eq. 3.3) corresponding to the field strength at the rf phase and the tunneling time for the field emission. The emission current I_{FN} corresponding to the field strength at the rf phase ϕ_{rf} is written as

$$I_{\mathrm{FN}} \sim (E_0 \sin\phi_{\mathrm{rf}})^2 \exp\left(-\frac{1}{E_0 \sin\phi_{\mathrm{rf}}}\right) \tag{3.4}$$

where E_0 is the amplitude of the sinusoidal macroscopic surface field in V/m. The tunneling time for the field emission depends on the height and thickness of the triangular potential barrier and has the following relation [33]:

$$T = \frac{\sqrt{2mI}}{e\beta_{\mathrm{field}}E}, \tag{3.5}$$

where I is the height of the contact Fermi potential written as

$$\begin{aligned} I &= \phi - \sqrt{\frac{e^3 F}{16\pi\epsilon_0}} \\ &= \phi - 1.897 \times 10^{-5} F^{1/2}\,[\mathrm{eV}]\,. \end{aligned} \tag{3.6}$$

At the typical operating condition of PITZ ($F = \beta_{\mathrm{field}}E \sim 4$ GV/m) the tunneling time is estimated to be about 2 fs, which is negligible compared to the rf cycle (769 ps). Therefore, the phase dependence of the field emission current can be drawn like Fig. 3.2.

Figure 3.2 shows that the field emission is concentrated on the maximum electric field region of an rf cycle. Therefore, the field emitted electrons produced on the cathode are preferably accelerated in the forward direction by the rf electric field.

The average field emission current during one rf cycle is described as [34, 35]

$$\begin{aligned} \bar{I}_{\mathrm{FN}} &= \frac{1}{T}\int_0^T I_{\mathrm{FN}}\,dt \\ &= \frac{5.79 \times 10^{-12} \times \exp(9.35\,\phi^{-1/2})\,A_{\mathrm{e}}\,(\beta_{\mathrm{field}}E_0)^{5/2}}{\phi^{1.75}} \exp\left(-\frac{6.32 \times 10^9 \phi^{3/2}}{\beta_{\mathrm{field}}E_0}\right), \end{aligned} \tag{3.7}$$

where T is the period of an rf cycle. In this step, $t(y)$ has been set to 1 since it is close to 1 and contributes just linearly to $\bar{I}_{\mathrm{FN}}$.

Fowler-Nordheim plots are useful to extract the field enhancement factor and the effective area of the field emitter. The plots can be made with an equation derived from Eq. 3.7:

$$\frac{d\log_{10}\left(\bar{I}_{\mathrm{FN}}/{E_0}^{5/2}\right)}{d\,(1/E_0)} = -\frac{2.71 \times 10^9\ \phi^{3/2}}{\beta_{\mathrm{field}}}. \tag{3.8}$$

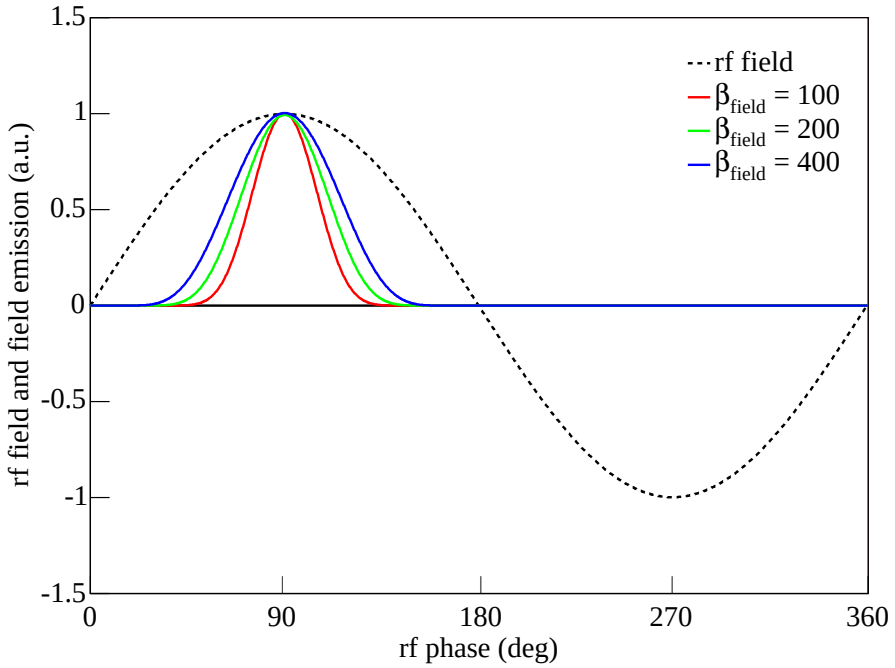

Figure 3.2: Normalized intensity distribution of field emission in comparison with the rf field for one rf cycle. The field emission curves have been computed using the simplified Fowler-Nordheim equation (Eq. 3.3) with ϕ of molybdenum (4.6 eV) assuming various β_{field} values of 100, 200, and 400.

As explained in Eq. 3.3 and 3.7, the field emission current density depends not only on the surface electric field but also on the work function of the material. Main materials in the gun cavity are Cu for the cavity, Mo for the cathode plug, and Cs and Te for the photoemissive film (Chap. 2). The work functions of the main materials for a polycrystalline state in the gun cavity are shown in Table 3.1 [36].

Table 3.1: Work functions for the main elements in the gun cavity.

element	ϕ (eV)
Cu	4.65
Mo	4.6
Te	4.95
Cs	2.14

When the electric field is so high that the top of the potential barrier is not higher than the Fermi level of the solid material, electron emission does not occur solely by tunneling but by direct emission over the barrier. It is called the field-

induced ballistic electron emission [29] and $y \geq 1$ applies in this condition. The field strength F_{b} when ballistic emission occurs is approximately written as [29]

$$F_{\mathrm{b}}/(\mathrm{V\ nm^{-1}}) \geq 0.6945 \times (\phi/\mathrm{eV})^2. \tag{3.9}$$

For Mo, $F_{\mathrm{b}} = 14.7 \times 10^9$ V/m. Assuming $\beta_{\mathrm{field}} = 100$, the ballistic emission takes place at $E = 147$ MV/m. For Cs, $F_{\mathrm{b}} = 3.18 \times 10^9$ V/m. Assuming $\beta_{\mathrm{field}} = 100$, the ballistic emission takes place at $E = 32$ MV/m. In a range of the rf field strength in L-band rf gun cavities (up to 60 MV/m), the ballistic emission from metal materials in the gun cavity will not take place. If elementary Cs stays without chemical combination with Te, for instance at the boarder of a photoemissive Cs_2Te film, it may be a source of the ballistic emission.

Field emission from semiconductor photocathodes

In semiconductors at room temperature, the Fermi level is located in the forbidden band between valence and conduction bands and the conduction band is rarely occupied. Therefore, electrons can be emitted only from the valence band. When $kT \ll E_{\mathrm{G}}$, where T is the temperature and E_{G} is the band-gap energy of the semiconductor, the conduction band is empty. In that condition, field emission occurs by tunneling from the valence band to the vacuum if the applied field is high enough. Since each emitted electron leaves a positive hole in the surface of the material, the emission current will be balanced by the conduction provided by the holes [28].

Figure 3.3 shows a simplified energy band diagram of Cs_2Te [37]. In Cs_2Te, peak densities of the states locate at 0.7 eV and 1.4 eV below the maximum of the valence band [38]. When the external rf field is applied to the material surface, the vacuum level, i.e. the potential barrier, is deformed to be triangular like for metals. Through the triangular barrier, electrons in the valence band can leave to vacuum. For the emission, electrons will be supplied from the state at 0.7 eV below the maximum of the valence band because the state is of uppermost maximum density. Considering the energy band gap ($E_{\mathrm{G}} = 3.3$ eV) and the electron affinity ($E_{\mathrm{A}} = 0.2$ eV), the electrons in the state at 0.7 eV below the valence band maximum will feel a potential barrier of 4.2 eV.

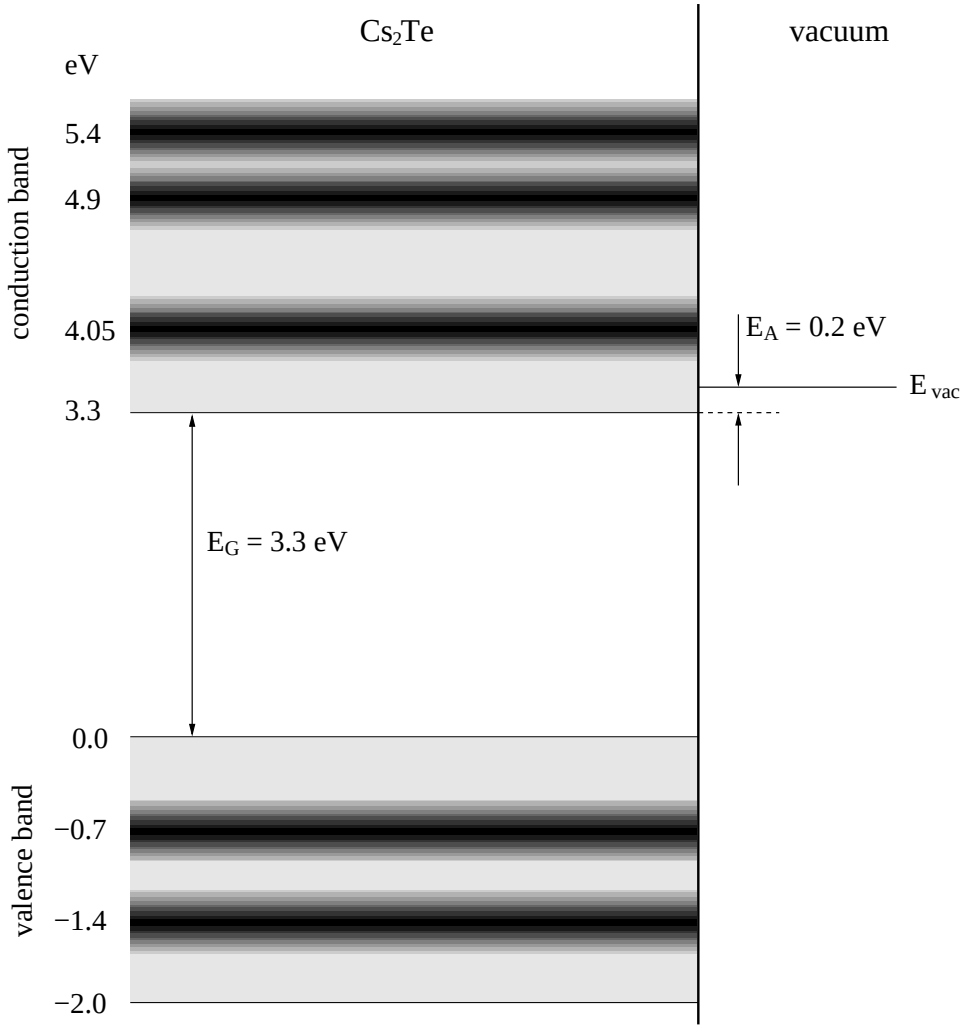

Figure 3.3: A simplified energy band diagram of Cs_2Te [37]. The maxima of the density of states are painted in dark. This band diagram has been constructed according to the measurements by Powel *et al.* [38].

3.2 Photoemission

The process of photoemission can be concisely described in a three-step model [39]
(1) the absorbed photons deliver their energy to electrons inside the material
(2) the energized electrons move through the material to the surface, losing some energy
(3) the electrons escape over the surface barrier (electron affinity) into the vacuum.

Not all photons incident on a photoemissive material cause electron emission. When photons strike a photoemissive material, some part is reflected from the surface and only a fraction can impart the energy to the electrons in the material. A simplified photoemission process is illustrated in Fig. 3.4. The ratio of the number of emitted electrons to the number of incident photons is defined as the quantum efficiency (QE). The QE is always less than unity because the photon absorption is less than one, some fraction of energy is lost at each stage of the photoemission process, and the generated electrons can move into the material[1]. Dominant factors determining the QE are the wavelength of the incident light and the composition, thickness, and topology of the photoemissive material.

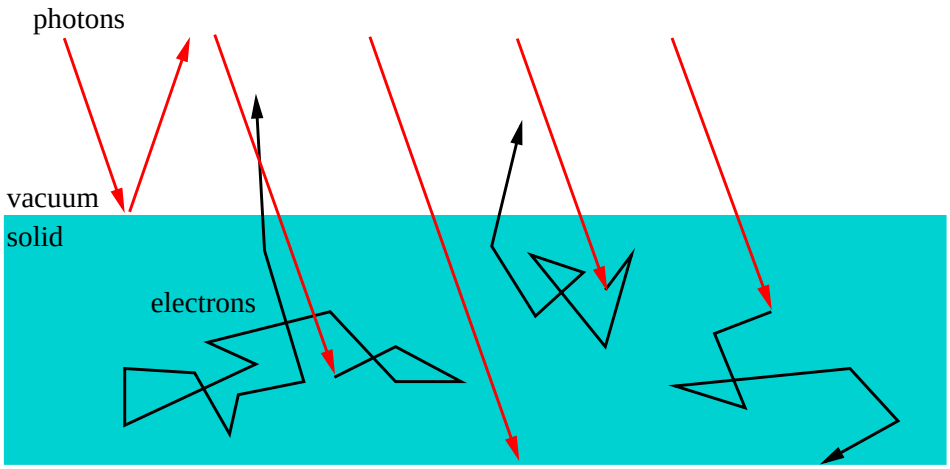

Figure 3.4: photo electron generation processes.

Metals are highly reflective. Semiconductors or insulators have a low reflection coefficient and absorb the photon energy more effectively. The absorption coefficient depends on the energy of the photons and on the band structure of the material. In metals, it is possible for electrons in the conduction band to be excited by photons and to be emitted into the vacuum if the photon energy is greater than the work function ϕ. In semiconductors, the absorption of the incident photons is very high

[1] This is true except if secondary electrons are generated during the photoemission process inside the material at very high photon energies [40].

for $E_{\mathrm{photon}} > E_{\mathrm{G}}$, where E_{G} is the width of the band gap. The major part of the incident photons is absorbed within a few tens of nanometers [41]. For photon energies less than E_{G}, the absorption decreases rapidly.

The probability that an excited electron will be emitted depends on the energy loss process governing its passage to the surface. This process is different for metals and semiconductors. In metals, the conduction band is partially occupied by free electrons. An electron excited in the conduction band will lose its energy mainly through collisions with free electrons and hardly propagate to the surface. Therefore, the escape depth is only a few nm. In semiconductors, the conduction band is almost empty and the probability of collisions with other free electrons is very rare. Therefore, the excited electrons can travel relatively long distances through the material provided their energies are lower than $2E_{\mathrm{G}}$. If the electron energy is higher than $2E_{\mathrm{G}}$, it may lose energy by the creation of electron-hole pairs.

As discussed above, excited electrons in a metal lose energy by the collisions with other free electrons. When the electron barely arrives the surface, its energy must be greater than the work function of the material. On the other hands, in

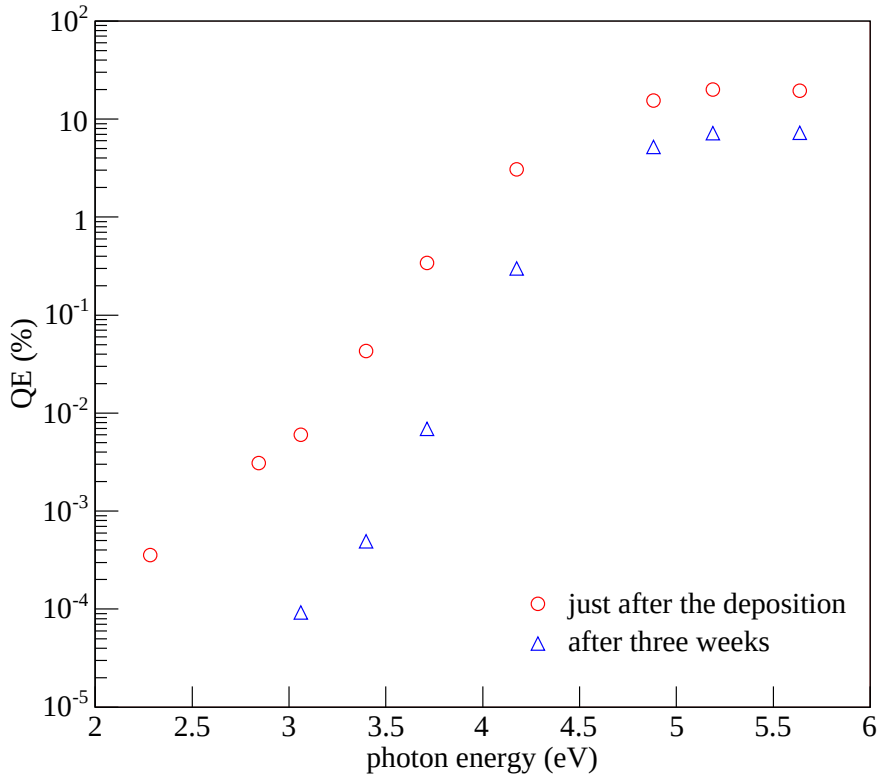

Figure 3.5: QE measurements vs. photon energy. The measurements have been performed with an UV lamp using different wavelengths of band pass filters. (Courtesy of P. Michelato, L. Monaco, and D. Sertore)

semiconductors, an electron which has an energy lower than $2E_G$ can quite freely propagate to the surface barrier. When the electron energy is higher than $E_G + E_A$, where E_A is the electron affinity of the material, the electron can overcome the potential barrier. This energy region between $E_G + E_A$ and $2E_G$ is called the magic window [39]. Especially for semiconductors which have a large band gap E_G and a small, or even negative electron affinity E_A, the escape length can reach several μm [42].

The QE of the Cs_2Te cathode as a function of the photon energy has been measured by Michelato *et al.* at INFN Milano-LASA (see Fig. 3.5). At the measurement

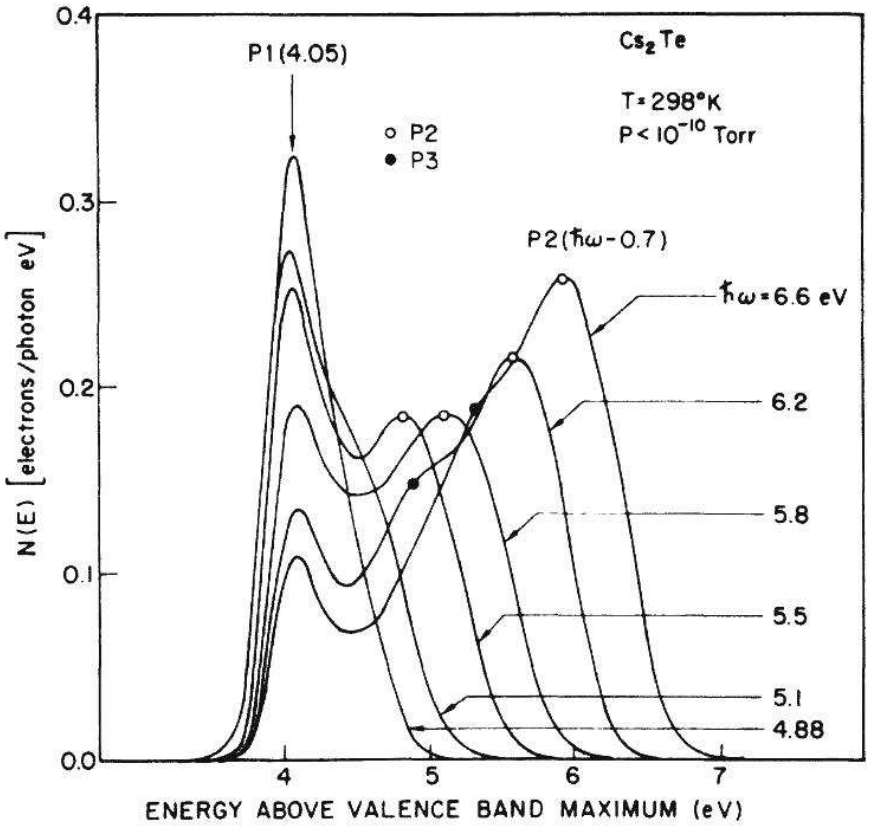

Figure 3.6: Energy distributions of the photoemitted electrons (from Ref. [38]). As photon energy increases, the peak P1 appears in the energy distribution curves at the same energy 4.05 eV. The peak comes from a maximum density of state in the conduction band located 4.05 eV above the valence band maximum. The peak P2 appears for a photon energy higher than 5.1 eV and comes from a maximum density of state in the valence band located 0.7 eV below the valence band maximum. The peak P3 appears for a photon energy higher than 6 eV and comes from a maximum density of state in the valence band located 1.4 eV below the valence band maximum [38].

when the cathode was just deposited, a steep decrease of the QE with the photon energy happens of about 3.5 eV photon which corresponds to the threshold energy for photoemission defined by E_{G} (3.3 eV) + E_{A} (0.2 eV). At the measurement three weeks after the deposition, the steep decrease of the QE moved to about 4.0 eV, which means the threshold energy has increased. Meanwhile, the cathode was transferred from the preparation chamber to an analysis chamber for a time-of-flight measurement to determine the energy of the emitted electrons [43].

In the Cs_2Te cathode, electrons excited by the UV laser ($\lambda = 262$ nm or $\nu h = 4.75$ eV) are most probably located 0.75 eV above the conduction band minimum, or 4.05 eV above the valence band maximum (see Fig. 3.6) because electrons cannot jump to the second structure of a maximum density of state at 4.9 eV above the valence band maximum. Therefore, the kinetic energy of the electrons photo-excited is 0.75 eV in Cs_2Te. When the electrons are emitted into the vacuum, the free electrons have an energy of certain level (vacuum level). The energy difference between the vacuum level and the conduction band minimum is called electron affinity.

Figure 3.7 shows the kinetic energy spectrum of electrons photoemitted from a Cs_2Te cathode obtained with a time-of-flight measurement by P. Michelato *et al.* at the INFN Milano-LASA [44]. For photoemission, UV light with $\lambda = 264$ nm has been used. In Fig. 3.7, a peak of the spectrum is located at 0.42 eV, which means the electron affinity of the Cs_2Te cathode is 0.33 eV.

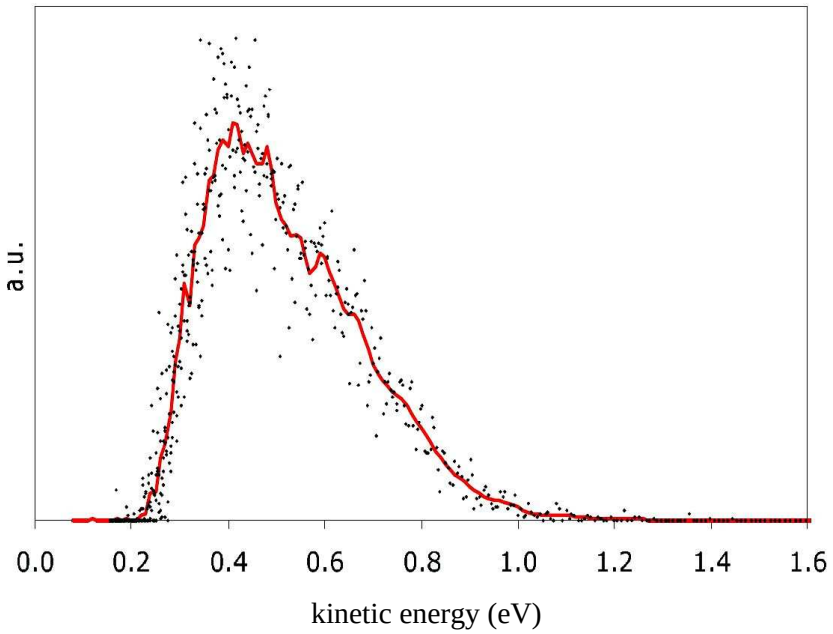

Figure 3.7: Kinetic energy spectrum of electrons photoemitted from a Cs_2Te cathode obtained with a time-of-flight measurement (from Ref. [44]). A photon wavelength of 264 nm has been used.

When the emissive material is thick, the electrons are in thermal random motion and lose their energy little by little by electron-phonon scattering. When the electrons reach the material-vacuum interface, only the electrons with a kinetic energy, actually the longitudinal component of momentum, higher than the surface vacuum level can be emitted into the vacuum. From the above point of view, the response time τ_{ph} of photoemission can be estimated with the following relation [42] when no external electric field applied:

$$\tau_{\mathrm{ph}} = \frac{E_k}{\Delta E_p}\frac{l_p}{v_a}, \tag{3.10}$$

where E_k is the kinetic energy of electrons above the surface vacuum level, ΔE_p is the average energy loss per electron-phonon collision, l_p is the electron-phonon scattering length, and v_a is the average speed of the electron over its complete trajectory. According to the work by Ferrini *et al.* [45], l_p is 3 nm and the corresponding ΔE_p is 5 meV. With the average thermal velocity[2] $v_a = 3.6 \times 10^5$ m/s, $\tau_{\mathrm{ph}} \approx 0.9$ ps is estimated. In reality, this calculation overestimates the delay time because Eq. 3.10 accounts for total emission time. In Ref. [45], τ_{ph} has been estimated to be about 0.1 ps by means of a Monte Carlo simulation as used at PITZ, or a 20 nm Cs_2Te film on a Mo substrate.

Under the influence of an external electric field, the drift velocity of the electrons plays a dominant role in the response time (see Fig. 3.8). At a field strength below about 1 MV/m, the drift velocity increases linearly with the field strength. But at an electric field higher than about 1 MV/m, the drift velocity v_{dr} is saturated at around 10^5 m/s [46, 47]. This means that the emission time by the drift, τ_{dr}, can be estimated as

$$\tau_{\mathrm{dr}} = l_{\mathrm{Cs_2Te}}/v_{\mathrm{dr}}, \tag{3.11}$$

where $l_{\mathrm{Cs_2Te}}$ is the penetration depth of the UV photons into the Cs_2Te film. If we assume $l_{\mathrm{Cs_2Te}} = 30$ nm, τ_{dr} is of the oder of 0.1 ps.

[2] Assuming the mass of the excited electron in the material is equal to the rest mass of an electron, the average thermal velocity is obtained with the relation, 0.75 eV $= (\gamma - 1)m_0c^2$.

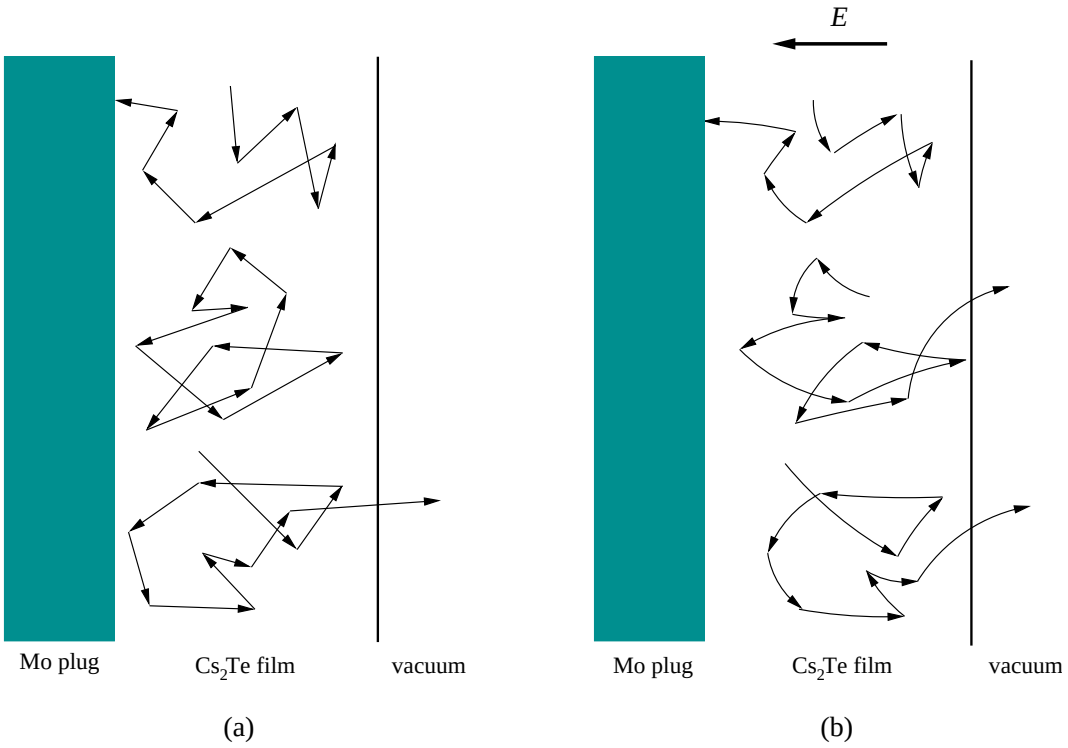

Figure 3.8: Trajectories of excited electrons in a Cs_2Te film. (a) When no external electric field is applied, the electrons are in thermal random motion between collisions. (b) When an external electric field E is applied, the electrons drift to the opposite direction of the field.

3.3 Secondary emission

When a primary electron strikes a solid material, it may penetrate the surface and generate secondary electrons. The origin of secondary electrons is separated into the following three categories [48]: When the primary electron is reflected off the surface, it is called "back-scattered electron". If the electron penetrates the surface and scatters off one or more atoms and is reflected back out, it is a "rediffused electron". If the electron interacts inelastically with the material and releases more electrons, "true secondary electrons" are generated. These secondary generation processes are sketched in Fig. 3.9.

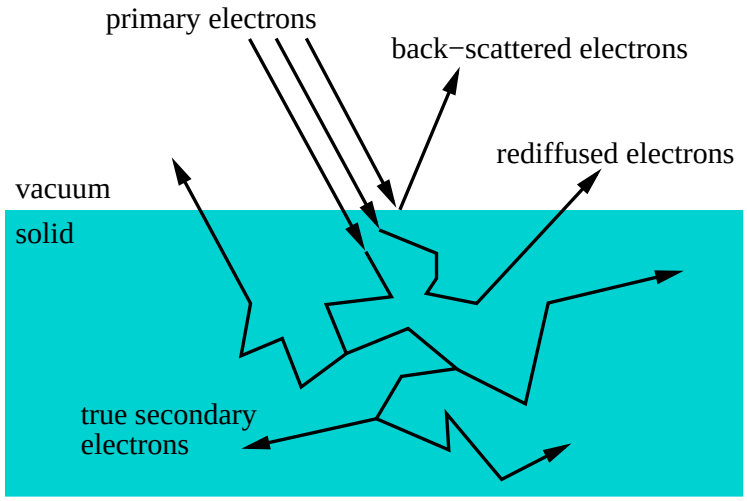

Figure 3.9: Secondary electron generation processes.

When the primary electrons have an energy of more than several keV, the true secondary electrons are dominant because back-scattering and rediffusing of electrons hardly occur at such high impact energy [48]. In the rf gun cavity, the primary electrons typically have a high energy over several hundreds keV because of an rf field of the order of 10 MV/m. Therefore only true secondary electrons are considered here.

The main features of true secondary emission are qualitatively understood by means of the three-step model similar as for photoemission [49]:
(1) production of internal electrons by bombardment of the primary electrons,
(2) transport of the internal secondary electrons toward the surface, which is accompanied by some energy loss due to inelastic scattering, and
(3) escape of the electrons through the solid-vacuum interface.

The secondary electron emission process shows great similarities to the photoemission process which is discussed in an equivalent three step model. Differences arise due to the primary process (penetration depth of ($\sim$eV) photons compared to the penetration depth of ($\sim$keV) electrons) and differences of the secondary electron

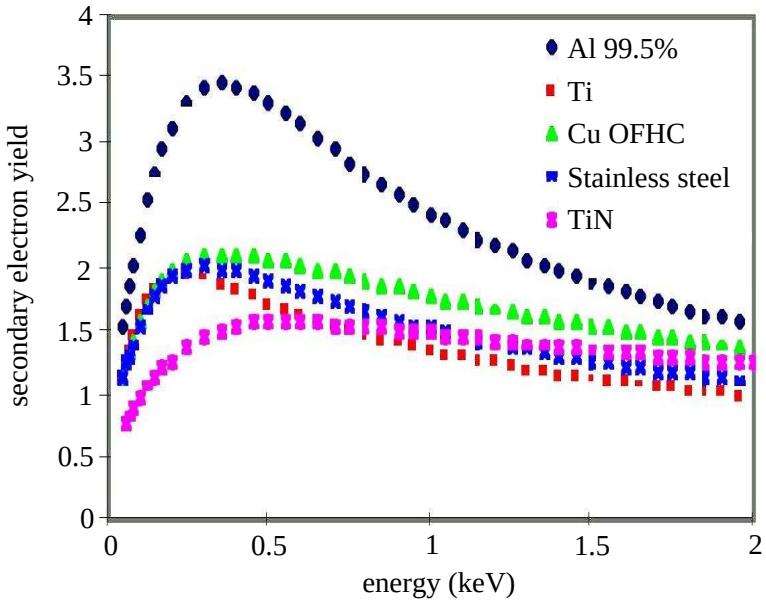

Figure 3.10: An example of measured secondary electron emission yield curves (from Ref. [51])

and photoelectron energies, respectively. When a UV photon energy of 4.75 eV is applied to Cs_2Te, photoelectrons are produced into the so-called magic window, i.e., their energy is too low to produce electron-hole pairs by electron-electron scattering and hence they don't loose energy during the transport to the surface. Secondary electrons, on the other hand, start with higher energy but loose effectively their energy on the way to the surface until they reach the magic window. Despite these differences, good photo-emitters are in general good secondary emitters [50] and the surface properties which affect the photoemission can also affect the secondary emission.

The secondary electron emission yield δ is defined as the ratio of the number of emitted electrons to the number of incident electrons to the solid. One approach to the characterization of the secondary emission properties of solids is the plot of δ as a function of E_p, the kinetic energy of the incident (or primary) electrons.

Figure 3.10 shows an example of measured secondary emission yield as a function of the impact energy of primary electrons. For the metals, the secondary yields increase up to $1.5 \sim 3.5$ and then decrease with the impact energy. At impact energies of several hundreds eV, the secondary yields reach the maximum.

For numerical calculation of secondary emission a simplified model for $\delta(E_p)$, the secondary emission yield depending on the energy of the primary electron from the surface [48], can be presented as:

$$\delta(E_p) = \delta_{\max} \cdot \frac{E_p}{E_{p,\max}} \cdot \frac{s}{s - 1 + (E_p/E_{p,\max})^s}, \tag{3.12}$$

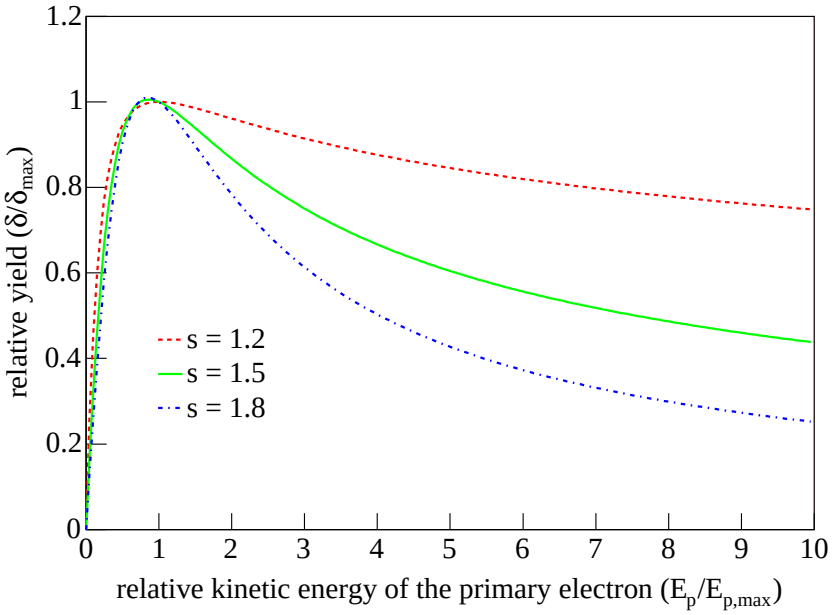

Figure 3.11: Secondary electron emission yield curves according to Eq. 3.12.

where $\delta_{\max}$ is the maximum secondary yield, which occurs at the primary electron energy $E_{p,\max}$ and s is a fit parameter, larger than one, which describes the form of the secondary emission yield curve. Fig. 3.11 shows the relative secondary yield for various s.

At impact energies lower than $E_{p,\max}$, the electron penetration depth increases with E_p and the generated secondary electrons are within the range of the escape depth. As the impact energy increases beyond $E_{p,\max}$, the penetration depth exceeds the escape depth so that the generated secondary electrons cannot reach the surface and the secondary yield decreases with E_p.

$\delta_{\max}$, $E_{p,\max}$, and s are widely varying parameters depending on the kind of solid material and on the state of the solid surface. Values of $\delta_{\max}$ range from 0.5 to 1.8 for metals and from 1 to 24 for semiconductor or insulators. Corresponding values of $E_{p,\max}$ range from 100 to 1000 eV for metals and from 250 to 1800 eV for semiconductor or insulators [52].

For p-type semiconductors like Cs_2Te, the average number of internal electrons produced by the primary electrons (Step 1) is proportional to the impact energy of the primary electrons divided by the energy required to make an electron-hole pair [53]. The probability of the transport toward the surface (Step 2) is related to the penetration depth of the primary electron and the mean free path of the secondary electrons, while the probability that an electron which reaches the surface escapes from the solid (Step 3) is a function of the energy of the electron divided by the electron affinity of the emissive material [53].

For metals, the escape depth is less than 10 nm due to the strong electron-

electron interaction in the conduction band. Due to the short escape depth, the generated secondary electrons disappear while approaching the surface and a very low ($\delta_{\max} \sim 1$) secondary emission yield is typical.

For this thesis, ASTRA [7] has been upgraded in order to generate and track secondary electrons. When an electron hits a geometrical aperture in ASTRA, the program generates a random integer number of secondaries according to this model function using a Poisson generator. The energy of the secondaries is assumed to have a Gaussian distribution with a few eV width [54, 55]. However, the initial energy as well as the emission angle of the secondaries does not affect the beam dynamics in the gun cavity because the energy is relatively small compared to the energy gain by the accelerating field at the cathode.

In the model, the time delay of the secondary emission is assumed to be negligibly small in comparison with the rf cycle of the cavity [56]. The incidence angle effect of the secondary emission yield is not considered because electron bombardment at the cavity is almost normal direction to the surface especially for the backplane of the cavity.

To the author's knowledge, no measured data for the secondary electron emission properties of Cs_2Te are published yet. But the parameters can be estimated from the data of similar materials such as CsI. CsI has a maximum secondary yield of 17.23 at a primary electron energy of 2.15 keV [57, 58]. This high secondary yield is explained by the high electronic band gap of 6.3 eV and low electron affinity of 0.1 eV [57].

Cs_2Te has a band gap of 3.3 eV and an electron affinity of 0.2 eV [38, 59]. Therefore, Cs_2Te is expected to have similar secondary emission properties as CsI. Actually, the secondary emission yield is strongly dependent on the surface state of the emissive material, i.e., chemical contamination and topology of the emitted surface. The dependence of the secondary emission yield on cathode parameters is discussed in Sec. 4.1.3.

Chapter 4

Effective emission mechanisms

High gain FELs demand high quality electron beams with an emittance below 1 mm mrad at 1 nC as discussed in Sec. 7.1. This emittance is close to the lower limit given by the thermal emittance which is defined by the kinetic energy distribution of the electrons emitted from the photocathode. In order to decrease the limit, a detailed understanding of the processes at the cathode is essential. The parameters characterizing photoemission are the quantum efficiency (QE), the kinetic energy of the photoelectrons, and the response time between the impact of the drive-laser photon and the extraction of the photoelectrons. Secondary emission can be parameterized in terms of secondary yield and response time between primary and secondary electrons.

In photocathode rf guns, the emission mechanisms at the photocathode play a crucial role in the overall beam dynamics. The electron distribution in the six dimensional phase space, consisting of the two transverse coordinates and momenta as well as the longitudinal coordinates and momentum, is determined by the three dimensional spatial profile of the drive laser and the electron emission properties. The emission properties are governed by the image charge effect of the emitted electrons to the material, the space charge force of the electrons in a bunch, and the Schottky effect, i.e. emission current increase with the electric field strength.

Even though the emission parameters of Cs_2Te photocathode are partly known [60], these parameters are not constant during gun operation but modified by the rf field strength as well as contaminations of the surface. Therefore, the effective emission mechanisms under gun operation conditions are studied in this chapter.

4.1 Low charge beam dynamics

Electron beams with a low bunch charge allow to study the emission mechanisms with a small influence of the space charge force and the sensitivity of the beam dynamics to the emission phase can be increased with a short drive-laser pulse length. With this condition, photoemission and secondary emission mechanisms are studied by means of the beam dynamics depending on the emission phase, i.e.

the rf phase when the electron leaves the cathode. Assuming that the electron is emitted by the drive-laser without delay time, the emission phase can be defined, for simplicity, as the relative phase of the gun rf field to the laser pulse.

In this section, the dynamics of a single electron, depending on the emission phase, is numerically simulated and compared with experimental results. Using the beam dynamics in the gun cavity, the photoemission and the secondary emission mechanisms are discussed.

For Sec. 4.1.2 and 4.1.3, experiments have been performed with the following conditions: A short drive-laser pulse with a Gaussian distribution (2.3 ps rms) was used in order to observe clearly the rf phase dependence of the electron beam dynamics; a very low charge (∼5 pC) electron bunch was generated with the laser pulse to get rid of the space charge effects; and a relatively low rf field (21.6 MV/m of maximum field at the cathode) was applied in order to reduce the impact energy of the photoemitted primary electrons, i.e. the UV-laser induced photoelectrons, and to generate a relatively large number of secondary electrons. The main and bucking solenoids were switched off during charge measurement to simplify the electron beam dynamics and a cathode with a thick Cs_2Te film (cathode #500.1, 60 nm thickness) was inserted to maximize the secondary electron production. These parameters are summarized and compared to the normal operating conditions of the first stage of PITZ in Table 4.1.

Table 4.1: Machine parameters.

	Low charge study	Normal operation of PITZ
Longitudinal laser profile	2.3 ps rms Gaussian	∼20 ps flat-top
Bunch charge	∼5 pC	1 nC
Maximum rf field	21.6 MV/m	≥40 MV/m
Main solenoid field at peak	0 T	∼0.17 T
Cs_2Te thickness	60 nm	30 nm

4.1.1 Single electron dynamics

The longitudinal electric field distribution on the z–axis inside the rf gun cavity is shown in Fig. 4.1 with the geometrical aperture of the gun cavity. The gun cavity and the rf coupler are cylindrically symmetric with respect to the z axis. At the cathode, the longitudinal rf field oscillates as $E(\phi) = E_0 \sin\phi$, where E_0 is the maximum field and ϕ is the rf phase. When ϕ has a value between 0° and 180°, the electrons are able to be extracted out of the cathode by the rf field.

Figure 4.2 shows the momentum of a photoemitted electron in the 1.5 cell rf cavity with the maximum rf field $E_{\max} = 21.6$ MV/m at the cathode as a function of the emission phase. The corresponding accelerating gradient at the cathode is shown together with the simulation. Since the electrons start with a velocity close

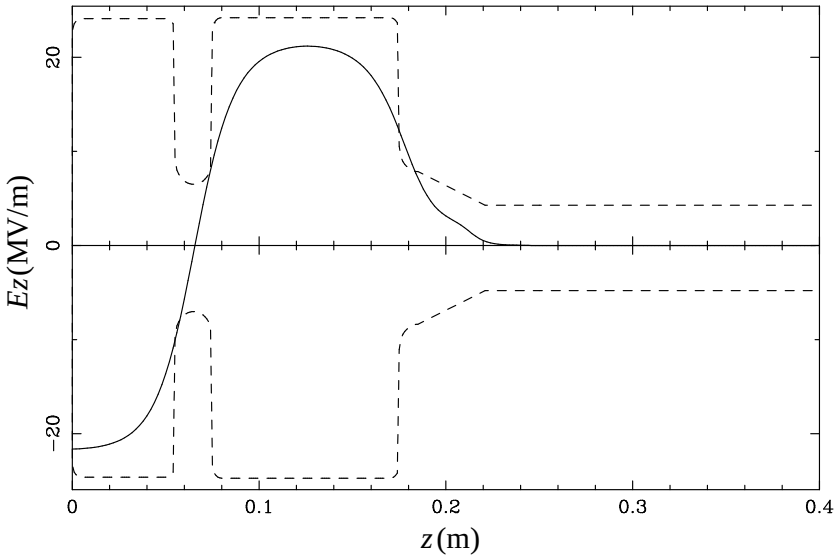

Figure 4.1: Longitudinal electric field (full line) and cavity aperture (dashed line, transversally in arbitrary units) used in the simulations.

to zero at the cathode, a strong phase slippage occurs, which is responsible for the functional dependence shown in Fig. 4.2.

Figure 4.3 shows the rf phase, $\omega t - kz + \phi_0$ [5], at three locations, i.e., the entrance, the center, and the exit of the full cell as a function of the emission phase ϕ_0, where ω and k are the rf frequency and the wave number, z is the observation position, and t is the arrival time of the electron at the position. Electrons starting at 0° reach already a phase of 65° at the center of the full cell. They are hence efficiently accelerated in the half and the full cell. Acceleration at a phase of 90° at the center of the full cell occurs at a starting phase of 48°, but when electrons reach near the exit of the gun cavity they experience a deceleration due to the phase slippage (see Fig. 4.3). Therefore, this phase cannot be optimum for electrons to gain highest momentum. Particles starting at ∼95° slip further to a phase of inefficient acceleration in the half cell and end up at 180° in the full cell. At a phase larger than ∼95° particles are decelerated in the full cell and are eventually stopped. Electrons starting between ∼95° and ∼113° can move forward and backward in the gun, while the phase may slip over several rf cycles. These electrons may hit the cathode, or an aperture, or flow out of the cavity at specific phases.

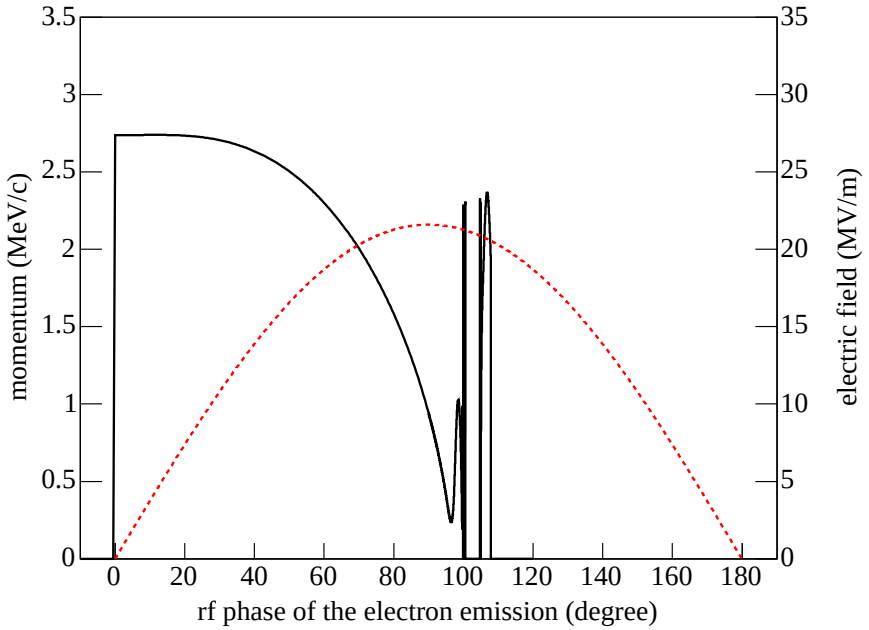

Figure 4.2: Longitudinal electric field on the cathode (red, dotted line) and momentum gain for a single electron (black, full line) vs. rf phase. The simulation has been tracked up to the 1st Faraday cup position, 0.78 m.

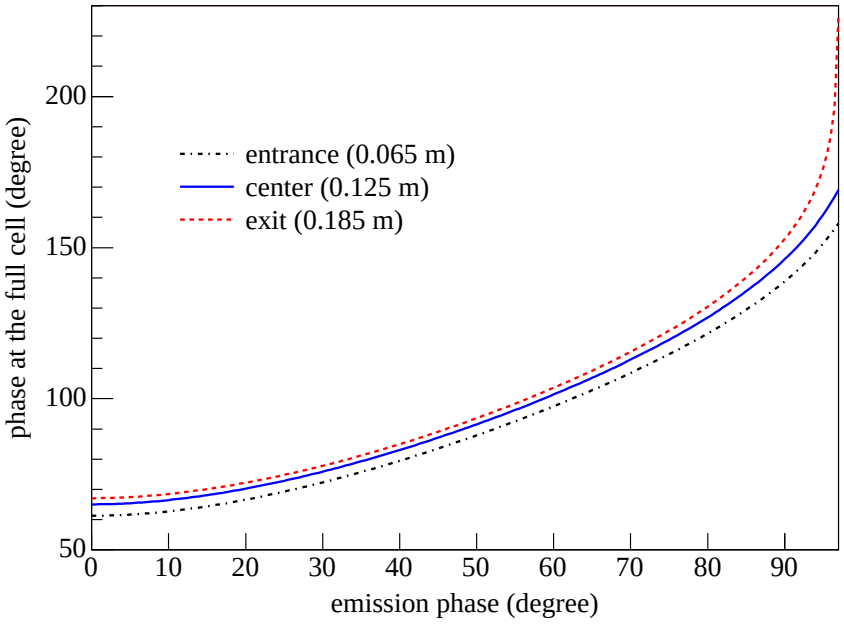

Figure 4.3: Phase, $\omega t - kz + \phi_0$, at the entrance, center, and exit of the full cell vs. emission phase in the gun cavity.

If the electron travels backward and hits the Cs_2Te photocathode it can generate secondary electrons. If the electron, however, hits the copper cavity or the molybdenum cathode plug it mostly disappears because Cu and Mo have secondary emission yields below one except for a primary impact energy between several hundreds eV and a few keV. Secondary emission from the cavity surface except the Cs_2Te photocathode is ignored in this study because such a low impact energy hardly occurs in a cavity with high rf field.

The simulation result of the secondary emission yield in dependence on the emission phase of the primary electron is shown in Fig. 4.4. For this simulation 10 000 primary electrons are tracked to generate secondary electrons, so that statistical fluctuations due to the random generation of integer numbers (as discussed in Sec. 3.3) of the secondaries are minimized. While the number of generated secondary electrons decreases in the phase range of 108° to 113°, the momentum of the secondaries increases as shown in Fig. 4.5.

The two parameters responsible for this dependence are the rf phase at which the primary electron hits the cathode (impact phase) and the primary electron energy. In this study, the launch phase of the secondary electron is assumed to be same as the impact phase of the primary electron, i.e. the secondary electron starts without delay. Figure 4.6 shows both impact phase and energy parameters for the emission phase range of 108° to 113° of the primary electron. Around 108°, the impact phase of the photo-emitted electrons is ∼60° so that the generated secondary electrons

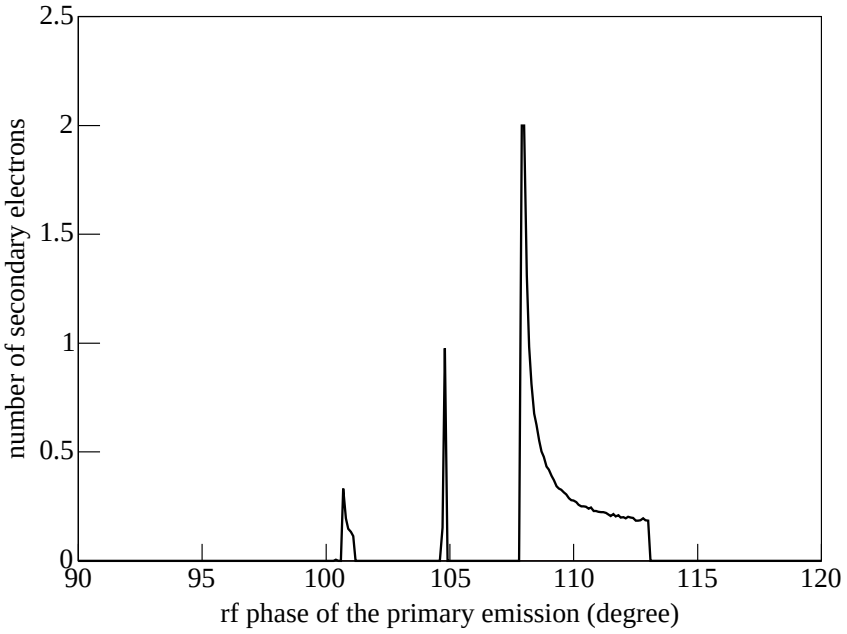

Figure 4.4: Average number of secondary electrons generated by a single primary electron as a function of the primary emission phase.

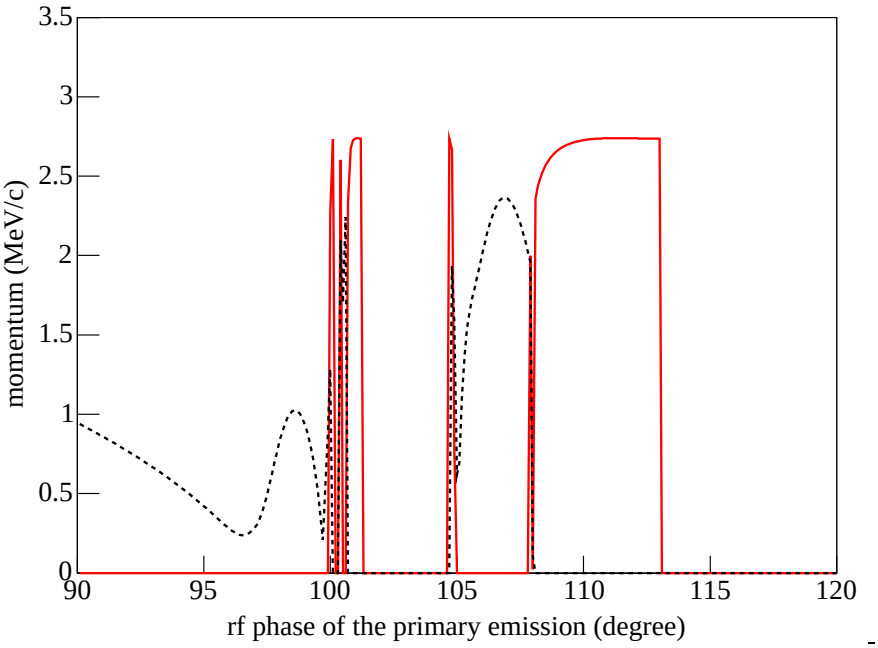

Figure 4.5: Electron dynamics simulation for photo-emitted electrons (black, dotted line). The momentum of the electron has been calculated at the exit of the gun. When secondary electrons are produced, the mean momentum of the secondary electrons is plotted (red, full line).

gain a low momentum (∼2.3 MeV/c). On the other hand, the impact energy is very small (∼28 keV) so that the secondary electron yield is about two. At a rf phase just below 113°, the secondary electrons gain the maximum momentum because they start at an rf phase close to 0°. But the impact energy is too high to make a large number of secondary electrons. Above 113° secondary electrons cannot be extracted from the cathode due to the negative impact phases.

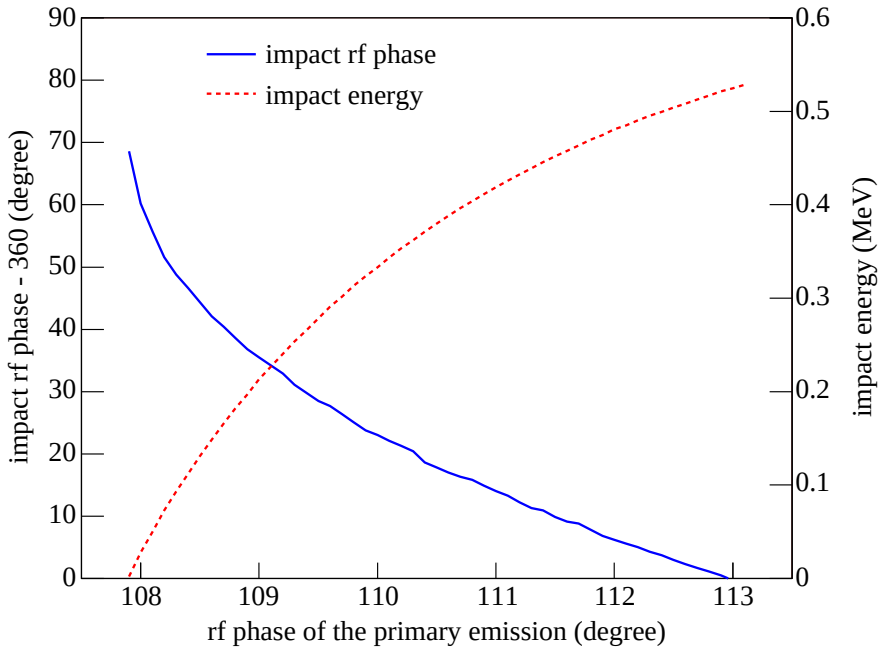

Figure 4.6: A simulation of the primary electron energy and the impact rf phase as a function of the primary emission phase.

4.1.2 Electron beam dynamics

Figure 4.7 shows measurements of the beam charge and the mean momentum as a function of the emission phase in comparison to an ASTRA simulation. For the charge measurement, the Faraday cup located 0.78 m downstream of the cathode has been used. For the momentum measurements, the spectrometer dipole 3.45 m downstream and the YAG screen in the dispersive section have been used.

Compared to the single electron dynamics discussed in Sec. 4.1.1 additional effects have to be taken into account:

(i) The temporal length of the laser pulse wipes out sharp structures in the dependence of parameters on the emission phase. Fine structures in the phase range between 100° and 120° can not be resolved. Around 0° the tail of the electron bunch which is generated by the laser pulse can already be extracted, while the head cannot escape from the cathode yet.

(ii) The quantum efficiency of the cathode shows a gradient dependence due to the Schottky effect [61], therefore the charge extraction increases somewhat within the phase range of 0° to 90°.

(iii) For high phases above 90° the transverse rf focusing tends to over-focus the electron beam and a fraction of the electrons gets lost due to the limited aperture of the beam pipe.

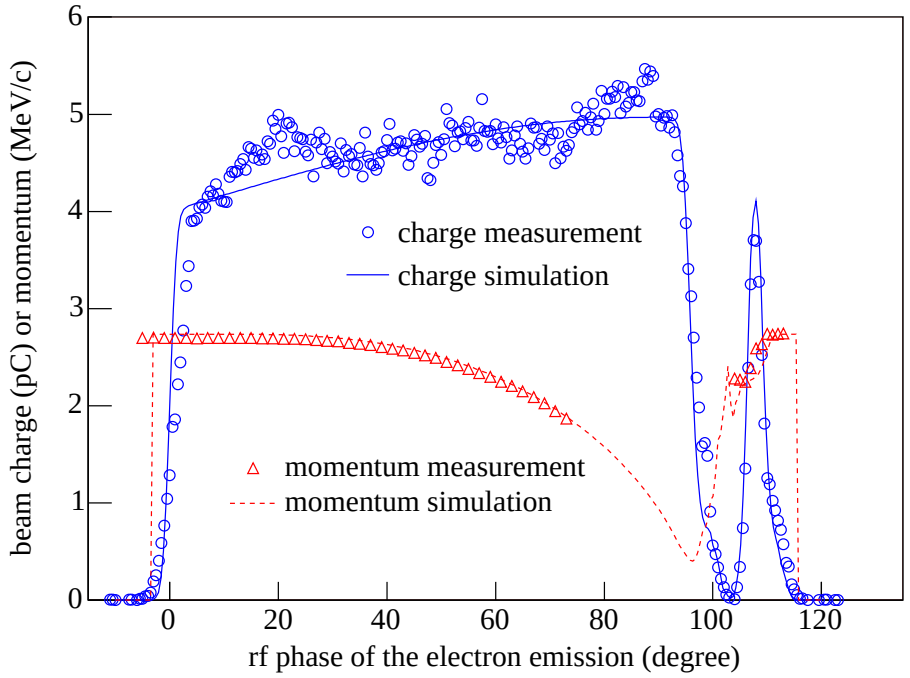

Figure 4.7: Beam charge and momentum as a function of the emission phase.

For the simulations of Fig. 4.7 a flat-top transverse laser profile with an rms radius of 0.47 mm and a Gaussian temporal laser profile with an rms size of 2.2 ps were used in order to generate the photoemitted electron beam for the particle tracking simulation. The measured transverse laser size was 0.44 mm rms for the horizontal direction and 0.51 mm rms for the vertical direction. The transverse laser profile was measured with a CCD camera in an image plane which has the same distance and optics to the laser source as the photocathode. The temporal laser size was measured to be ∼2.3 ps rms with a streak camera which has 2 ps resolution. For the beam charge dependence on the rf phase, a Schottky effect was modeled with the formula [61]: $Q \propto (4.0 + 0.045 \cdot E_{\mathrm{rf+sc}}\ [\mathrm{MV/m}])\ [\mathrm{pC}]$, where $E_{\mathrm{rf+sc}}$ is the actual electric field (rf + space charge) in the center of the cathode.

Figure 4.8 displays beam trajectories at characteristic emission phases in the case of maximum field of 21.6 MV/m. At 5° the electron beam can be fully extracted, due to the laser pulse length of ∼2.3 ps (∼1° in the rf phase) rms Gaussian, and smoothly accelerated because it is synchronized to the rf field in the full cell and hence gains its maximum momentum. At 90° the electron beam is decelerated and then accelerated again in the full cell. At this phase the transverse rf focusing is optimal to send the beam down the beam line. At 96° electrons are further decelerated and over-focused by the rf field, therefore about a half of the electrons get lost at an aperture. At 104° all emitted electrons return and disappear in the backplane of the cavity. At 108° a fraction of the electrons moves back to the cathode, to disappear or to produce secondary electrons, depending on the impact energy. The other fraction of the primary electrons which have a small difference in emission phase and trajectory, barely survives and flows out of the cavity with secondary electrons.

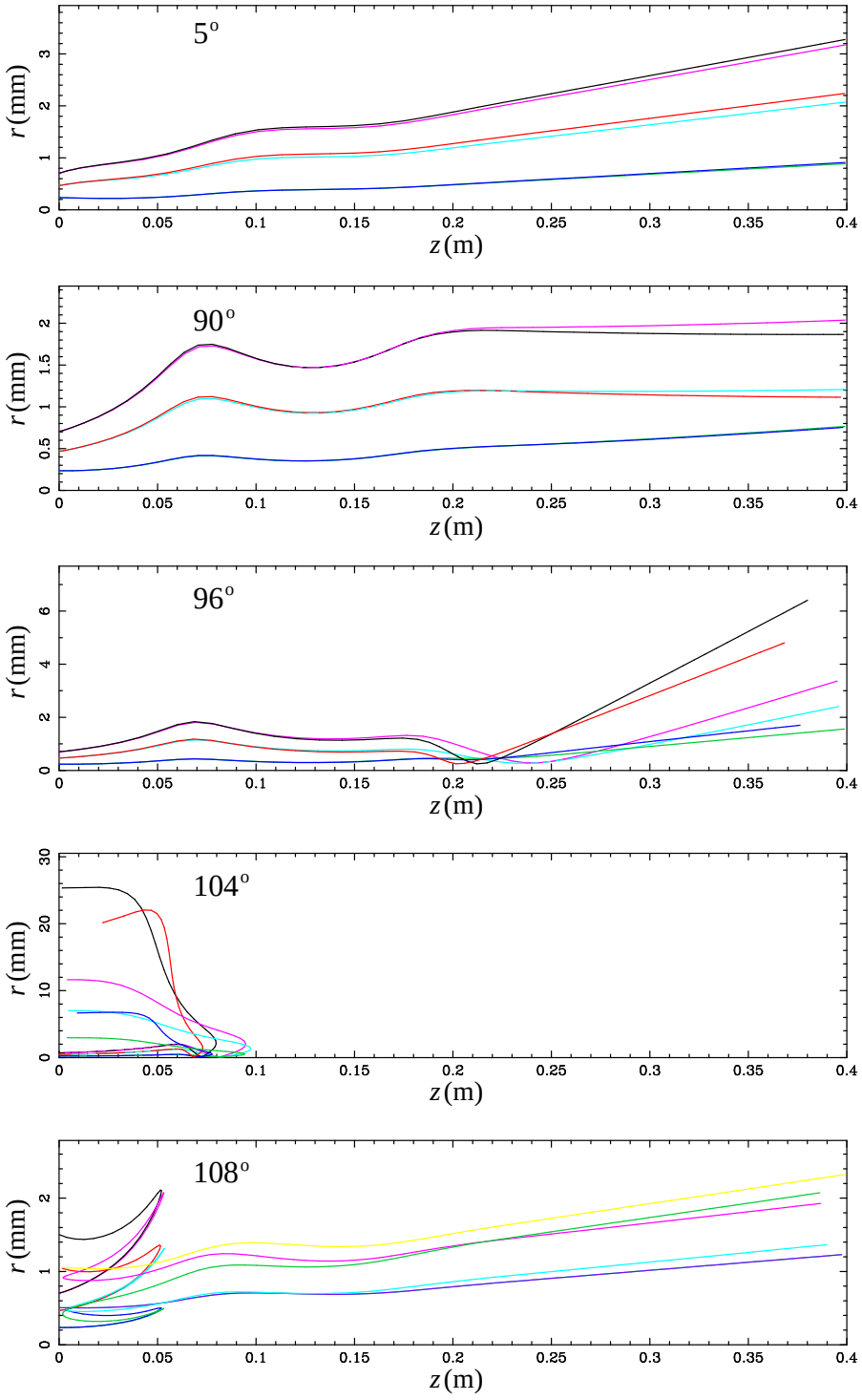

Figure 4.8: Beam trajectories at characteristic emission phases.

4.1.3 Secondary emission in electron dynamics

The secondary emission yield is strongly dependent on the surface status of the emissive material. During the gun operation, a quantum efficiency change of the Cs_2Te photocathodes from ~7% to ~0.5% was observed. Measurements presented here are done at a quantum efficiency of ~1.5%. For the measurements in the following section cathode #500.1 [12] has been used. The maximum secondary yield δ_{max} in Eq. 3.12 and the corresponding primary electron energy $E_{p,\,max}$ are assumed to be 7.0 and 2.2 keV, respectively. The fit parameter s is set to 1.5. With these parameters the measurement results obtained with cathode #500.1 can be nicely matched as will be shown below.

As discussed in Sec. 4.1.2 (Fig. 4.7 and 4.8), the charge bump appearing between 100° and 120° is composed of both, primary and secondary electrons. Figure 4.9 shows the bump in more detail in order to distinguish the electron sources clearly. The simulation for the sum of the primary and secondary electrons was fit to the measurement with optimizing the secondary emission parameters. From the simulation result, the primary electrons range from about 103° to about 111° and the secondary electrons from about 105° to about 115°.

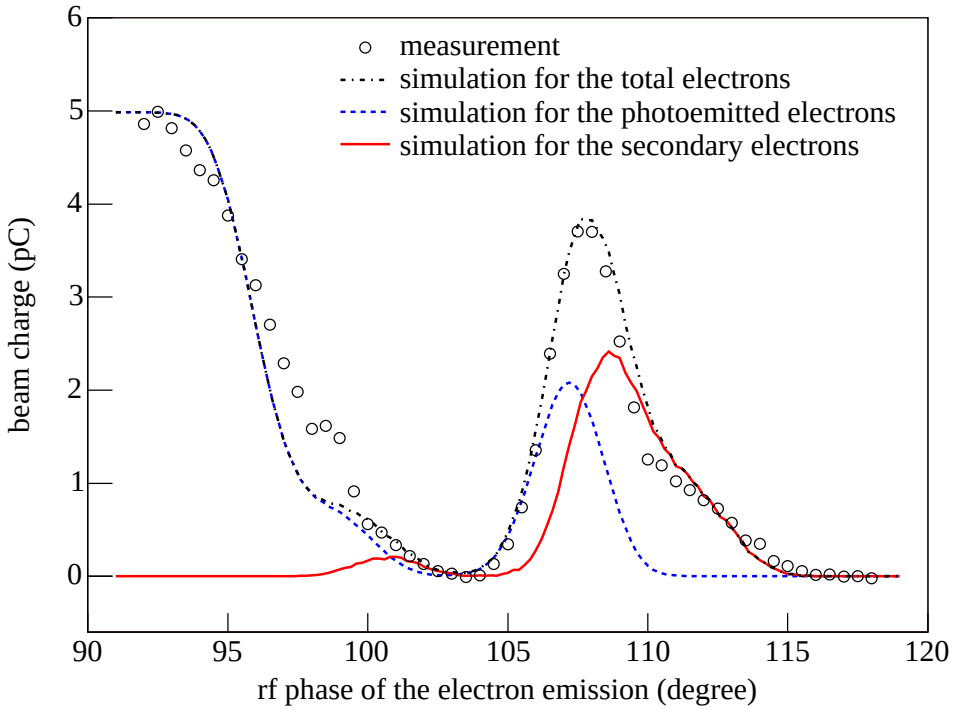

Figure 4.9: Beam charge at the bump. In the simulation, the primary electrons and the secondary electrons are distinguished.

The momentum distributions of the bump as a function of the emission phase was investigated experimentally. A main solenoid field of 0.075 T (peak value) was applied in order to focus the electron beam onto the YAG screen in the dispersive section. The measured momentum distributions at a series of phases are plotted in Fig. 4.10. Two characteristic momenta were detected. For the lower phases (105° and 106°) the beam momentum is ∼2.37 MeV/c. For the higher phases (111° – 114°) ∼2.74 MeV/c has been measured. Between 107° and 109°, a continuous transition of the height of the two peaks from the lower momentum peak to the higher momentum peak has been observed.

Simulations were made to study this splitting of the two peaks in the momentum distribution (Fig. 4.11). The simulations show that the lower momentum peaks

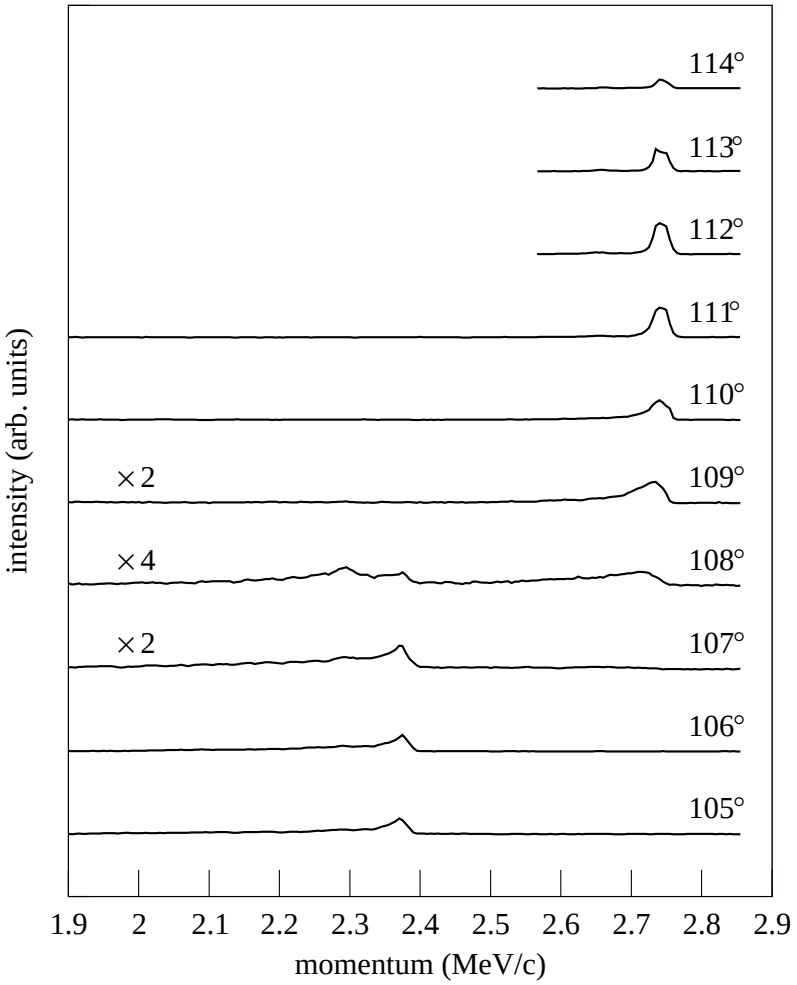

Figure 4.10: Series of momentum measurements for the phase range of 105° to 114°. Cathode #500.1 was used for this momentum measurement.

have their origin in electrons produced directly by the laser pulse and the higher momentum peaks originate from the secondary electrons. These secondary electrons have a higher momentum because the emission phases of the secondary electrons, (i.e., impact phases of the primary electrons with the assumption of no delay time) correspond to the rf phases for maximum momentum gain (see Fig. 4.6). Broader peaks in the momentum measurements than in the simulations result mainly from an rf power jitter of about 2% [62] during the accumulation of the electron beam images on the YAG screen. For each measurement the images of 50 electron bunches were integrated on the YAG screen.

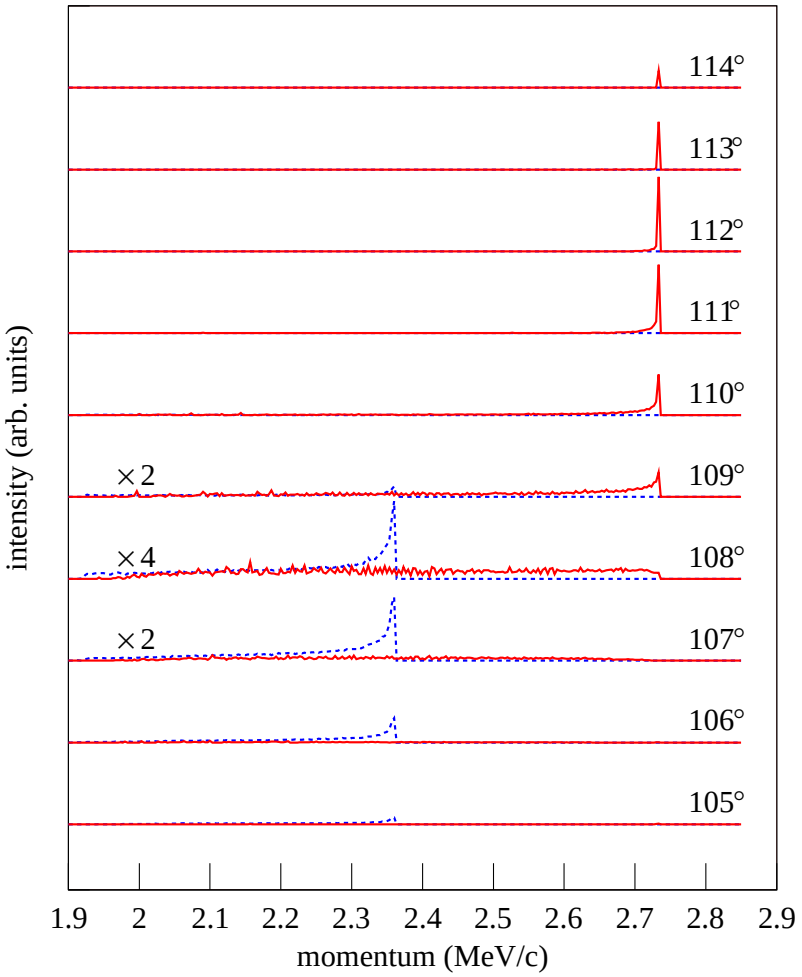

Figure 4.11: Simulation of the momentum distribution in the phase range of 105° to 114°. The electrons generated by the laser pulse (blue, dashed lines) and the secondary electrons (red, full lines) are shown separately.

Dependence on cathode parameters

In order to study the dependence of the secondary emission properties on cathode parameters, another cathode, #61.1 [12], has been used for additional charge and momentum measurements. Cathode #61.1 has been produced following the same procedure and with the same geometry as cathode #500.1 except for the Cs_2Te film thickness which is only 20 nm as compared to 60 nm for cathode #500.1. The quantum efficiency of cathode #61.1 was about 0.5% (∼30% of the quantum efficiency of cathode #500.1) during the measurements discussed here. To compensate the difference in the quantum efficiency for the two cathodes, the energy of drive-laser pulse has been adjusted so that the bunch charge in the phase range which is independent of the secondary electrons, between 0° and 90°, was the same for both cathodes. The measurements for the two cathodes are plotted in Fig. 4.12. There is a great similarity except for the bump which is lower for cathode #61.1 than for cathode #500.1.

Figure 4.13 compares the measurements of both cathodes in the phase range of interest and shows a simulation matched for cathode #61.1. For the simulation the

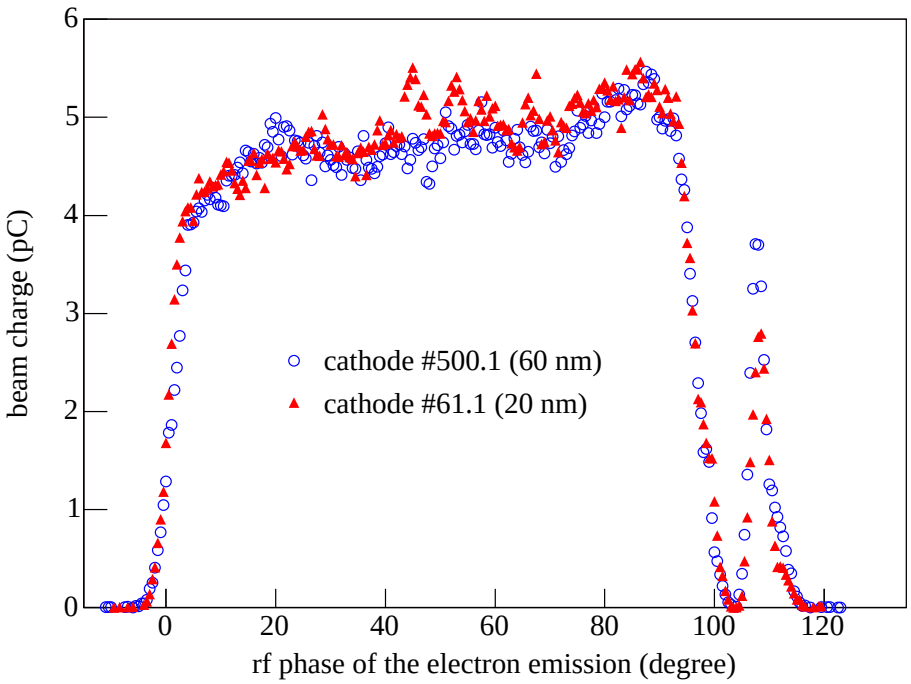

Figure 4.12: Comparison of the bunch charges depending on the emission phase for cathode #61.1 and cathode #500.1. The energy of drive-laser pulse has been adjusted to get the same bunch charge for the two cathodes in the phase range between 0° and 90°.

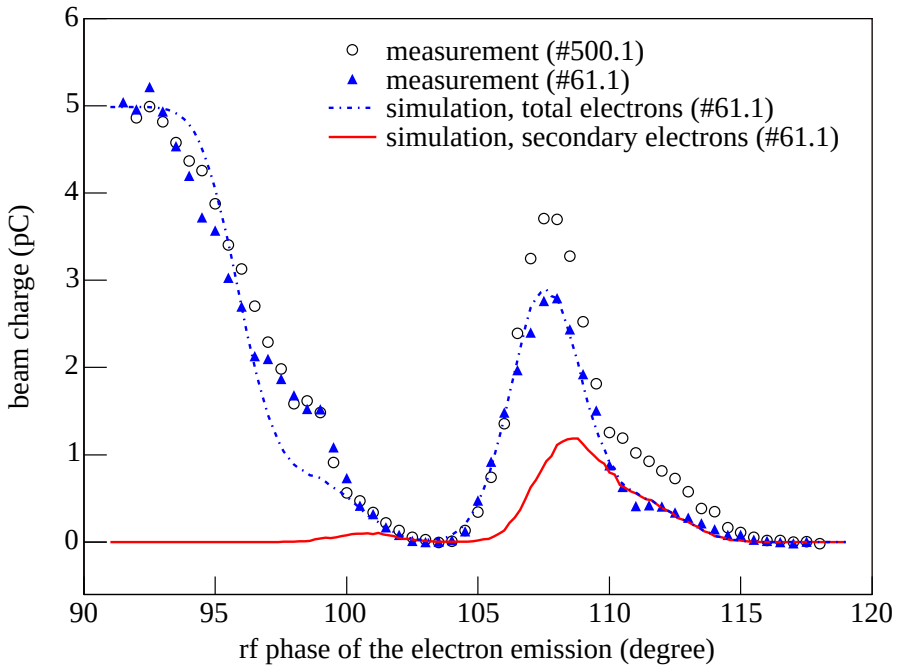

Figure 4.13: Comparison of the bunch charges at the bump for cathode #61.1 and cathode #500.1.

maximum secondary emission yield $\delta_{\max}$ was reduced from 7.0, as it was used in the simulations discussed above, to 4.5 while keeping the other parameters (for the secondary electron generation and also for the operating condition of the gun) fixed.

Momentum measurements for cathode #61.1 (as shown in Fig. 4.14): The principal characteristics are identical to cathode #500.1, but the measured intensity at the higher momentum peak, corresponding to secondary electrons, is lower for cathode #61.1.

The cathode with the thicker Cs_2Te coating is expected to have a higher secondary emission yield especially for primary electrons with impact energies higher than 1 keV [63]. The lower quantum efficiency of cathode #61.1 may be related to the cathode thickness, which is in the order of the photon absorption length as well as the electron escape depth, but may also be influenced by the surface status of the cathode. Cs_2Te has a low electron affinity of $\sim$0.2 eV, which allows the photo-excited electrons to easily overcome the potential barrier at the surface. Adsorbates on the cathode surface, which built up due to the vacuum conditions in the gun, can increase the electron affinity and hence reduce the quantum efficiency. As discussed in Sec. 3.3, the electron affinity plays an important role in the secondary emission process as well.

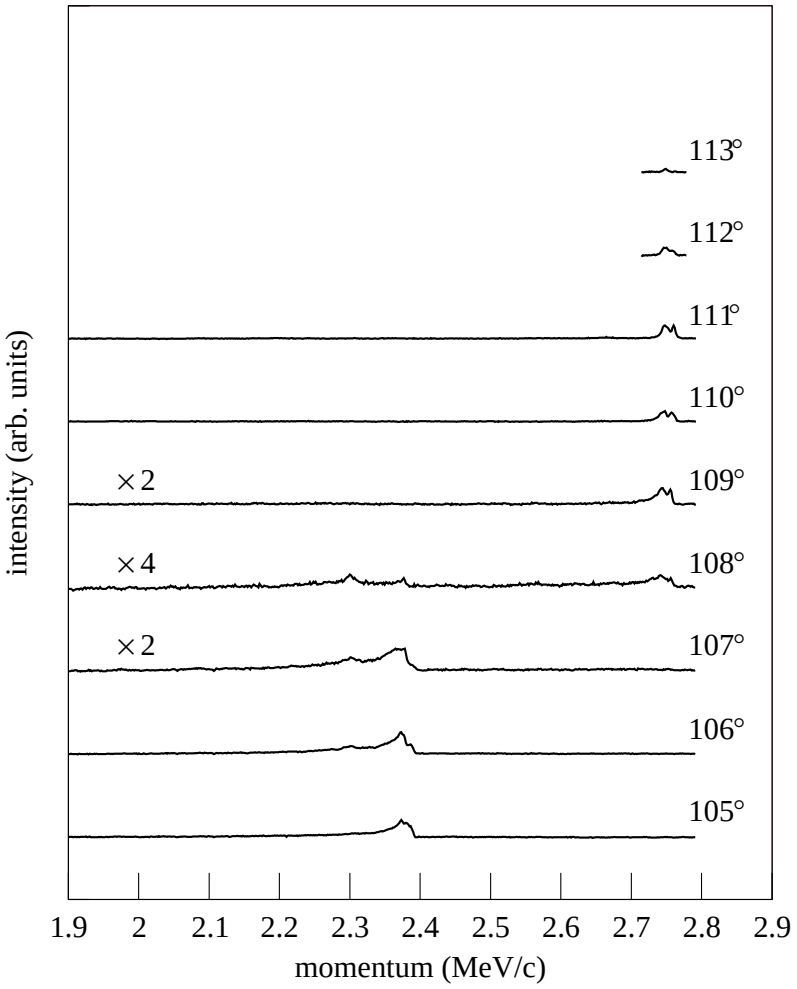

Figure 4.14: Series of momentum measurements for cathode #61.1.

Dependence on gun gradient

At impact energies below $E_{p,\max}$, the electron penetration depth increases with the impact energy of the primary electron E_p and secondary electrons are generated within the range of the escape depth. As the impact energy increases further beyond $E_{p,\max}$, the penetration depth exceeds the escape depth so that some of the generated secondary electrons cannot reach the surface and the secondary yield decreases with E_p. This behavior is found in Fig. 4.15. At the lowest gradient (22.9 MV/m) the bump composed of the photoemission and the secondary emission is relatively high, which means the impact energy of the primary is close to $E_{p,\max}$. As the gradient increases, the impact energy becomes larger than $E_{p,\max}$. As the result, the height of the bump becomes lower.

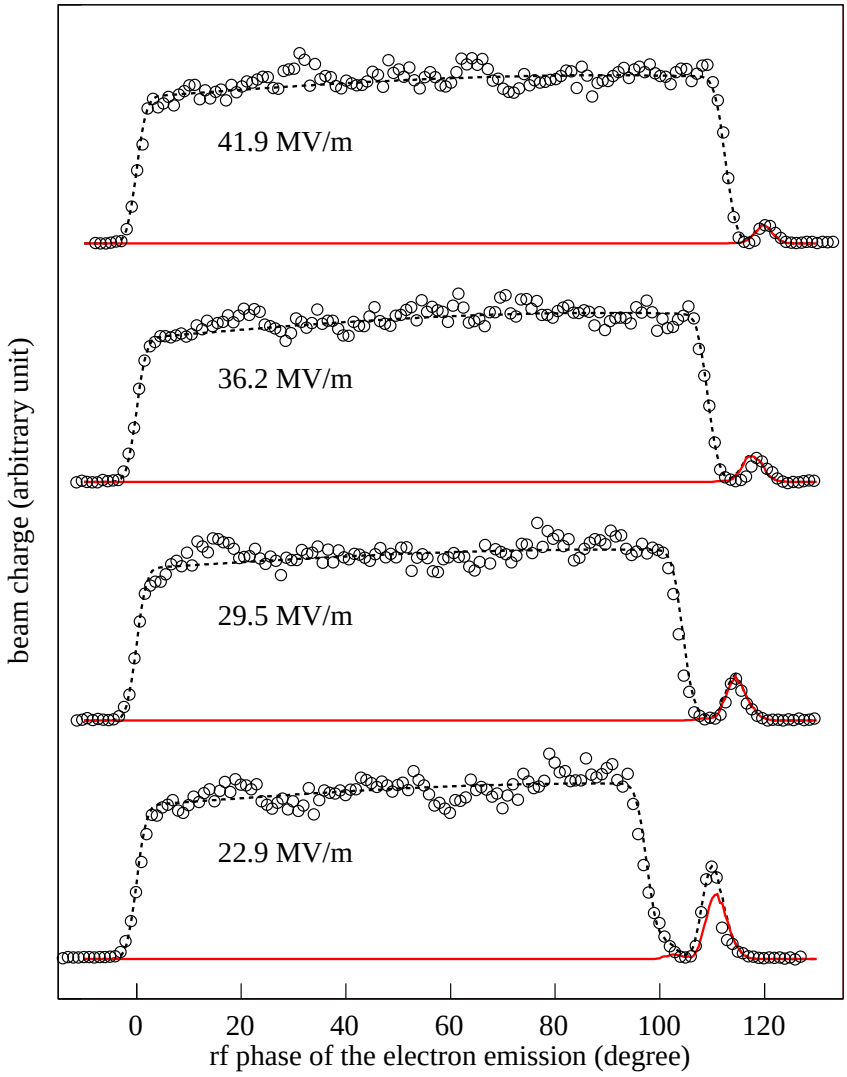

Figure 4.15: Beam charge vs. rf phase of the electron emission at several rf input power levels for the beams with small bunch charge of max. 9 pC. Measurements (circle) are shown with the corresponding simulations (line). The simulation results are distinguished for all electrons (black dotted line) and only for secondary electrons (red full line)

4.1.4 Effective photoemission for low charge beams

Because of the rf field at the cathode during electron emission, the properties of the cathode change. The properties change makes the electrons generated by the drive-laser pulse change with the rf field strength as well. Here, a limitation in measurement of the delay time of photoemission is discussed shortly. And then, one attempt to estimate the electron affinity variation with the rf field is discussed with the extracted bunch charge and the kinetic energy of the electrons.

Delay time of photoemission

In the charge measurement as a function of the emission phase (see Fig. 4.7 and 4.15), the charge variation around 0° include, in principle, information about the temporal pulse shape of the drive-laser [64] and the delay time of the photoemission.

From the discussion in Sec 3.2, the emission time of the photoelectrons generated by the drive-laser is much shorter than a time (2.14 ps) corresponding to 1° of the rf phase. This means that the delay time does not influence the initial profile of the electron beam extracted from the cathode.

Schottky effect - bunch charge increase with the rf gradient

Figure 4.15 shows beam charge measurements as a function of the emission phase for different rf gradients. The measurements were performed with cathode #43.2 when the cathode had no damage in November 2004. A short (3 ps rms) Gaussian laser pulse was used to produce a small bunch charge (max 9 pC) in order to reduce the space charge force. The bunch charge has been measured with the Faraday cup 0.78 m downstream from the cathode and the data have been read with an oscilloscope in the control room. Due to the small signal-to-noise ratio for low charge measurements, the error is of the order of several percent of the average value at each measurement point. The beam charge was measured as a function of the emission phase by scanning the timing of the laser pulse with respect to the rf phase.

Around 0°, the increase of the bunch charge is mainly caused by the pulse shape of the drive laser [64]. The rf phase instability of about 2° [62] reduces the slope somewhat. The bunch charge increases slowly up to an rf phase of ∼90°. After ∼90°, the electrons cannot be effectively accelerated by the rf field due to a strong phase slippage and they hit apertures, composed of the gun cavity, the coaxial coupler, and the beampipe, and disappear.

The corresponding simulation (dotted black line in Fig. 4.15) includes the photoemitted electrons as well as the secondary electrons. The secondary electrons (solid red line) are also shown separately.

With an increase of the rf field strength at the Cs_2Te cathode, a potential barrier defined by the electron affinity E_A is lowered and, as the result, the probability of electron extraction is increased. This is called the Schottky effect.

Spicer has derived a relation for the photoemissions [39] based on a three-step model. The field dependence of the photo-emitted bunch charge is predicted to be:

$$Q_{\mathrm{bunch}} = \frac{G\left[h\nu - (E_{\mathrm{A}} + E_{\mathrm{G}})\right]^{\frac{3}{2}}}{\left[h\nu - (E_{\mathrm{A}} + E_{\mathrm{G}})\right]^{\frac{3}{2}} + \Gamma}, \tag{4.1}$$

where E_{G} is the band gap energy and G and Γ are fit parameters to be determined from the experimental data. The photon energy $h\nu$ of the drive-laser pulse is 4.75 eV in this study. In the original application of Eq. 4.1 by Spicer, the QE has been measured by changing the photon energy $h\nu$ while keeping E_{A} and E_{G} constant. In this study, the photon energy and E_{G} are kept constant and E_{A} is searched with a fit.

The effective electron affinity change during the gun operation is illustrated in Fig. 4.16. the QE of Cs_2Te cathodes monotonically decreases down to $\sim$1 %. It can be explained by an increase of the electron affinity by $(\kappa - 1)E_{\mathrm{A},0}$, where $E_{\mathrm{A},0}$ is the electron affinity when a cathode is very fresh and κ is a parameter introduced to describe "poisoning". The poisoning parameter κ is close to 1 when the cathode is fresh and becomes greater with poisoning.

On the other hand, under the influence of an rf field, the Schottky effect lowers the electron affinity E_{A} by an amount of $\sqrt{\frac{e^3}{4\pi\epsilon_0}\beta_{\mathrm{ph}}E_{\mathrm{emit}}}$ [28], where E_{emit} is the

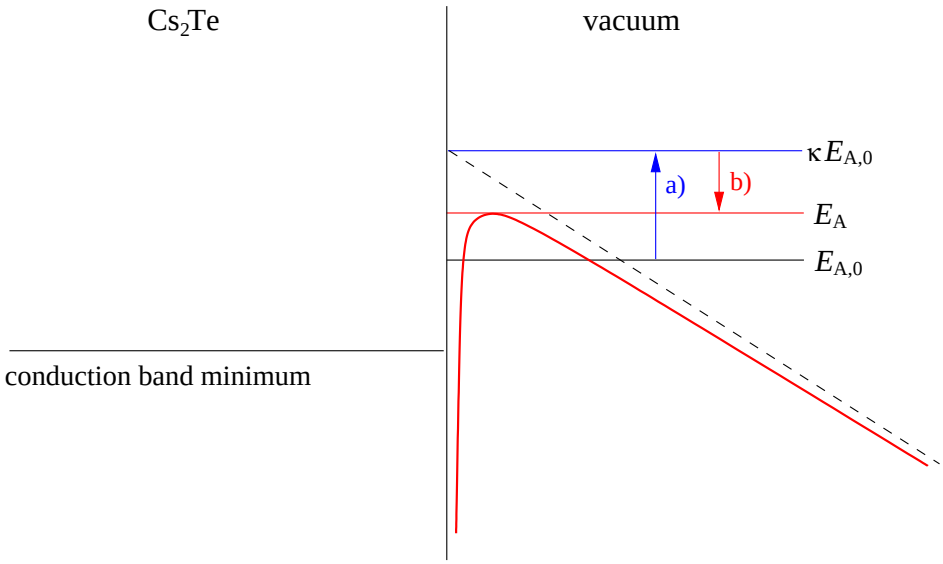

Figure 4.16: Effective electron affinity change during the gun operation. a) increase of the potential barrier by $(\kappa - 1)E_{\mathrm{A},0}$ due to poisoning. b) decrease of the potential barrier by $\sqrt{\frac{e^3}{4\pi\epsilon_0}\beta_{\mathrm{ph}}E_{\mathrm{emit}}}$ under the influence of an rf field.

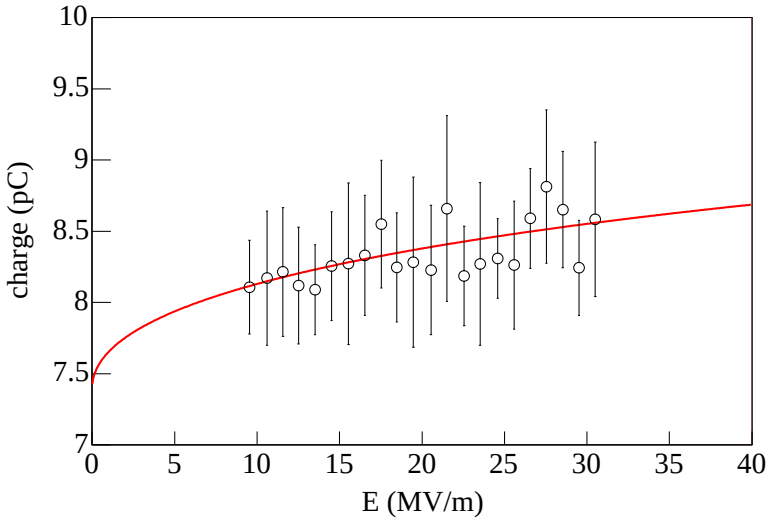

Figure 4.17: Beam charge vs. the rf field strength at the time of emission. The emitted beam charges have been collected by scanning the emission phase at several rf input power levels. A fit has been made using Eq. 4.1 and 4.2.

rf field strength at the time of emission, and $\beta_{\rm ph}$ is the field enhancement factor for photoemission. $\beta_{\rm ph}$ includes geometrical effects and the polarization of the Cs_2Te film. Therefore, $E_{\rm A}$ in Eq. 4.1 is expressed as

$$E_{\rm A} = \kappa E_{\rm A,0} - \sqrt{\frac{e^3}{4\pi\epsilon_0}\,\beta_{\rm ph}\,E_{\rm emit}}\,. \tag{4.2}$$

For the emission phase between 10° and 80° at the four different rf strength cases in Fig. 4.15, the beam charges were collected and plotted in Fig. 4.17 to find the fit parameters, κ, $\beta_{\rm ph}$, G, and Γ in Eqs. 4.1 and 4.2. The fit has been made using Eq. 4.1 and 4.2: $\kappa = 2.2$, $\beta_{\rm ph} = 3$, $G = 11.7$, and $\Gamma = 0.59$. In Fig. 4.17 the fit line is extended to zero electric field. It shows that the increase of the bunch charge in the 0 – 4 MV/m range is ∼8 % with 262 nm photon wavelength. Coleman [65] reported ∼13 % increase at the same field strength range with 254 nm photon wavelength. This discrepancy is possibly due to a slightly different Cs-Te composition or a different status of the surface. The large measurement error and missing data points at the low rf field strength can contribute to the discrepancy as well.

Kinetic energy distribution – Thermal emittance

An electron in the material can be emitted into the vacuum when the electron has an energy higher than or equal to the vacuum level ($E_{\rm vac}$ in Fig. 3.3). In the Cs_2Te cathode, electrons excited by the drive-laser are located 0.75 eV above the conduction band minimum with the highest probability (see Sec. 3.2). When the electron is emitted into the vacuum, the energy of the electron shifts from the highest

probability state (0.75 eV above the conduction band minimum) to the vacuum level which is same as the electron affinity (0.2 eV above the conduction band minimum of Cs_2Te). Therefore, the kinetic energy of the electron in the vacuum will be equal to the energy difference between the two levels, i.e. $E_{\mathrm{kin}} = 0.75\,\mathrm{eV} - 0.2\,\mathrm{eV} = 0.55\,\mathrm{eV}$.

The thermal, or initial, emittance of an electron beam determines a lower limit for the normalized emittance of the beam generated by a photoinjector [37]. The thermal emittance characterizes the phase space area occupied by the electron beam immediately after the emission. The normalized rms emittance for a transverse direction, here x-direction, is defined as [66]

$$\varepsilon_{n,\mathrm{rms}} = \frac{1}{m_0 c}\sqrt{\langle x^2\rangle\langle {p_x}^2\rangle - \langle x\,p_x\rangle^2}, \tag{4.3}$$

where $\langle\ \rangle$ defines the second central moment of the particle distribution and m_0 is the rest mass of an electron. At the cathode, there is no correlation between the coordinate and the momentum of the emitted electrons, hence the term $\langle x\,p_x\rangle$ in Eq. 4.3 is zero. Therefore, the normalized rms emittance can be simplified as [66]

$$\varepsilon_{n,\mathrm{rms}} = x_{\mathrm{rms}}\,\frac{p_{x,\mathrm{rms}}}{m_0 c}. \tag{4.4}$$

For an electron with total momentum p, the transverse momentum p_x is given by

$$p_x = p\sin\theta\cos\phi, \tag{4.5}$$

where $\theta = [0,\,\theta_{\mathrm{max}}]$ and $\phi = [0,\,2\pi]$ are the polar and the azimuthal angles, respectively. The rms value of the transverse momentum can be calculated with the following relation:

$$p_{x,\mathrm{rms}} = \sqrt{\frac{\int\int {p_x}^2\sin\theta\,d\theta\,d\phi}{\int\int \sin\theta\,d\theta\,d\phi}}. \tag{4.6}$$

Since the kinetic energy of the emitted electron is of the order of 0.55 eV as discussed above, the emitted electron is non-relativistic. Therefore, the momentum can be approximated as

$$p = m_0 c\sqrt{\frac{2E_{\mathrm{kin}}}{m_0 c^2}}. \tag{4.7}$$

When it is assumed that the electrons are emitted isotropically into the half-sphere over the cathode, the maximum polar angle θ_{max} is set to $\pi/2$. The thermal (normalized rms) emittance is written as [66]

$$\varepsilon_{n,\mathrm{rms}}^{\mathrm{therm}} = r_{\mathrm{rms}}\sqrt{\frac{2\,E_{\mathrm{kin}}}{m_0 c^2}}\,\frac{1}{\sqrt{3}}, \tag{4.8}$$

where r_{rms} is a generalized coordinate for a transverse direction, i.e. either x_{rms} or y_{rms}.

From the emittance measurement with minimized space charge emittance and rf emittance, the thermal emittance can be obtained. The measured thermal emittance gives an information on the kinetic energy of the emitted electron, that is, on the potential barrier defined by the electron affinity of the emissive material. The measurement procedure of the thermal emittance is described in detail in Ref. [24].

When the rf field is applied at the cathode, the vacuum level is bent downward (see Fig. 3.1 and 4.16). Therefore, the potential barrier decreases and the kinetic energy of the emitted electrons gets higher. The thermal emittance, as the result, increases with the rf field strength at the cathode (Fig. 4.18). During the rf gun operation, the Cs_2Te cathode is exposed to a non-ultrahigh vacuum environment because of the field emission induced by the rf field. Therefore, the electron affinity increases and the kinetic energy of the electron decreases.

The measurement has been performed with a small charge (3 pC) electron beam generated by a short laser pulse (3 ps rms Gaussian), in order to reduce the space charge emittance as well as the rf emittance. The space charge emittance is defined as a contribution of the space charge force which expands the phase space volume of the electron bunch by the interactions of the electrons in the bunch. The rf emittance comes from the inhomogeneity of the rf field in the gun cavity and also from the finite range of the emission phase.

The measured emittance $\varepsilon_{\mathrm{meas}}$ (black circle in Fig. 4.18) includes the above contributions as

$$\varepsilon_{\mathrm{meas}} = \sqrt{\left(\varepsilon_{\mathrm{meas}}^{\mathrm{therm}}\right)^2 + \left(\varepsilon^{\mathrm{rf}}\right)^2 + \left(\varepsilon^{\mathrm{sc}}\right)^2 + \left(\varepsilon_{\mathrm{slit.meas}}^{\mathrm{sys.error}}\right)^2}, \tag{4.9}$$

where $\varepsilon_{\mathrm{meas}}^{\mathrm{therm}}$ is the measured thermal emittance, $\varepsilon^{\mathrm{rf}}$ is the rf emittance, $\varepsilon^{\mathrm{sc}}$ is the space charge emittance, and $\varepsilon_{\mathrm{slit.meas}}^{\mathrm{sys.error}}$ is possible systematic error in slit measurements.

The measured thermal emittance $\varepsilon_{\mathrm{meas}}^{\mathrm{therm}}$ is divided into a theoretical thermal emittance $\varepsilon_{\mathrm{theory}}^{\mathrm{therm}}$ defined by Eq. 4.8 and a discrepancy parameter η,

$$\varepsilon_{\mathrm{meas}}^{\mathrm{therm}} = \eta\, \varepsilon_{\mathrm{theory}}^{\mathrm{therm}}. \tag{4.10}$$

η parameterizes the discrepancy between the measurements and the theoretical values. For the theoretical calculation with Eq. 4.8, the kinetic energy of the emitted electrons E_{kin} is assumed to be the value defined by the energy difference between the highest probable state in the conduction band of Cs_2Te and the vacuum level. But, in reality, the kinetic energy has a certain distribution. The discrepancy parameter η may also come from mechanical roughness and non-uniform QE of the cathode surface, laser jitter (intensity and position at the cathode), measurement errors of the laser spot size, and rf jitter (power and phase). In this study, η has been fitted to be 1.34 as shown in Fig. 4.18.

The rf emittance $\varepsilon^{\mathrm{rf}}$ originates from the finite size of the electron bunch in the rf field. In Fig. 4.18, $\varepsilon^{\mathrm{rf}}$ has been numerically calculated with ASTRA with the machine parameters for each measurement points assuming that the center of the

beam perfectly coincides the electrical center of the gun cavity. At PITZ, a beam based alignment within 0.2 mm error is always performed before starting emittance measurements [67]. The contribution of such a misalignment to the emittance is negligibly small, about 1%, according to ASTRA simulation.

The space charge emittance $\varepsilon^{\mathrm{sc}}$ can be ignored when a very small beam charge is used. In this study, 3 pC charge has been used.

The systematic error in the slit measurements $\varepsilon^{\mathrm{sys.error}}_{\mathrm{slit.meas}}$ is hard to clearly separate from η. In this study, it has been set to 0.2 mm mrad according to an analysis of the position jitter of the beamlets.

In Fig. 4.18, one line from the theoretical calculation using Eq. 4.8 is shown. For this calculation, the electron affinity change due to poisoning (increase) and the Schottky effect (decrease) is ignored and the discrepancy parameter η is not included. The theoretical thermal emittance (0.46 mm mrad) can be compared to the measurement with a time-of-flight spectrometer by Sertore *et al.* [60].

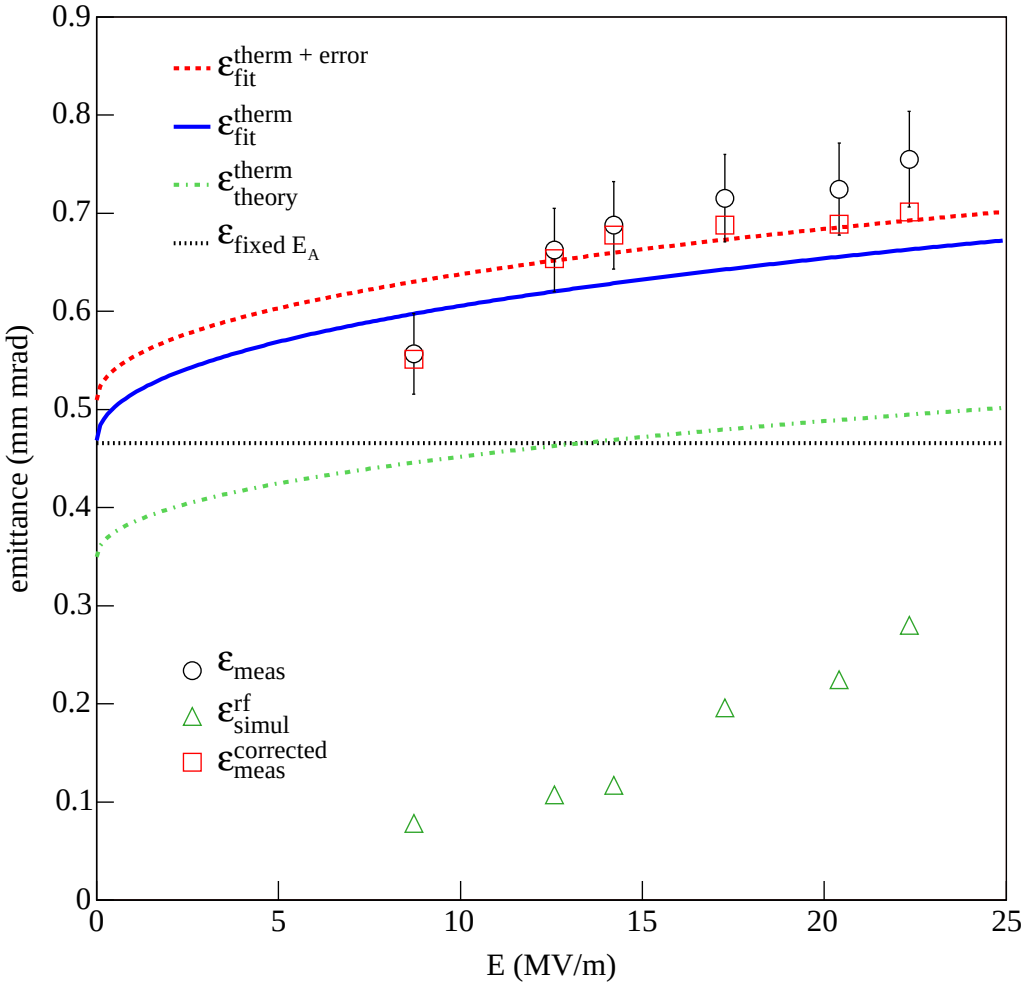

Figure 4.18: Transverse emittance at 0.55 mm rms size of the laser pulse and 3 pC bunch charge vs. the rf field strength. For the measurement, the gun gradient was changed and the emission phases ϕ_{emit} was optimized in order to achieve the highest momentum for each gradient. The rf field strength was obtained by multiplying the gradient with $\sin\phi_{\mathrm{emit}}$. The rf emittance $\varepsilon^{\mathrm{rf}}$ (△) has been numerically calculated with ASTRA and subtracted quadratically from the measured emittance $\varepsilon_{\mathrm{meas}}$ (◯) in order to find a corrected emittance $\varepsilon_{\mathrm{meas}}^{\mathrm{corrected}}$ (□). This corrected emittance includes the measured thermal emittance $\varepsilon_{\mathrm{meas}}^{\mathrm{therm}}$ and possible systematic error in slit measurements $\varepsilon_{\mathrm{slit.meas}}^{\mathrm{sys.error}}$. A theoretical estimation $\varepsilon_{\mathrm{theory}}^{\mathrm{therm}}$ (-·-·-) has been analytically calculated using Eq. 4.10. In order to make a fit to the measurement ($\varepsilon_{\mathrm{meas}}^{\mathrm{therm}}$), a discrepancy parameter η has been multiplied to the theoretical value ($\varepsilon_{\mathrm{theory}}^{\mathrm{therm}}$) and the result $\varepsilon_{\mathrm{fit}}^{\mathrm{therm}}$ has been plotted. The final fit $\varepsilon_{\mathrm{fit}}^{\mathrm{therm+error}}$ (- - -) has been made with considering $\varepsilon_{\mathrm{slit.meas}}^{\mathrm{sys.error}}$. Another theoretical value using Eq. 4.8 with fixed E_{A} ($\kappa E_{\mathrm{A},0}$ = 0.44 eV) is shown (····) for comparison.

4.2 Beam dynamics for normal operating conditions

Since PITZ aims to produce high quality electron beams with a small transverse emittance in parallel with a short bunch length as required for FEL operation, 1 nC electron beams are normally generated for the characterization of the beam parameters. Electron beams with 1 nC bunch charge are strongly influenced by the space charge force when the beams are not in the relativistic regime. In order to reduce the space charge force, the electron bunch length is about 20 ps immediately after emission from the photocathode and the short bunch length is achieved with bunch compressors after a further acceleration. The initial temporal profile of the electron bunch is controlled by the profile of the drive-laser pulse. Therefore, in addition to the emission mechanism depending on the emission phase, the space charge force and the finite laser pulse length should be considered when the electron beam dynamics is studied. In this section, the electron emission processes and the beam dynamics at the normal operating conditions are studied with cathode #500.1 (60 nm Cs_2Te thickness).

4.2.1 Beam dynamics dependence on emission phase

For high charge beams, the dynamics dependence on the emission phase is more complicated than for low charge beams. Figure 4.19 shows measurements of the beam charge and the mean momentum as a function of the emission phase. ASTRA simulations are shown as well. The beam charge has been measured with the first ICT (0.9 m downstream) and beam momentum has been measured with the spectrometer dipole. The measurement methods for the charge and the momentum are described in Sec. 4.1.2. The transverse profile of the drive-laser pulse was measured to be flat-top with an rms size of 0.57 mm for the x-direction and 0.59 mm for the y-direction. The temporal laser profile was a flat-top with a full-width-of-half-maximum (FWHM) of 18.5 ps and a rising/fall time of 8.4 ps. For the charge and momentum measurements, the energy of the laser pulse was optimized to get 1 nC of bunch charge at a reference emission phase and was kept constant for the measurements at the other emission phases. At PITZ, the reference emission phase is defined as the phase which allows a maximum momentum gain [67].

Since the laser pulse has a finite length, electron beams start to come out from an emission phase around $-10°$ (see Fig. 4.19). The beam charge increases steeply up to about 35°, and then increases slowly up to about 90°. Above about 90°, the beam charge starts to drop down and becomes strongly dependent on the solenoid current and on the aperture defined by beampipes. The steep increase results from the space charge force and the mirror charge force induced by the beam itself. The emission process of high density beams will be discussed in Sec. 4.2.2. The slow increase after about 35° can be explained with the Schottky effect. Above about 90°, the transverse rf field over-focuses the electron beams and the over-focused beams get lost due to the aperture (more discussion in Sec. 4.1.2). Therefore, the beam charge above 90° depends strongly on the solenoid current and the aperture.

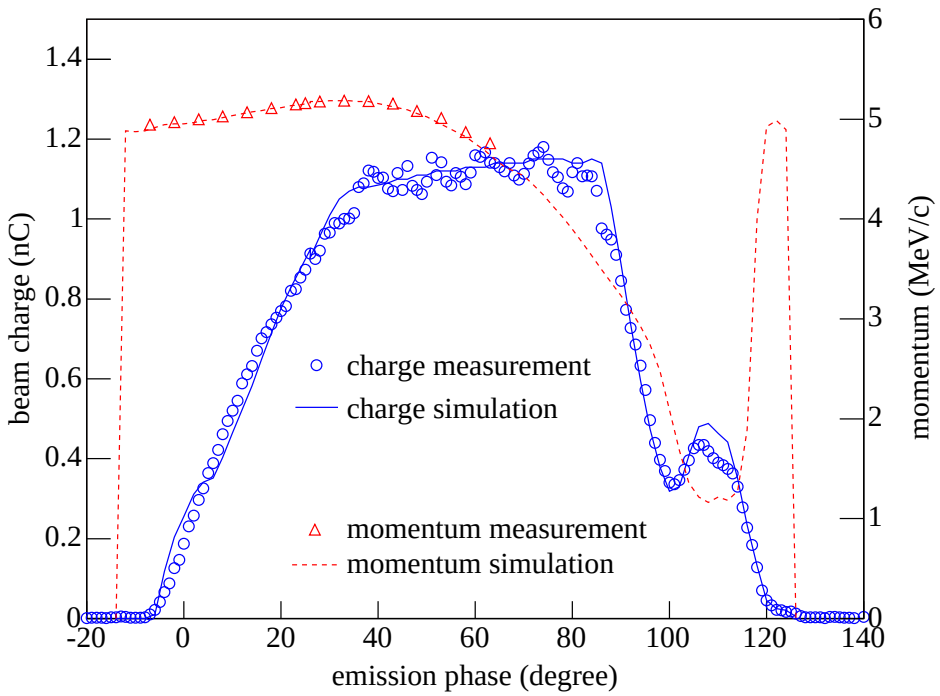

Figure 4.19: Bunch charge and mean momentum vs. emission phase for cathode #500.1 at 45 MV/m of maximum rf field at the cathode. For the charge measurement, the main and bucking solenoid currents were set to 320 A and 24 A, respectively. For the momentum measurement, the solenoid currents were optimized in order to focus the beam to the dispersive arm screen.

According to the simulation, secondary electrons are generated at emission phases around 0° (produced during photoemission dominated by the space charge force and the mirror charge force) and around 120° (produced by hitting the cathode after some trajectory of the photoemitted electrons as discussed in Sec. 4.1.3) but the fraction of secondary electrons to photoemitted electrons is very small.

The transverse emittance of the beam has been measured as a function of the emission phase and the result is plotted in Fig. 4.20. The measurements have been performed with the single slit located 1.6 m downstream from the cathode and the YAG screen located 1.01 m further downstream from the slit. In the figure, the mean momentum of the beam is also shown in order to show the emission phase dependence. The minimum of the transverse emittance can be achieved at an emission phase around the reference phase (i.e., the emission phase providing a highest momentum gain) for the operating conditions described above. For these emittance measurements the energy of the drive-laser pulse has been adjusted to get 1 nC beam for each emission phases because the beam charge has a strong contribution on the emittance.

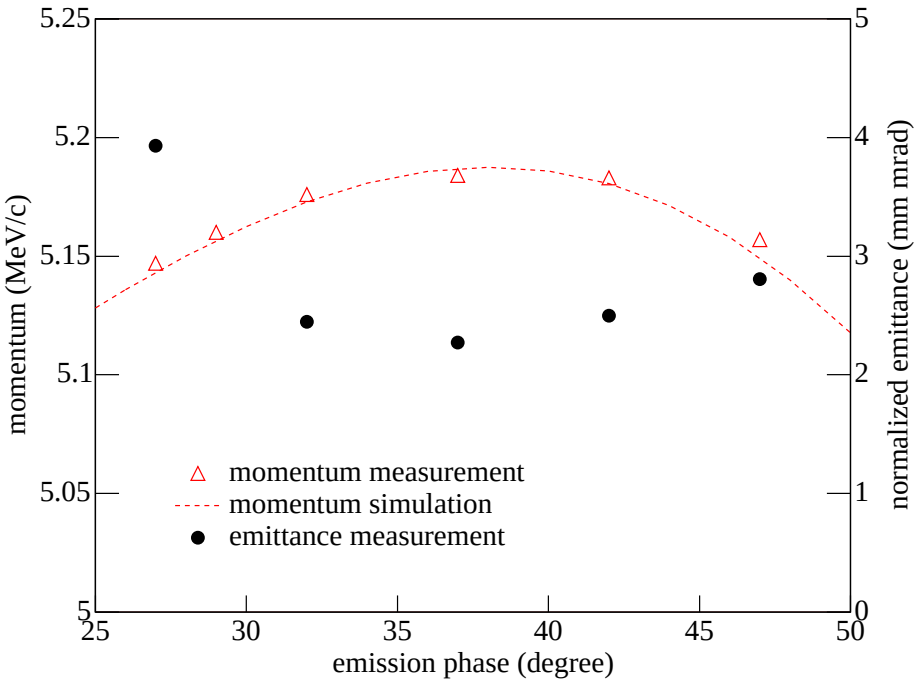

Figure 4.20: Mean momentum and transverse emittance vs. emission phase for cathode #500.1. To get a minimum transverse emittance at 45 MV/m of maximum rf field at the cathode, the emission phase has to be set to about 37°.

4.2.2 Effective electron emission for high charge beams

Even if the laser pulse energy is kept constant, the bunch charge extracted from the cathode varies with the rf field strength. Figure 4.21 shows the bunch charge measured as a function of the gun gradient with two different energies of the laser pulse. The beam charge has been measured with the Faraday cup 0.78 m downstream from the cathode. For the measurements, a laser pulse with a radial transverse profile of about 0.47 mm rms and a flat-top longitudinal profile of about 21 ps FWHM were used. The emission phase was optimized to extract the maximum charge at each measurement point. In order to guide the extracted charge to the Faraday cup, the solenoid current was also optimized for each measurement point.

When electrons are emitted from the cathode, the electrons see the mirror image inside the material, with the same charge but an opposite polarity, at the same distance but the opposite direction from the cathode surface (see Fig. 4.2.2). The mirror charge pulls the electrons back to the cathode surface. In addition to the mirror charge force, the electron beam expands by itself after emission due to the space charge force. As a result, a fraction of the electrons emitted from the cathode may move backward to the cathode where they disappear or produce secondary electrons. Since the impact energy of the electrons hitting the cathode surface is high (typically on the order of 10 keV), the number of secondary electrons produced during

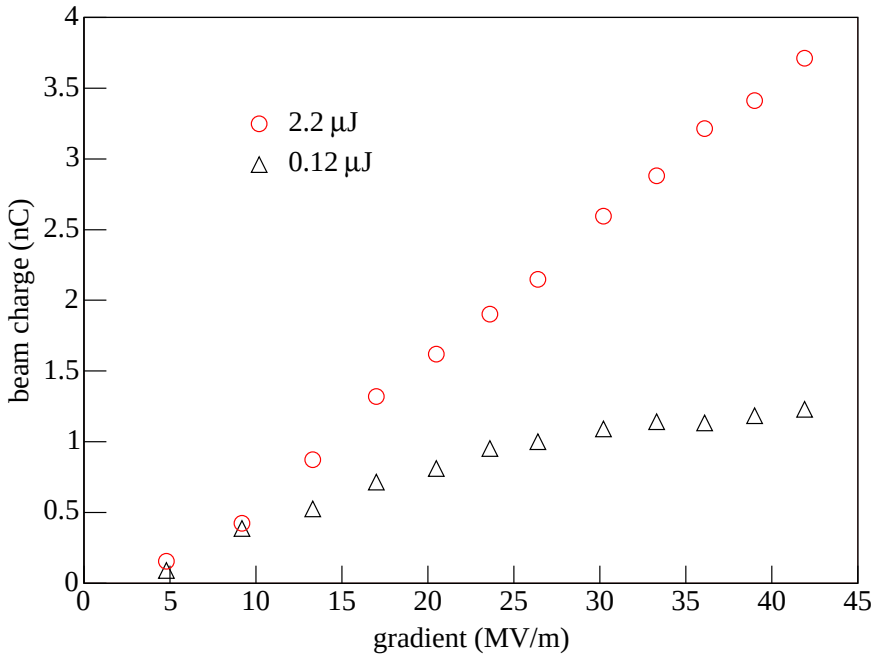

Figure 4.21: Bunch charge vs. rf gradient in the gun; two different energies of the drive-laser pulse were used for cathode #500.1.

the emission is very small (typically less than 1‰ of the photoemitted electrons). Figure 4.2.2 illustrates the forces affecting the electron bunch during emission: The force generated by the rf accelerating field, the space charge force and the mirror charge force.

4.2.3 Effective emission at the optimum phase

The electron beam emitted from the cathode does not have exactly the same profile as the drive-laser pulse. The space charge force as well as the mirror image force have a strong effect on the beam profile (see Fig. 4.23). Since the length of the laser pulse ranges about 10° in the rf phase, the Schottky effect and/or the space charge force introduce an inclination on the temporal profile within one bunch as well [68].

For a typical operating condition of PITZ (1 nC and about 46 MV/m of rf gradient), the optimum phase is about 37° (see Fig. 4.20). According to the bunch charge curve in Fig. 4.19, the electron bunch emitted at 37° feels the influence of the three forces. This means that the emission process for the head and the tail part of one bunch might be dominated by different forces. Therefore, a more fine adjustment for the laser profile has to be made for real operating conditions.

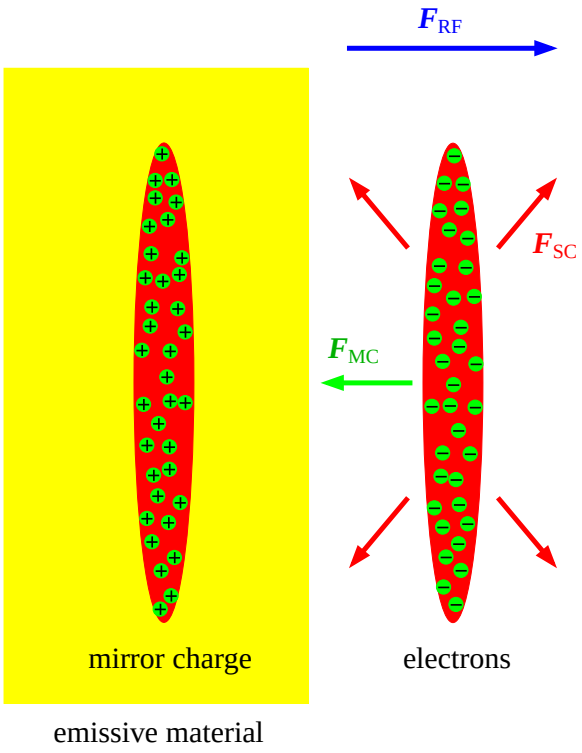

Figure 4.22: Illustration of the forces affecting the beam near the cathode: the force by the rf field F_{RF}, the space charge force F_{SC}, and the mirror charge force F_{MC}.

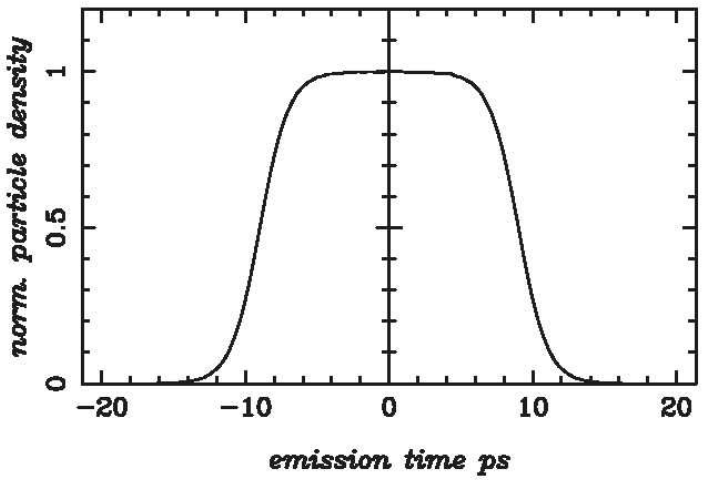

(a)

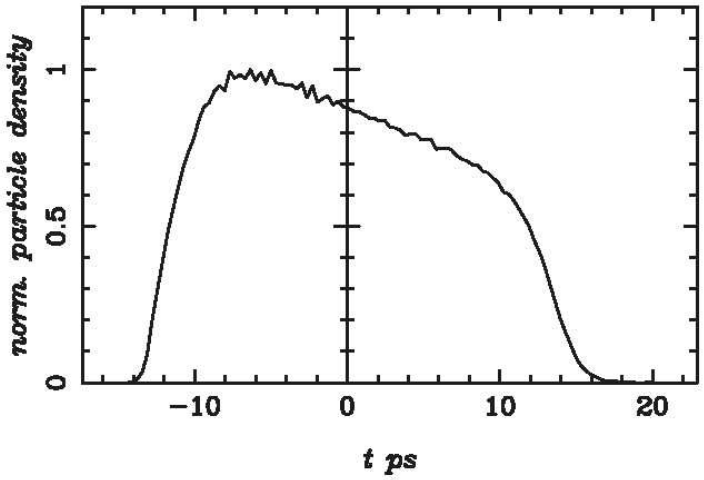

(b)

Figure 4.23: Temporal bunch profile after emission simulated with ASTRA (b) and the laser pulse profile (a). The bunch profile has been numerically calculated at 5 mm from the cathode.

Chapter 5

Dark current

In photocathode rf guns, dark current is defined as "unwanted electrons generated in the absence of the drive-laser pulse". Since the VUV FEL and the European XFEL demand high gradients and long rf pulses at the gun, the amount of dark current is comparable to the electron beam and can be a hazard to the downstream components like diagnostics, cryogenic modules and undulators. Most of the dark current is cut by beam pipes and collimators, but dark current starting close to the center of the cathode can be accelerated together with the electron beam. Therefore,

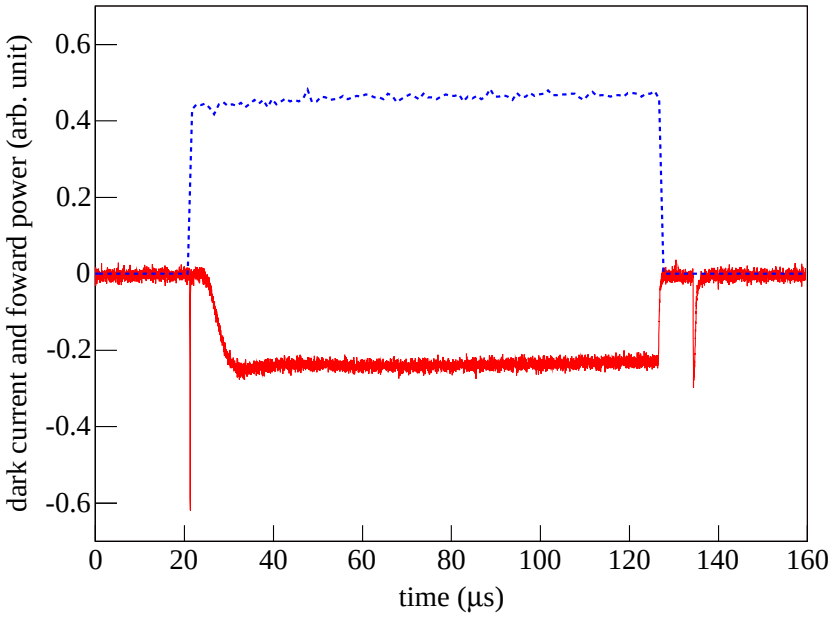

Figure 5.1: Typical dark current measured with the Faraday cup 0.78 m downstream from the cathode (full red line). The rf forward power into the gun (dotted blue line) is shown as well.

understanding the source locations as well as the dynamics of dark current is crucial to prevent vacuum components from radiational activation and damage.

An example of dark current generated by the high rf field is shown in Fig. 5.1. The main part of the dark current increases slowly with the start of the rf pulse and decreases quickly after the end of the rf pulse because the rf power in the cavity has a finite fill/decay time and the amount of the field emission follows the relation, $I_{\mathrm{emit}} \sim E^2 \exp(-1/E)$ (Eq. 3.7). Two sharp peaks are visible in the figure. The peaks come from multipacting at the cathode, which will be discussed in the next chapter.

In this chapter, the crucial sources of dark current are characterized and the behavior for several cathodes and two gun cavities at different conditioning situation are discussed.

5.1 Dark current source

5.1.1 Trajectories of the field-emitted electrons

The amount of the field emission increases with the local electric field according to the Fowler-Nordheim relation as discussed in Sec. 3.1. Therefore, the most sensitive regions for dark current can be estimated from the rf field calculation in the cavity. The three dimensional rf field in the gun cavity and a part of the coaxial rf input coupler has been calculated using the code MICROWAVE STUDIO [69] and the am-

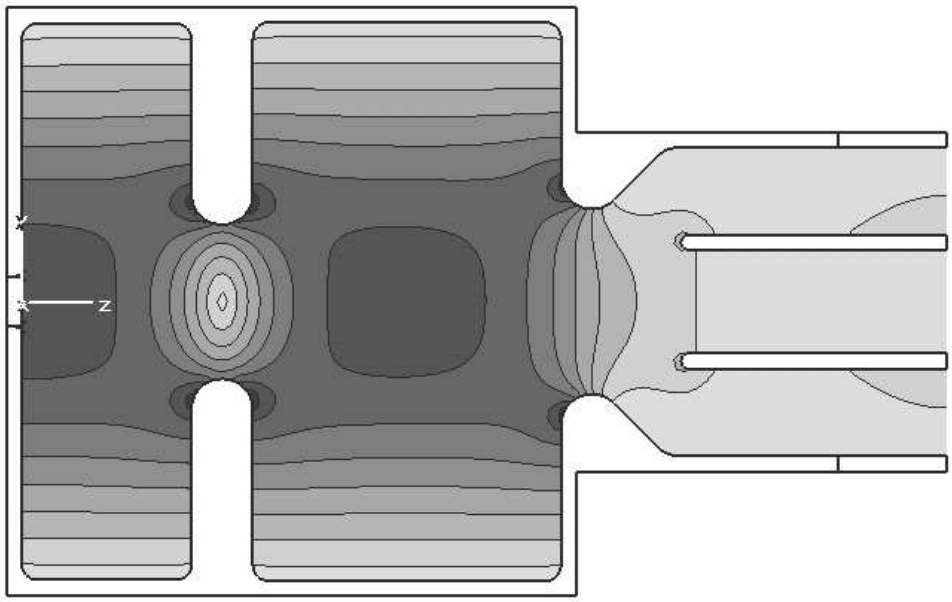

Figure 5.2: RF electric field calculation in the cavity.

plitude of the calculated field is shown in Fig. 5.2. From this simulation, a strong surface field is present at the irises and the cathode area.

The beam dynamics of the dark current from the high field strength region has been studied by means of ASTRA and is presented in Fig 5.3. The simulation shows that electrons starting at the cathode area (the Cs_2Te film, the Mo cathode plug, and the Cu backplate near the cathode) can be accelerated downstream and can be measured with the Faraday cup. The field emitted electrons from other sources, like the iris or the entrance to the coupler, cannot leave the gun cavity, because they cannot be captured by the accelerating rf electric field. However, they are able to locally heat up the cavity surface and may create secondary electrons. In order to suppress vacuum problems induced by field emission from the cavity surface, a careful conditioning is necessary [70].

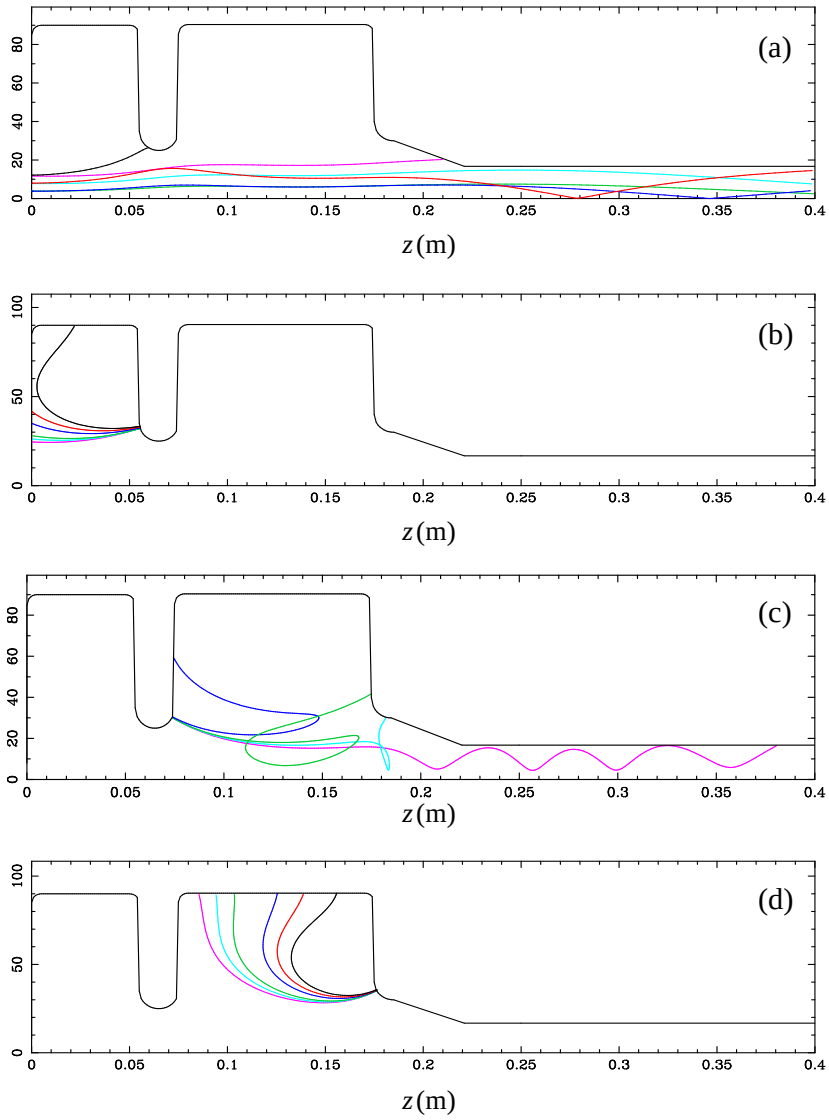

Figure 5.3: Example trajectories of the electrons emitted from the high field strength regions: (a) the cathode area, (b) the first iris in the half cell, (c) the first iris in the full cell, and (d) the second iris in the full cell. A gun gradient of 42 MV/m and a main solenoid current of 300 A have been used for the simulations. The electrons have been tracked up to 0.4 m downstream taking into account apertures of the gun cavity and the beam pipe.

5.1.2 Empirical approach of source characterization

In this section, the dark current image is compared to the cathode geometry in order to figure out the dark current source locations. A photography of the cathode front surface is shown in Fig. 5.4. The photography has been taken through the vacuum window in the cathode chamber. The cathode has been positioned using the manipulator in the load-lock chamber. The polished Mo cathode plug (8 mm radius) is coated with a thin Cs_2Te film (2.5 mm radius) at the center of the front surface (Fig. 5.4 a). The wire surrounding the cathode in Fig. 5.4 a is an anode installed for QE measurements of the cathode in the cathode chamber. With a UV lamp, the QE of the cathodes can be measured in the cathode chamber without influence of the rf as well as the aperture effects. On the Mo plug surface in Fig. 5.4 a, the reflected image of the vacuum window is visible. The Mo plug is polished and has a nearly optical surface quality. In order to make an electric contact in the gap between the Mo plug and the Cu cavity, a CuBe spring is used [13].

Dark current traces on the YAG screen 0.78 m downstream from the cathode have been investigated. Figure 5.5 a shows dark current for a main solenoid current of 360 A and a bucking solenoid of 70 A when a maximum rf field of 40 MV/m is applied at the cathode. This solenoid configuration makes the dark current image be clearer at the screen even though the magnetic field at the cathode is not zero (see Sec. 2.1.4). The steerer before the screen was switched off during the measurements to avoid that electrons with different energy bend by different amounts. A good

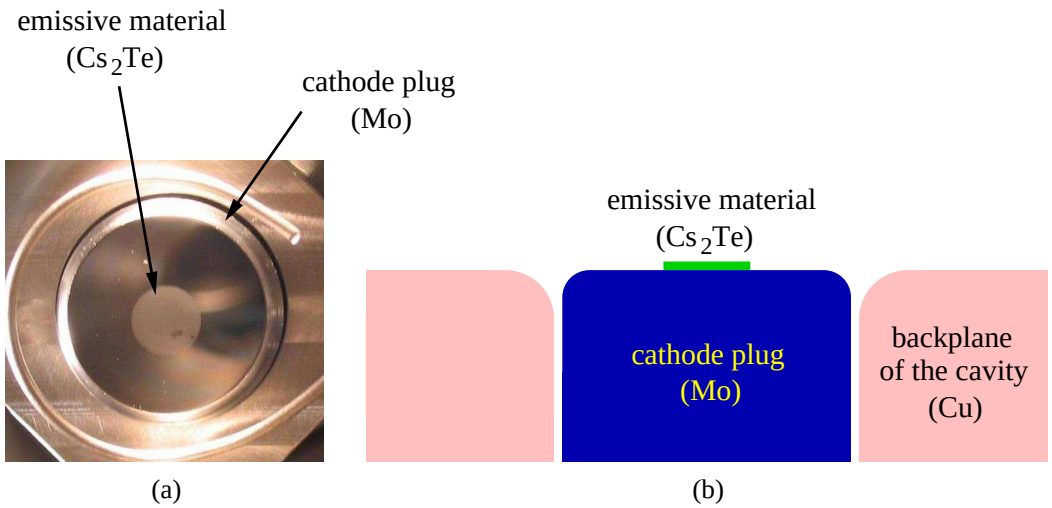

Figure 5.4: Geometry of a cathode. (a) The front surface of the cathode in the cathode chamber. Thin film of Cs_2Te is visible. The circular wire in front of the cathode plug is used to measure the QE and installed only in the cathode chamber. (b) A schematic cross section of the cathode and the backplane of the Cu cavity.

correspondence between the geometry of the cathode front surface (Fig. 5.4 a) and the dark current image (Fig. 5.5 a) can be found: the two ring-shape images might be corresponding to the boarder of the Cs_2Te film and the edge of the Mo cathode plug. The spiral pattern outside the three rings is thought to be from the edge of the hole in the Cu cavity backplane because the pattern is not changed at all with the rotation of the cathode plug. The dark crossing lines in Fig. 5.5 a are grids marked on the screen. The intervals between two lines are 1 cm. The elliptical bright line is the boarder of the YAG screen.

When the drive-laser with a transverse profile as shown in Fig. 5.5 b hits the electrical center of the cathode, the electron beam produces an image at the center of the dark current image as shown in Fig. 5.5 c. For this measurement, a drive-laser with a low energy (electron bunch charge $\sim$ 2 pC) and a spot size of 0.44 mm rms was used in order to make the brightness of the beam comparable to that of the dark current and also to make the beam image size optimal as will be shown below. The structure of the electron beam (Fig. 5.5 d) is similar to the transverse profile of the drive-laser (Fig. 5.5 b), which means that the low charge electron beam can be imaged onto the screen without loss of profile information.

Figure 5.6 compares the dark current images for three cathodes (one Mo and two Cs_2Te cathodes). The pattern of the images are the same for the three cathodes, but the intensity of the inner ring is different. The ring pattern might come from a focusing effect by the rf field and the solenoid field, and the Cs_2Te film seems to contribute for the higher intensity of the inner ring. The inner ring could be measured far downstream together with electron beams as well.

The emission location of the beam was scanned by moving the drive-laser spot on the cathode (see Fig. 5.7). The laser spot was moved vertically by 1 mm steps with the mirror located at the end of the telescope system between the laser source and the view port of the accelerator vacuum tube. In the figure, the beam movement takes place horizontally because the solenoid field rotates the electron beam by 90°. Due to the large QE difference between the Cs_2Te film ($\gtrsim$ 1%) and the Mo plug ($\lesssim$ 0.01%), the boundary between Cs_2Te and Mo can be estimated.

When the whole part of the laser hits the Cs_2Te area, a bright circular image of the electron beam is shown at the center of the dark current image. With moving the laser spot to the boarder of the Cs_2Te film, a part of the circular image is getting cut. When the laser spot location is moved out of the Cs_2Te area, the beam image completely disappears. The electron beam is cut by about a half of the size at $x =$ 0 mm and $y = -3$ mm and at $x = 0$ mm and $y = 2$ mm. The distance of the two points corresponds to the diameter of the Cs_2Te film (5 mm).

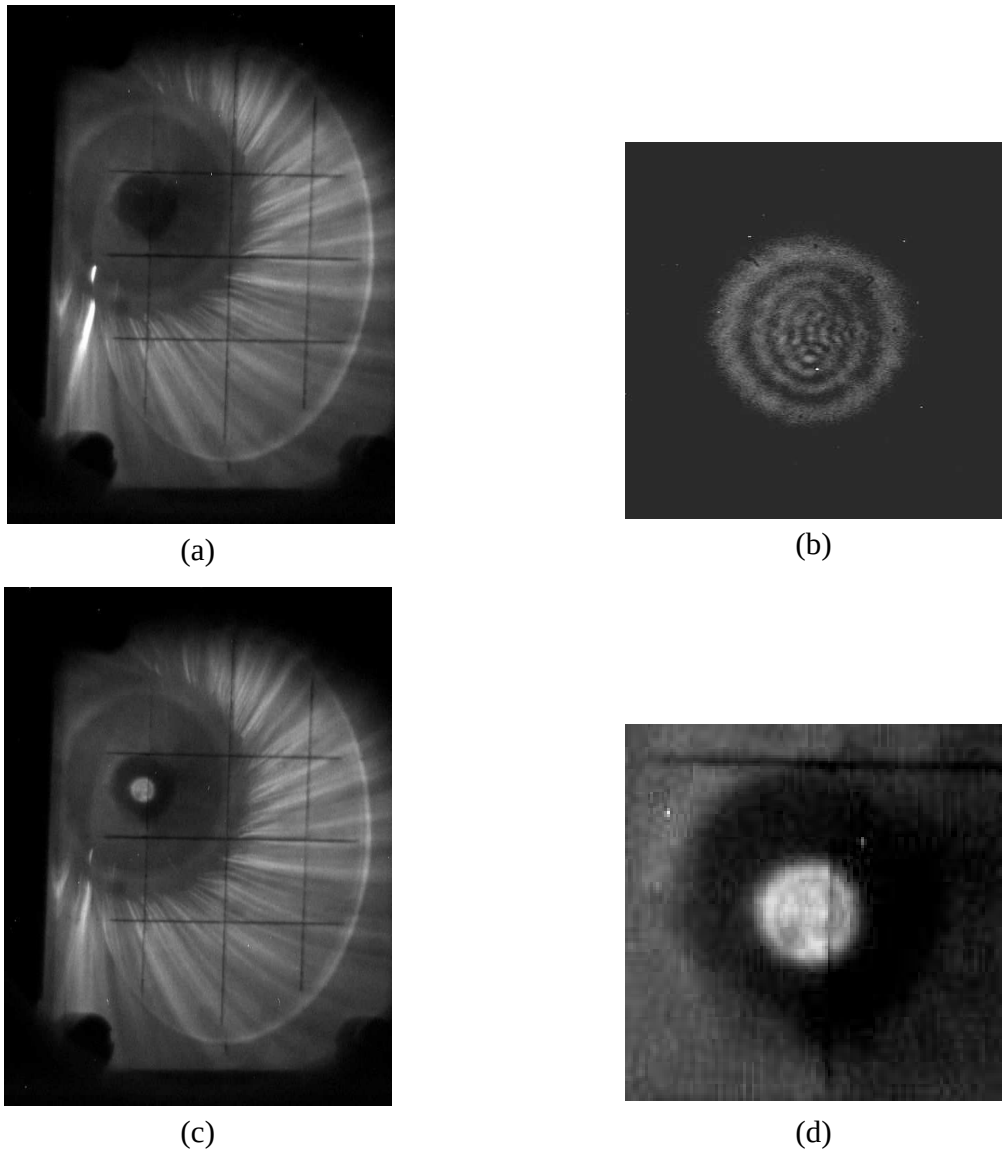

Figure 5.5: Images of a dark current, drive-laser, and electron beam. Cathode #33.2 was used for these measurements. A main solenoid current of 360 A and a bucking solenoid current of 70 A were used in order to focus the dark current and the beam when a maximum rf field of 40 MV/m is applied at the cathode. (a) Dark current image at the screen 0.78 m downstream from the cathode. (b) The transverse profile of the drive-laser at the virtual cathode (see Sec. 2.2.1 for the measurement procedure). Clear diffraction patterns are shown. (c) Dark current and electron beam. The drive-laser has been positioned at the electrical center of the cathode in order to produce the electron beam. (d) Enlarged view of the electron beam in (c). The charge distribution of electron beam shows a similarity to the diffraction structure of drive-laser profile.

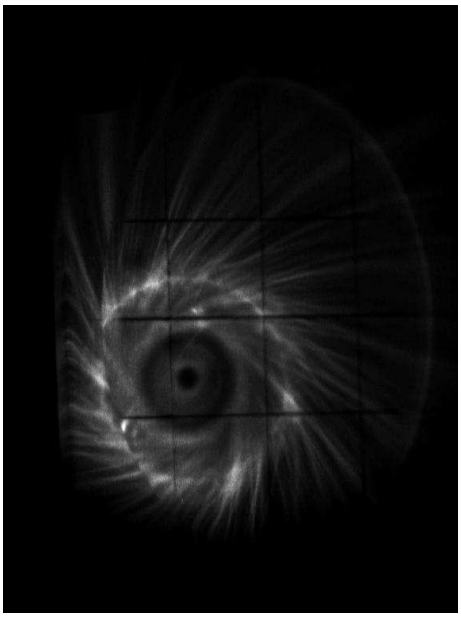

(a) cathode #56.2 (Mo)

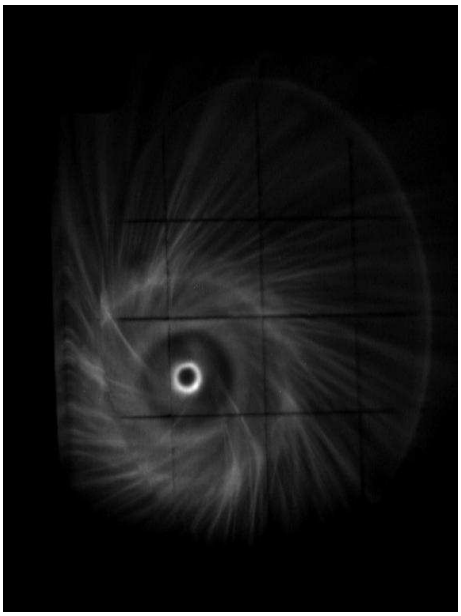

(b) cathode #54.2 (Cs_2Te)

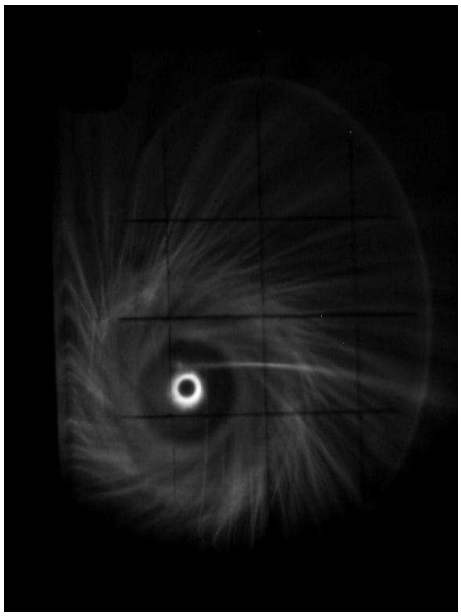

(c) cathode #58.1 (Cs_2Te)

Figure 5.6: Dark current images for one Mo cathode and two Cs_2Te cathodes for a main solenoid current of 320 A and a bucking solenoid current of 80 A when a maximum rf field of 42 MV/m is applied at the cathode. The dark currents were imaged on the screen 0.78 m downstream from the cathode. The images for all three cathodes were taken when the cathodes were used for the first time.

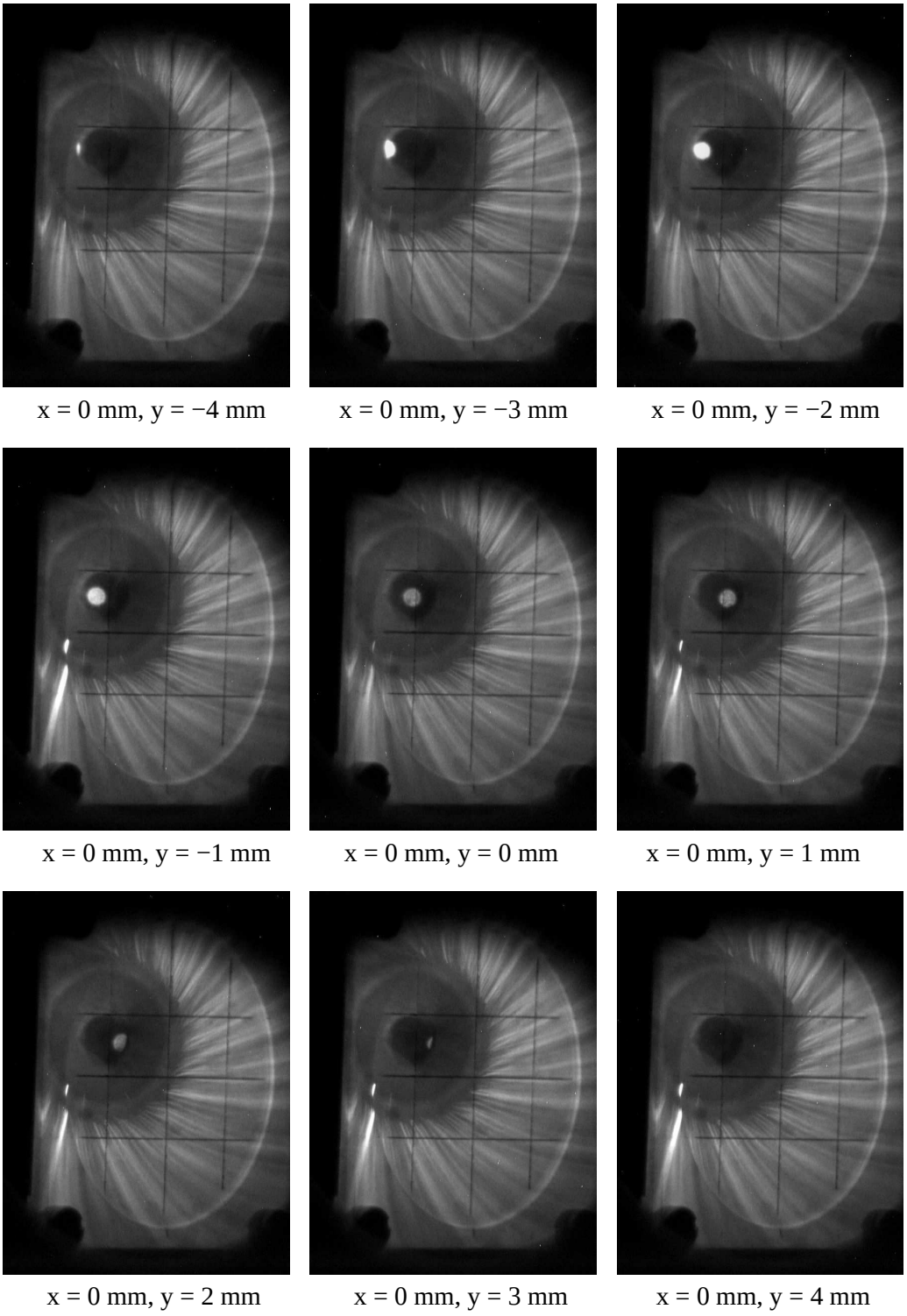

Figure 5.7: Electron beam movement inside the dark current image. The same cathode (#33.2) and the same machine conditions were used as in Fig. 5.5. The beam movement was driven by controlling the laser spot position on the cathode.

5.2 Momentum spectrum

Figure 5.8 displays momentum spectra of dark current and electron beam. The momentum spectra have been measured with the spectrometer dipole 3.45 m downstream from the cathode and the YAG screen in the dispersive arm section. In order to cover a wide range of momenta, the current of the dipole has been scanned and a series of the projected beam images have been collected in order to realize the actual momentum distribution. As discussed in Sec. 3.1, dark current, generated by the strong rf field, is field-emitted around 90° in the rf phase (see Fig. 3.2). The electron

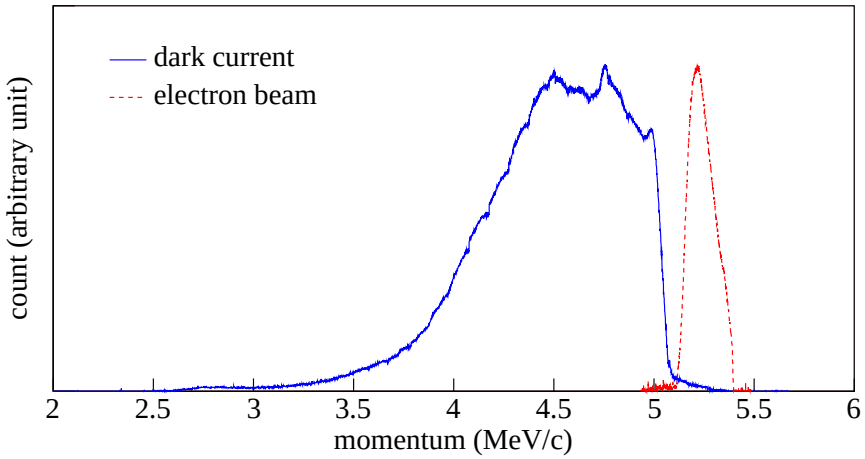

(a)

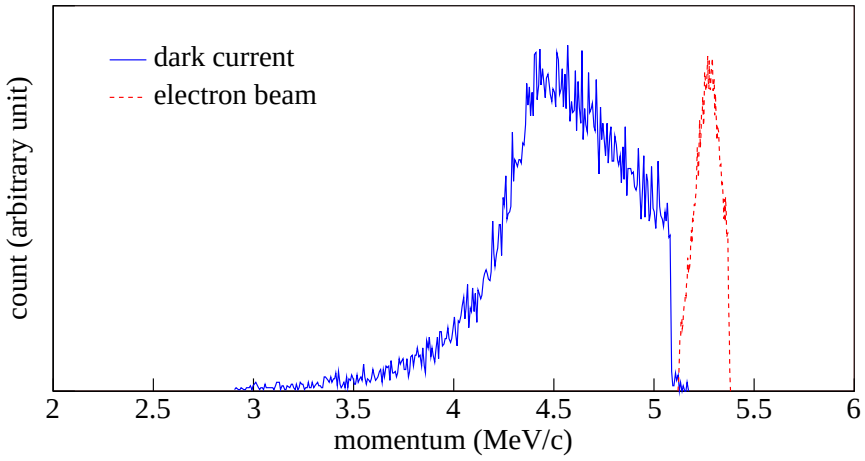

(b)

Figure 5.8: Momentum spectra of dark current and electron beam: (a) measurement with a spectrometer dipole and (b) simulation assuming 46.5 MV/m maximum field at the cathode. The vertical axes show relative intensities.

beams were produced at the emission phase (∼35°) providing the maximum mean momentum.

The initial distribution for the dark current simulation was configured by taking account of the discussion in Sec. 3.1 and 5.1. The dark current source was assumed to be the cathode itself and the surrounding area. The time structure of the field emission current was made to be a Gaussian distribution around 90° in the rf phase with a spread of 14° (∼30 ps) rms. In the simulations, dark current and electron beam have been tracked up to the dipole position considering apertures composed of the gun cavity, the coaxial rf input coupler, and the beam pipe. When an electron hits any aperture, the electron is lost in the tracking simulation.

For the momentum measurements, steerers had to be used to guide the electrons to the dipole and to the screen in the dispersive arm. For the simulations, the steerer effect has been ignored and, as the result, the actual aperture effect is underestimated in the simulation. Therefore, the intensity of the simulated dark current below about 4.8 MeV is higher than that of the measured one.

The high momentum part of the dark current is overlapping with the electron beam to a small extent. According to simulation results, the overlapping part consists of secondary electrons produced at the cathode as well as field-emitted electrons [71] (see Sec. 4.1). Because the major part of the field-emitted electrons cannot be accelerated downstream due to the emission phase, the electron can hit the cathode and generate secondary electrons. When the secondary electron is generated the rf phase is close to the zero phase, therefore secondary electrons can get a high momentum like electron beams.

5.3 Dependence on the solenoid field

In this section, the dark current dependence on the solenoid field for cathodes with different Cs_2Te film thicknesses is discussed. In the first half of the section, the dark current dependence on the main solenoid current is discussed keeping the bucking solenoid current to be zero. In the second half, the dark current dependence on combinations of the main and the bucking solenoid currents is discussed.

Dependence on the main solenoid

Figure 5.9 shows the measured dark current for Mo cathode #47.3 as a function of the main solenoid current together with an ASTRA simulation. The bucking solenoid current was kept to be zero. In the simulation, the same source location and time structure of the field emission current was used as in Sec. 5.2.

The amount of dark current reaching the Faraday cup depends on the strength of the magnetic field of the main solenoid. The irises in the gun, the coaxial coupler, the beam tube, and the mirror reflecting the laser pulse onto the photocathode play a role as apertures for the dark current beam. A force induced by the main solenoid field and the rf field guides the dark current through these apertures.

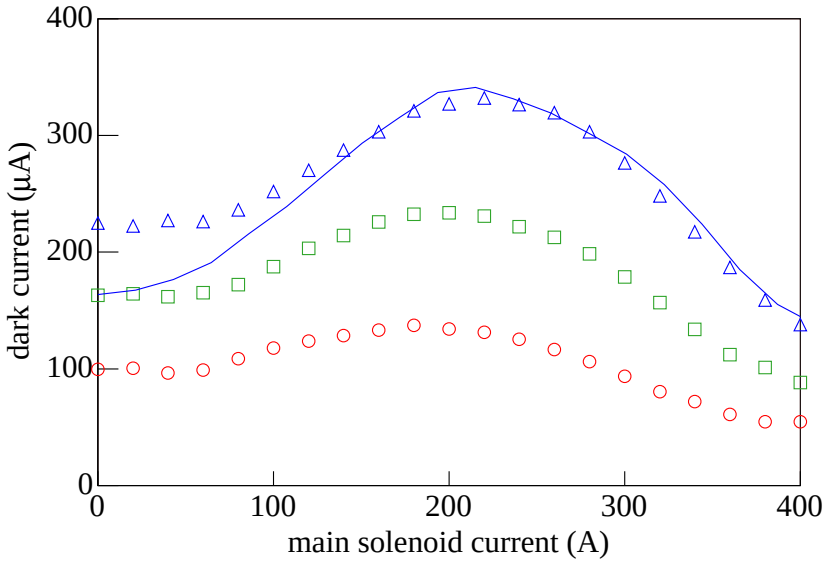

Figure 5.9: Dark current measurements with cathode #47.3 (Mo) vs. main solenoid current at several maximum rf fields: at 42 MV/m (△), 40 MV/m (□), and 37 MV/m (○). A simulation (line) is compared with the measurement for the 42 MV/m case.

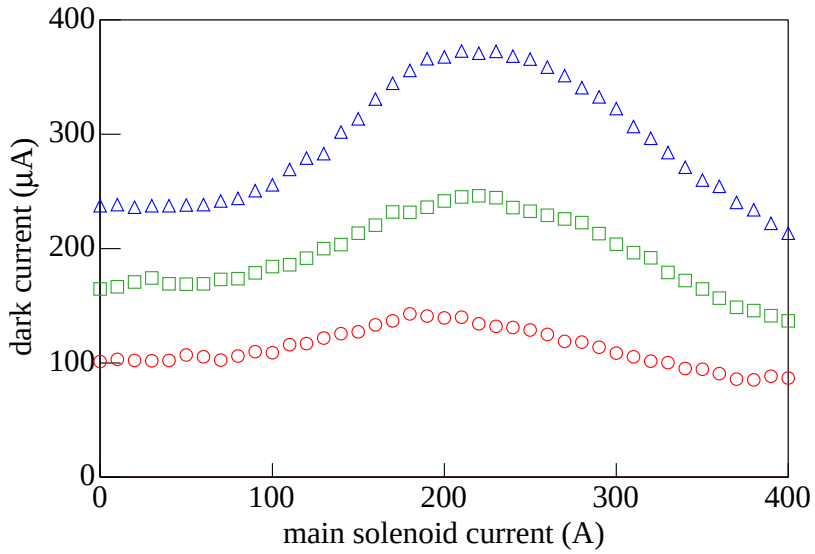

Figure 5.10: Dark current measurements with cathode #61.1 (20 nm Cs_2Te thickness) vs. main solenoid current at several maximum rf fields: at 42 MV/m (△), 40 MV/m (□), and 37 MV/m (○).

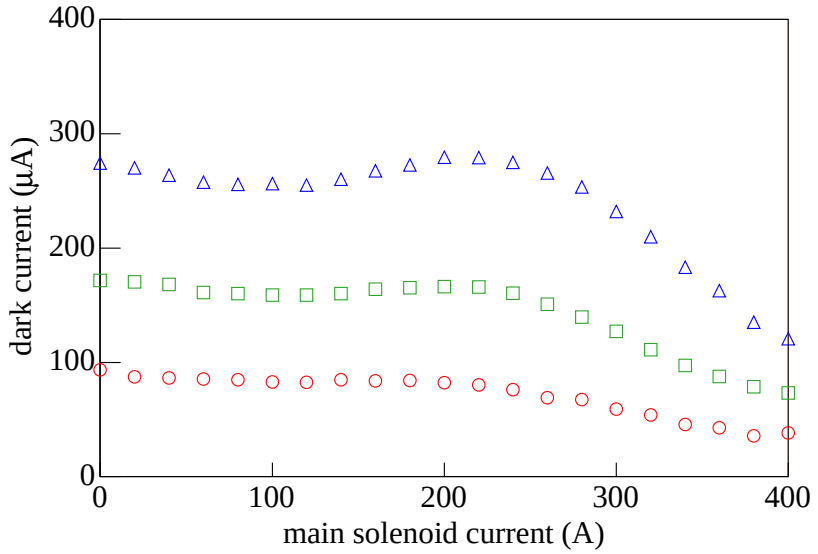

Figure 5.11: Dark current measurements with cathode #35.2 (40 nm Cs_2Te thickness) vs. main solenoid current at several maximum rf fields: at 42 MV/m (△), 40 MV/m (□), and 37 MV/m (○).

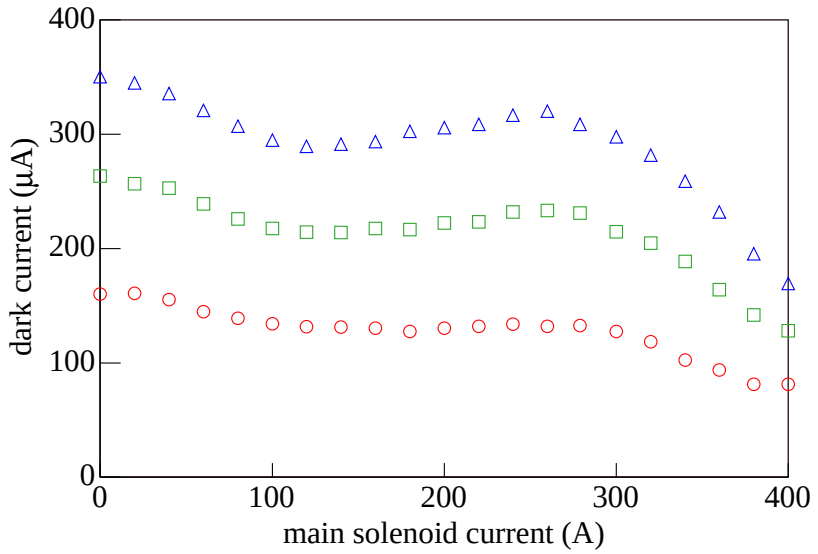

Figure 5.12: Dark current measurements with cathode #500.1 (60 nm Cs_2Te thickness) vs. main solenoid current at several maximum rf fields: at 42 MV/m (△), 40 MV/m (□), and 37 MV/m (○).

The dark current dependence on the main solenoid current is shown in Figs. 5.9 – 5.12 for the cathodes with a different thickness of the Cs_2Te film, a distinct difference was found at the low main solenoid current region. For the cathode with a thicker Cs_2Te film, a higher dark current is observed at small solenoid field. The cathodes #61.1, #35.2 and #500.1 have a Cs_2Te film with a thickness of 20 nm, 40 nm and 60 nm, respectively (see Appendix A for a more detailed cathode information). The dark current dependence on the main solenoid current for the Mo cathodes showed a similar behavior as for cathode #61.1, but the behavior was closer to what can be expected from the simulation. The different behavior for the cathodes with different Cs_2Te film thickness is not expected from beam dynamics simulations, which means that the difference originates from a different emission process for the different thickness cathodes. Field emission from the Cs_2Te cathode under the influence of a magnetic field must be studied in detail.

Dependence on the main and the bucking solenoids

For the thinnest cathode, #61.1, the dark current at zero main solenoid current is about 200 μA and does not depend on the bucking solenoid current (Fig 5.13 a). For the thickest cathode, #500.1, on the contrary, the dark current strongly varies with the bucking solenoid current (Fig 5.13 b). A hill of the dark current appears following a line satisfying the relation: $I_{\text{bucking}} \sim 0.25 \cdot I_{\text{main}}$. The inclination of the hill line is higher than for the compensation condition of the magnetic field at the cathode: $I_{\text{bucking}} = 0.0764 \cdot I_{\text{main}}$ [18]. This hill cannot be explained with a beam dynamics simulation and might be related to an emission process itself.

In Fig. 5.14, the dark current measurements with two Faraday cups at different distance from the cathode are shown. Cathode #60.1 with a Cs_2Te film thickness of 30 nm shows a bucking solenoid dependence with a strength in between the dependence of cathode #61.1 (20 nm) and #500.1 (60 nm) (Fig. 5.14 a). For the Faraday cup located 5.7 m downstream from the cathode, a focusing effect becomes dominant and the major part of the dark current gets lost except near 200 A of the main solenoid current. Above a main solenoid current of 270 A, no dark current was measured at the second Faraday cup. For the dark current measurement at the second Faraday cup, an electron beam emitted at the optimum emission phase (about 35°) was sent to the Faraday cup by help of steerers. The steerers had to be optimized to send the beam without the loss of beam charge because the accelerator beamline was mis-aligned with an error of several mm. Therefore, the dark current loss was due to an over-focusing of electrons and due to misalignment of the beamline.

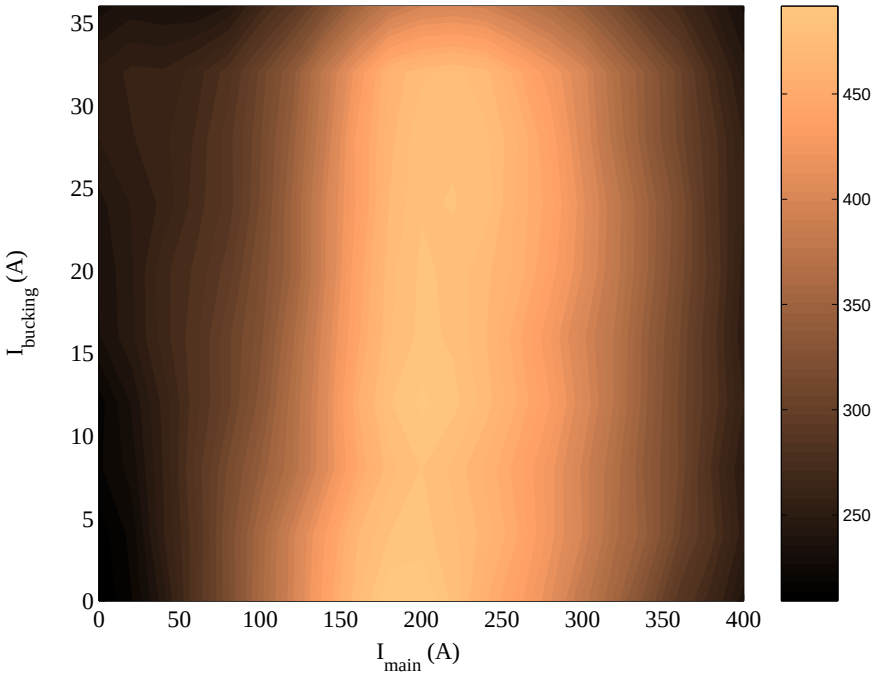

(a)

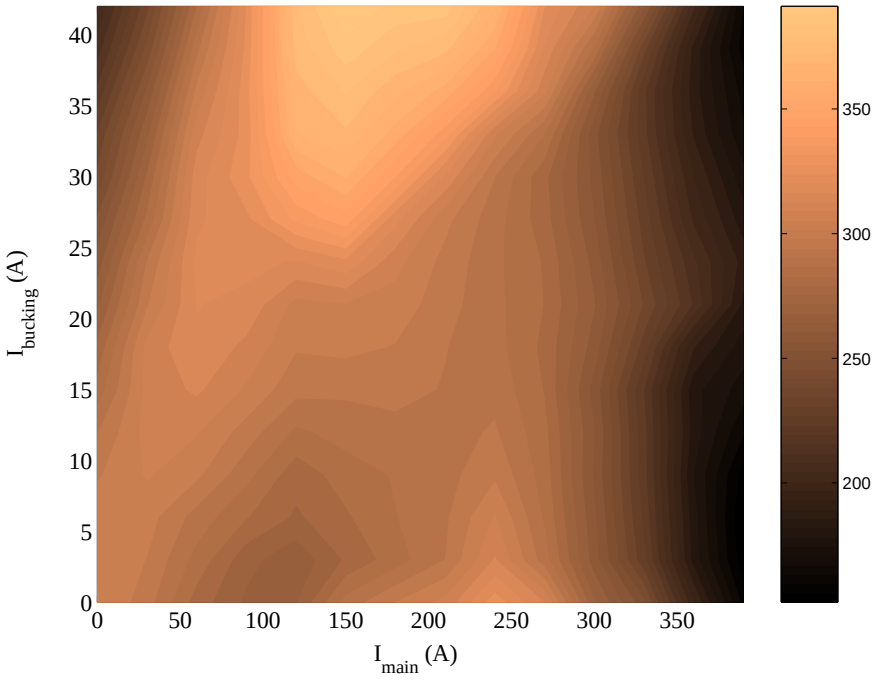

(b)

Figure 5.13: Measured dark current vs. main and bucking solenoid current; (a) #61.1 (20 nm Cs_2Te thickness), (b) #500.1 (60 nm Cs_2Te thickness). The scales in the right bars are in μA.

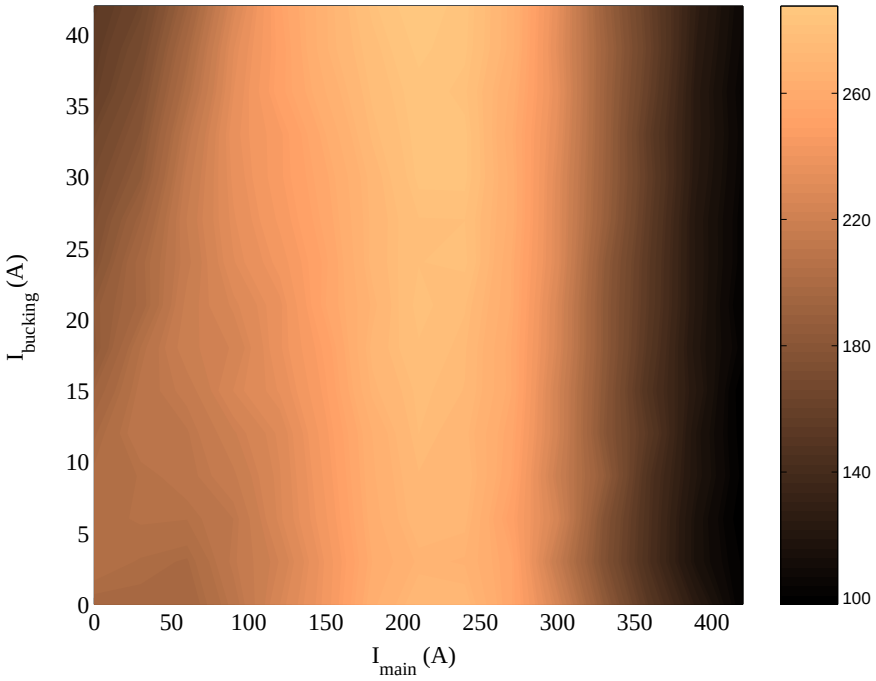

(a)

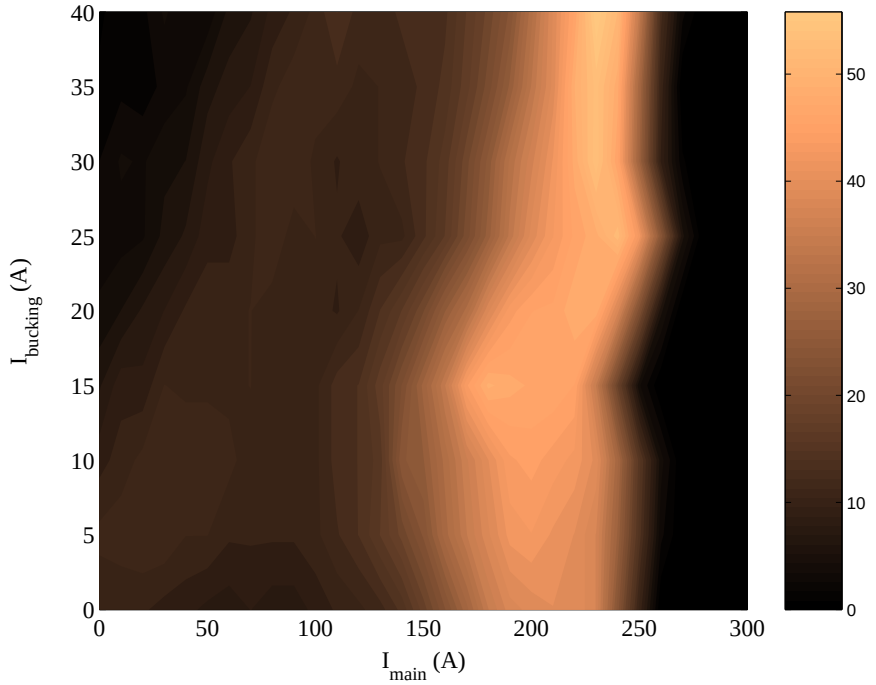

(b)

Figure 5.14: Measured dark current vs. main and bucking solenoid current for #60.1 (30 nm Cs_2Te thickness). The measurements have been made with the Faraday cups at different locations: (a) at 0.8 m and (b) at 5.7 m. The scales in the right bars are represented by μA.

5.4 Dependence on the states of cathodes and cavities

Figure 5.15 shows Fowler-Nordheim plots (Eq. 3.8) for different gun cavities and conditioning states. Until November 2003, the first PITZ gun cavity named prototype #2 was used. This gun cavity showed a low dark current after a long conditioning time. At present, this gun cavity is used as the injector of the VUV FEL in Hamburg. When we started to use the second PITZ gun cavity named prototype #1 in January 2004, a large amount of dark current was measured since the inner surface quality of the gun cavity was much worse that that of gun cavity #2 [70]. After several months of operation including conditioning efforts, the cavity showed a dark current level even less than the previous cavity (see Fig. 5.17).

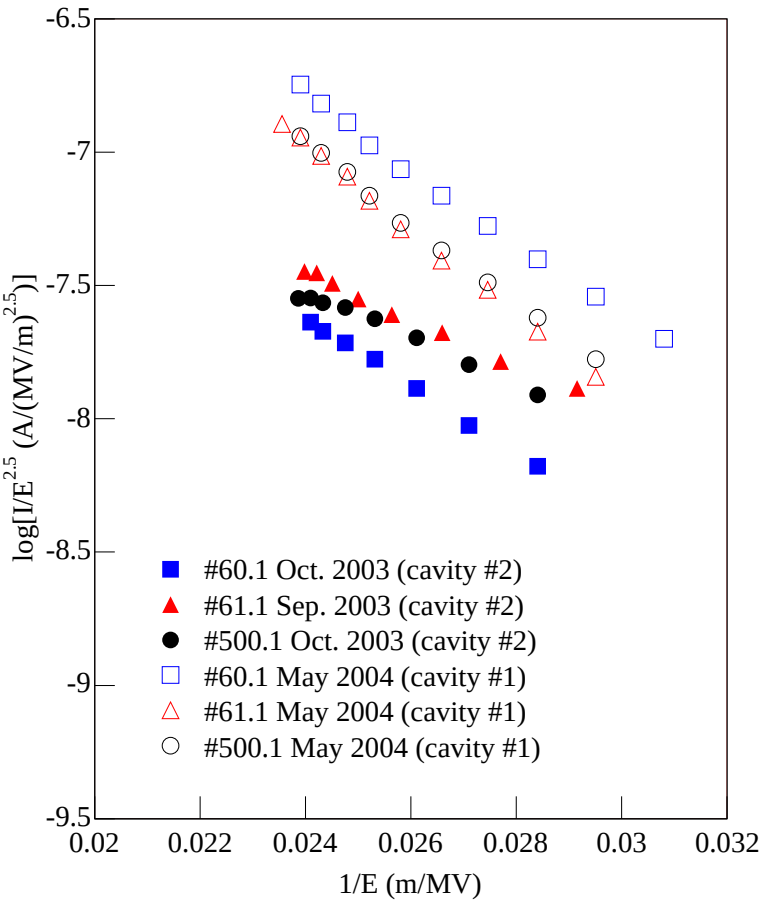

Figure 5.15: Fowler-Nordheim plots showing a cavity dependence. Cavity prototype #2 was used till November 2003 at PITZ. Cavity prototype #1 has been installed in January 2004 and is in operation. During the exchange of the gun cavities the photocathodes were kept in the ultra-high vacuum in the separated cathode chamber.

The field enhancement factor $\beta_{\rm field}$ and the effective areas $A_{\rm e}$ were found from the data in Fig. 5.15 using Eq. 3.7 and 3.8. The results are summarized in Table 5.1. When we compare the measurements between two cavities at different conditioning status in the autumn of 2003 (well conditioned cavity #2) and in the spring of 2004 (not well conditioned cavity #1), the field enhancement factors became slightly smaller but the effective areas became larger by several orders of magnitude. The result might imply that the number of hot spots, which are strong sources for field emission, were reduced by rf conditioning.

Table 5.1: Field enhancement factor $\beta_{\rm field}$ and effective area $A_{\rm e}$ derived from the dark current measurements in Fig 5.15.

cavity	cathode	measured time	$\beta_{\rm field}$	$A_{\rm e}$ (m^2)
#2	#60.1	October 2003	214	1.25×10^{-15}
#2	#61.1	September 2003	273	2.34×10^{-16}
#2	#500.1	October 2003	327	7.45×10^{-17}
#1	#60.1	May 2004	184	4.16×10^{-14}
#1	#61.1	May 2004	166	7.95×10^{-14}
#1	#500.1	May 2004	177	4.64×10^{-14}

Figure 5.16 shows dark current measurements in cavity #2 for five cathodes. Two cathodes, #34.3 and #500, show a large dark current immediately after the first insertion into the cavity compared to the measurements after several months of operation. In case of #60.1 such an effect is not visible because the first measurement in April 2003 was made only after 3 weeks of operation. For cathode #34.3, both the field enhancement factor and the effective area decreased slightly. For cathode #500.1, the main origin of the dark current reduction was a decrease of the effective area.

Table 5.2: Field enhancement factor $\beta_{\rm field}$ and effective area $A_{\rm e}$ for the dark current measurements in Fig 5.16.

cathode	measured time	$\beta_{\rm field}$	$A_{\rm e}$ (m^2)
#34.3 (Mo)	January 2003	203	3.83×10^{-15}
#34.3 (Mo)	April 2003	179	2.61×10^{-15}
#60.1	April 2003	185	4.96×10^{-15}
#60.1	October 2003	214	1.25×10^{-15}
#47.3 (Mo)	September 2003	217	6.67×10^{-15}
#61.1	September 2003	273	2.34×10^{-16}
#500.1	September 2003	321	1.03×10^{-16}
#500.1	October 2003	327	7.45×10^{-17}

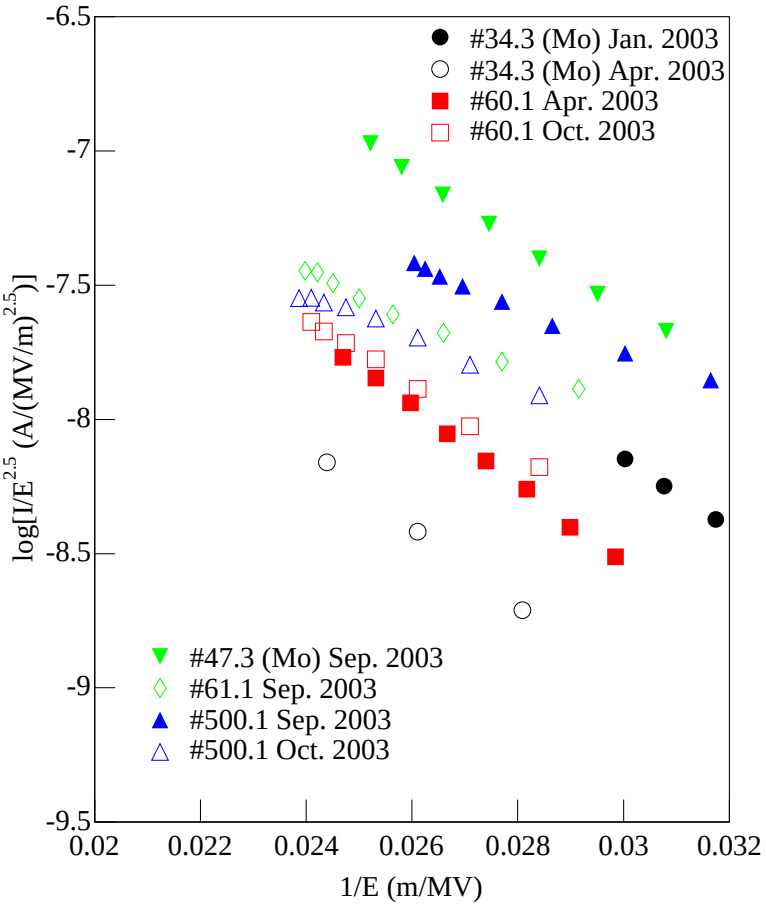

Figure 5.16: Fowler-Nordheim plots for different status of the cathodes in cavity #2.

Since the inner surface of cavity #1 was not very clean when it was installed, the conditioning was not straightforward but time consuming [70]. After a long time conditioning work, the dark current became even lower than for cavity #2 (Fig. 5.17). This cavity has been used for a high rf power test and higher gradient has been applied in the cavity.

According to the measurements shown above, the amount of the dark current does not relate to the Cs_2Te thickness. The amount of the dark current depends on the conditioning status of the gun cavity and the cathode and also on the cathode individual, possibly related to the preparation procedure.

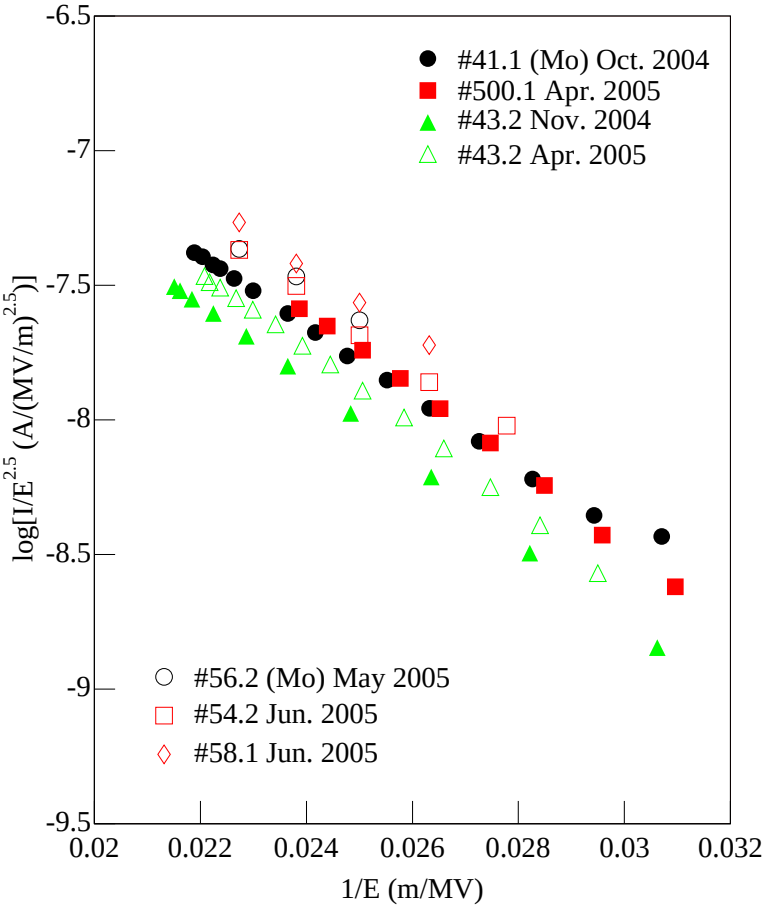

Figure 5.17: Fowler-Nordheim plots for different Cs_2Te cathodes in cavity #1 after a long-time conditioning.

Table 5.3: Field enhancement factor β_{field} and effective area A_e for the dark current measurements in Fig 5.17.

cathode	measured time	β_{field}	A_e (m^2)
#41.1 (Mo)	October 2004	203	1.36×10^{-15}
#500.1	April 2005	179	5.10×10^{-15}
#43.2	November 2004	185	2.78×10^{-15}
#43.2	April 2005	214	3.65×10^{-15}
#56.2 (Mo)	May 2005	217	1.51×10^{-16}
#54.2	June 2005	273	2.20×10^{-15}
#58.1	June 2005	303	2.99×10^{-15}

5.5 Dark current history

A long-term collection of the dark current measurements at the PITZ gun is shown in Fig. 5.18. Immediately after the installation of gun prototype #1 at PITZ (Spring 2004), a dark current of higher than 1 mA was observed for several cathodes. With time going on, the amount of dark current decreased for all cathodes. At the PITZ operation, the main reason of requiring new Cs_2Te cathodes were damages of the Cs_2Te film. The damages were clearly visible (see Appendix A.2). It might come from bombardments of ions to the cathode surface. Because the surface quality of gun cavity prototype #1 was not of the best one and a leak of the cooling water existed, the vacuum in the gun cavity was not always good as below 10^{-10} mbar.

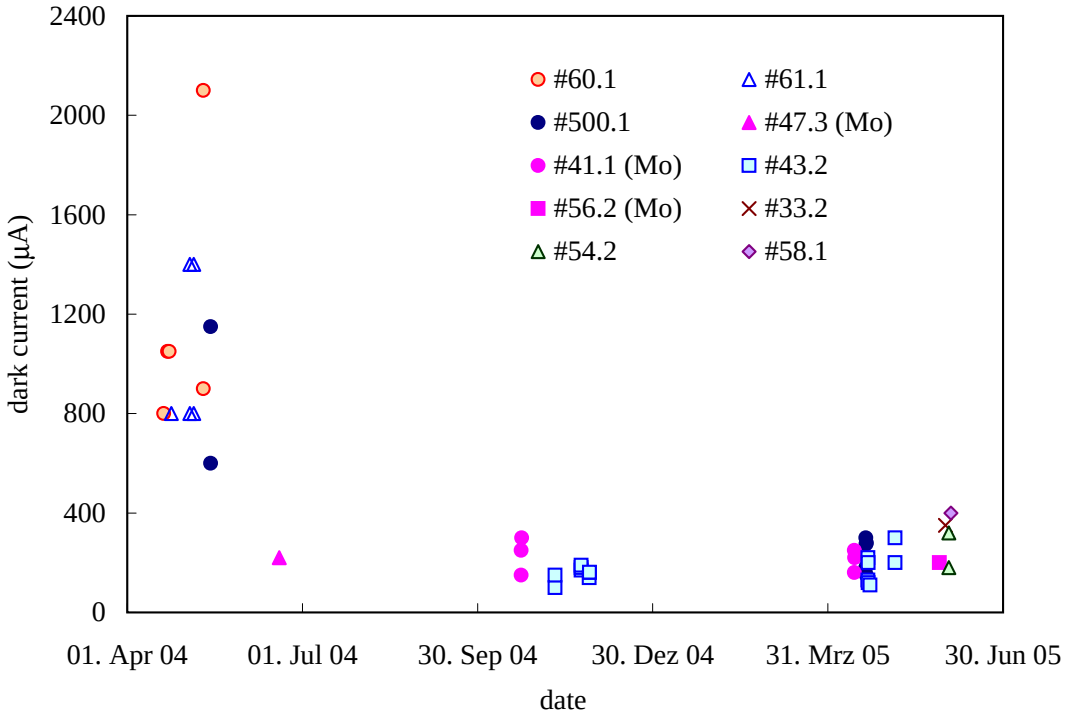

Figure 5.18: Dark current measurements in the PITZ gun prototype #1. The parameters were following: 40 MV/m gun gradient, 280 A main solenoid current, and 20 A bucking solenoid current. The data have been collected from the PITZ logbook by L. Monaco.

Chapter 6

Multipacting

Multipacting (multiple impacting) is an undesired explosive increase of the number of electrons. Multipacting can be initiated by a field emission due to the rf-induced surface field at the cathode, the coaxial coupler, or the gun cavity surface. Multipacting may cause rf power loss, lead to vacuum breakdown, and even damage the surface inside the cavity. Under the electromagnetic fields given by the rf and the solenoids, the number of electrons can be multiplied by a process of secondary electron generation when electrons impact a material with a secondary emission yield (SEY) larger than one. One speaks of multipacting if the process is repeated and the number of electrons increases. The multipacting process depends on the impact energy and the rf phase.

Single-side multipacting at a metal cavity surface occurs under alternating electromagnetic fields if an electron hits the departing point at the same rf phase after next rf cycles as when it started and if the secondary electron emission yield of the material is greater than one [73, 74, 75, 76]. Multipacting from metal surfaces can be suppressed by reducing the SEY with a careful conditioning process.

The following multipacting sources can exist in the photocathode rf guns.

a) RF coupler: At the surface of the coaxial coupler, a strong rf field is applied, and, moreover, the coupler is under an influence of the main solenoid. Therefore, the rf coupler can be a position for multipacting. In this case, multipacting will be strongly dependent on the main solenoid field but must be independent of the bucking solenoid field because the rf coupler is far from the cathode or the bucking solenoid. Sometimes, this multipacting has been detected at PITZ as well as TTF2. This multipacting shows up as "dead zone" between ~20 A and ~50 A of the main solenoid current independently of the rf gradient. When it happened, we could not operate the gun due to vacuum breakdown. After conditioning work, this multipacting has vanished.

b) Cavity surface made from copper: Multipacting will occur with a combination of the solenoid field and the rf field. If multipacting takes place at the cavity surface, the multipacting should not depend on the cathode material, i.e. whether Cs_2Te or Mo.

c) RF window: The bucking solenoid is located far from the rf window of the gun coupler. Therefore, the bucking solenoid current should not influence to multipacting occurring at the rf window.
d) Photocathode: Multipacting occurring at the photocathode will be dependent on the main solenoid field as well as strongly dependent on bucking solenoid field. The multipacting will be sensitive to the rf field at the cathode as well. But, first of all, cathode material will be most crucial for multipacting at the cathode.

In principle, other sources of multipacting except at the Cs_2Te photocathode can be inhibited by blowing up the chemically contaminated layers of the material, which may have a secondary emission yield higher than one, or by rounding out volcano-like structures which may allow a high field enhancement.

In this study, a new type of single-side multipacting is introduced. The multipacting takes place at a single-side, i.e. at the front surface of the Cs_2Te photocathode, but with possibly different phase between the emission phase of the primary and the secondary electrons. Unfortunately, the single-side multipacting occurring at the photocathode, cannot be suppressed because a high QE is unavoidably related to a high SEY.

6.1 Measurements

6.1.1 General description of observations of multipacting

Depending on the operating condition, either two sharp strong peaks at the beginning and the end of the rf pulses or one of them are present (see Fig. 5.1 and Fig. 6.1). The peaks do not show up for Mo cathodes and their behavior is sensitive to the solenoid configuration. Similar behaviors have been reported at other rf guns [72, 77]. The front multipacting peak appears immediately after the start of the rf pulse and the rear peak has a delay of the order of some μs after the end of the rf pulse. This observation implies that the multipacting happens when the gradient in the cavity is lower than its maximum value. Assuming that the multipacting occurs at the same gradient in the cavity for a certain cathode and a certain solenoid profile, the multipacting condition can be found with the following relation for the front peak

$$E_{\mathrm{MP}} = E_{\mathrm{max}} \left[1 - \exp(-t_{\mathrm{front}}/\tau)\right] \tag{6.1}$$

and also for the rear peak

$$E_{\mathrm{MP}} = E_{\mathrm{max}} \exp(-t_{\mathrm{rear}}/\tau), \tag{6.2}$$

where E_{MP} is the rf field at the center of the cathode when the multipacting occurs, E_{max} is the maximum field of the rf pulse, t_{front} is the delay between the start of the rf pulse and the beginning of the front multipacting peak, t_{rear} is the delay between the end of the rf pulse and the beginning of the rear multipacting peak, and τ is the fill/decay time of the rf field in the cavity. Only the rear peak is discussed in detail because the time difference between the start of the rf pulse and the first multipacting peak is much less than 1 μs and hard to be measured.

In the actual rf system, the rf field in the cavity is not zero but at a certain, very small level when the klystron is running but no low level input is fed into the klystron. Including the background rf term, Eq. 6.2 can be rewritten as

$$E_{\mathrm{MP}} = (E_{\mathrm{max}} - E_{\mathrm{BG}}) \exp(-t_{\mathrm{rear}}/\tau) + E_{\mathrm{BG}}, \tag{6.3}$$

where E_{BG} is the rf background when the low level rf input is not applied. From Eq. 6.3, the delay time can be expressed as a function of E_{max},

$$t_{\mathrm{rear}} = \tau \ln(E_{\mathrm{max}} - E_{\mathrm{BG}}) - \tau \ln(E_{\mathrm{MP}} - E_{\mathrm{BG}}). \tag{6.4}$$

The digital signal processing system and the preamplifier of the klystron are adjusted in order to minimize the background level [62]. The actual background power level is on the order of 100 W and negligible compared to the normal operating condition (> 3 MW) when discussing the photoelectron beam dynamics. For the multipacting process, however it can not be neglected.

6.1.2 Dependence on the maximum rf field

The multipacting behavior dependence on the maximum rf field is shown in Fig. 6.1. For these measurements, cathode #43.2 was used (when it was new) and the solenoid currents were 400 A in the main solenoid and 30 A in the bucking solenoid. At 40 MV/m of the maximum rf field (Fig. 6.1 a), the rear multipacting peak appears after the strong main dark current which corresponds to the pulse length of the rf forward power into the gun. As the maximum rf field decreases the level of the main dark current gets lower. On the contrary, the height of the multipacting peak does not change visibly (Fig. 6.1 b). As the maximum rf field decreases further, the front multipacting peak newly appears (Fig. 6.1 c). From those observations, one can

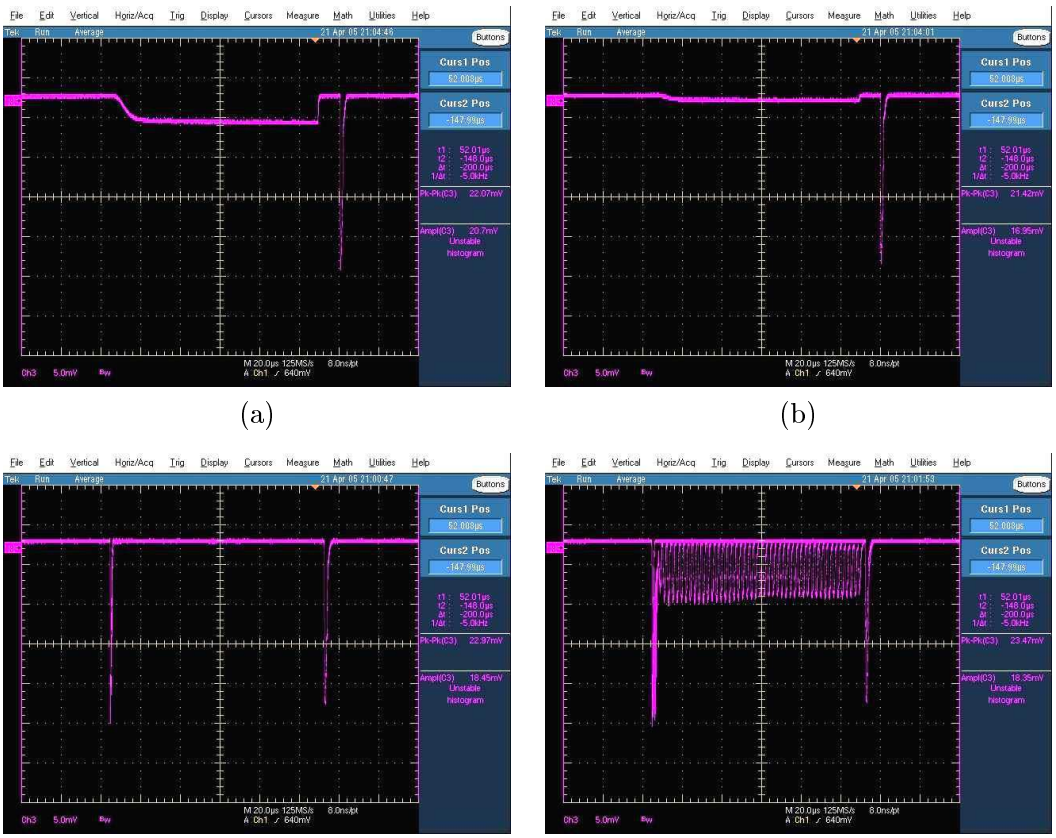

Figure 6.1: Signals measured with the Faraday cup 0.78 m downstream for gradients of (a) 40 MV/m, (b) 33 MV/m, (c) 2.7 MV/m, and (d) 2.4 MV/m. The signals were transported through a 50 Ω rf cable to the oscilloscope in the control room. The distance of grids are 5 mV in the vertical scale and 20 μs in the horizontal scale, respectively. Cathode #43.2 was used for this measurement when it was fresh. The solenoid currents were 400 A in the main solenoid and 30 A in the bucking solenoid.

conclude the following: The peak gradient does not affect the multipacting process of the rear multipacting peak. For the front multipacting peak, the multiplication of the number of electrons could occur due to the slower increase of the rf field. The rf field range required for the multipacting keeps up long enough to generate the multipacting.

If the maximum rf field decreases to a certain threshold, the multipacting takes place over the entire region of the rf pulse with an oscillatory feature (Fig. 6.1 d). Below the threshold, the beam loading induced by the multipacting disturbs the increase of the rf field strength in the gun cavity, i.e. the field strength provided by the rf power cannot be fully achieved in the gun cavity.

The position and the amplitude of the rear multipacting peak were observed

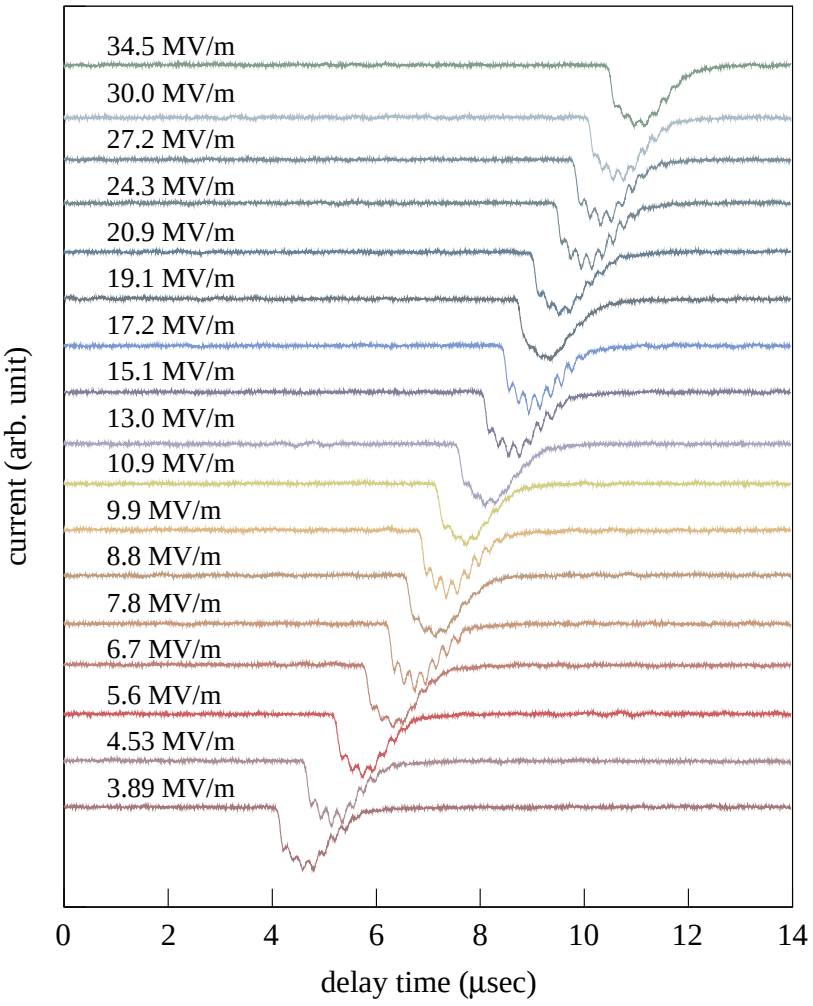

Figure 6.2: Rear multipacting peak with respect to the end of the rf pulse as a function of the maximum rf field at the cathode.

as a function of the maximum rf field in the cavity as shown in Fig. 6.2. The measurements have been made with the Faraday cup 0.78 m downstream from the cathode. The delay time decreases with lowering the maximum rf field but the charge in the multipacting peaks does not change. This result shows that the multipacting is independent of the maximum rf field and the multiplication process takes place at a low rf field during the decay of the rf field.

Three series of measurements for different states of two different cathodes have been performed and the results are shown with fits in Fig. 6.3. χ-square fits have been made to find the multipacting field E_{MP}, the rf background E_{BG}, and fill/decay time τ using Eq. 6.4, where E_{MP} and E_{BG} are completely unknown values and τ should be close to the measured one. The fit results are summarized in Table. 6.1. The two different cathodes show different multipacting fields E_{MP}. The possible reason for the difference will be discussed in the following sections. The fitted rf fill/decay times are in good agreement with the filling time of 2.78 μs obtained from the rf measurements of the cavity [78].

When the measurements were made, cathode #60.1 was strongly damaged but the central part of the cathode had still emissive material (Cs_2Te) (see Fig. A.3 a in Appendix A). Cathode #43.2 was fresh except for the small mechanical damage at the upper left corner which had not existed just after preparation (see Fig. A.1 a and Fig. A.1 b in Appendix A).

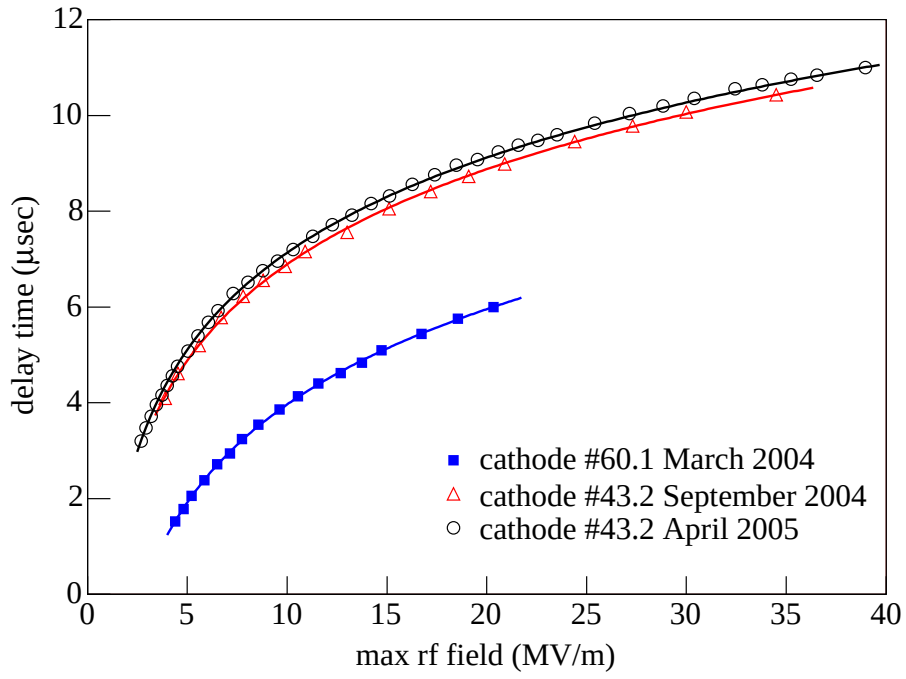

Figure 6.3: Delay time of the multipacting peaks as a function of the maximum rf field for two cathodes. The curves are fits according to Eq. 6.4.

Table 6.1: Fit results for the multipacting measurements in Fig. 6.3.

cathode	#60.1	#43.2	
measured time	Mar. 04	Sep. 04	Apr. 05
E_{MP} (MV/m)	2.70	1.04	1.07
E_{BG} (MV/m)	0.36	0.18	0.31
τ (μs)	2.80	2.83	2.83

6.1.3 Dependence on the solenoid setting

The longitudinal magnetic field along the z-axis is shown in Fig. 6.4 together with the rf field distribution and the gun aperture. The solenoid field distribution is displayed following the field measurement with a hall probe [18] (see Sec. 2.1.4 for more detail).

When the bucking solenoid switched off, the magnetic field at the front surface of the cathode is not zero. For example, when the main solenoid current is 400 A, the bucking solenoid current of 30.5 A is necessary to make the solenoid field zero at the cathode. Without the bucking solenoid current, the remnant field at the cathode is 0.012 T.

While the maximum rf field affects only the delay time of the multipacting peak, a change of the solenoid field distribution varies the shape and the charge of the

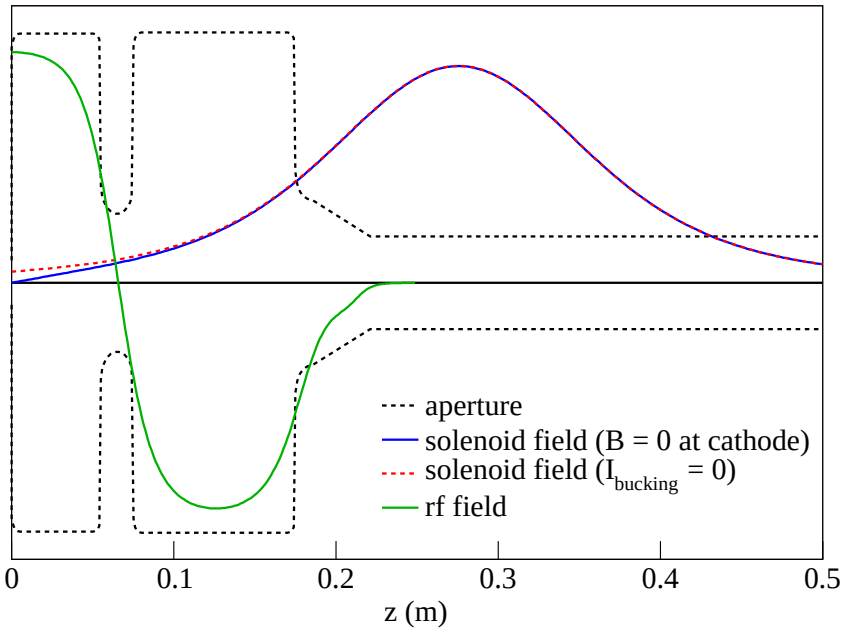

Figure 6.4: The solenoid field and the rf field with the gun aperture at PITZ.

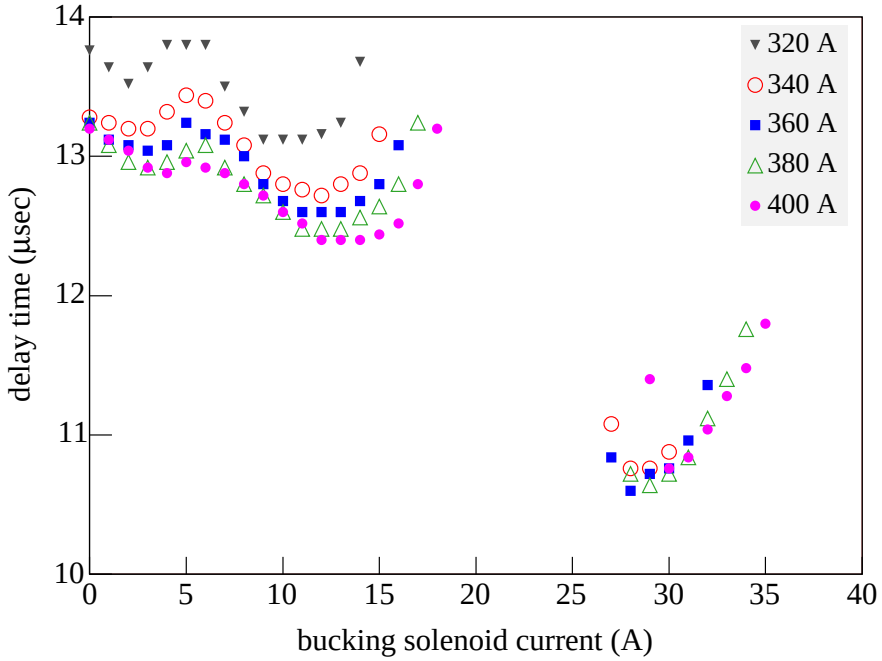

Figure 6.5: Measurements of the delay time between the end of the rf pulse and the start of the rear multipacting peaks as a function of bucking solenoid current for several main solenoid currents.

multipacting peak.

In order to see the dependence of the multipacting behavior on the solenoid field distribution, a set of measurements were made with cathode #43.2 in November 2004. The delay time for the rear peak was measured as a function of the bucking solenoid current for several main solenoid currents. At a bucking solenoid current of between 18 A and 26 A as well as higher than 35 A, no multipacting has been detected with the Faraday cup. With the increase of the main solenoid current up to 400 A, the delay time becomes shorter. The maximum rf field of 39 MV/m at the cathode was used. From the measurements in Fig. 6.5, the multipacting field E_{MP} has been calculated by using Eq. 6.3 with keeping the background field E_{BG} and the fill/decay time τ to be constant. The results (see Fig. 6.6) show that the multipacting takes place at gradients of less than 1 MV/m.

The charge contained in the multipacting peak is shown in Fig. 6.7. The maximum charge reaches above 1 nC. The plots of the multipacting field E_{MP} and the charge, as a function of the bucking solenoid current, show a similarity. According to the above measurement, the multipacting does not take place at the typical operation condition of PITZ (a main solenoid current of about 320 A and a bucking solenoid current of about 24 A at a rf gradient of 42 MV/m).

Figure 6.8 shows the variation of the peak shape with different bucking solenoid currents while keeping the main solenoid current to be 400 A. At a bucking solenoid

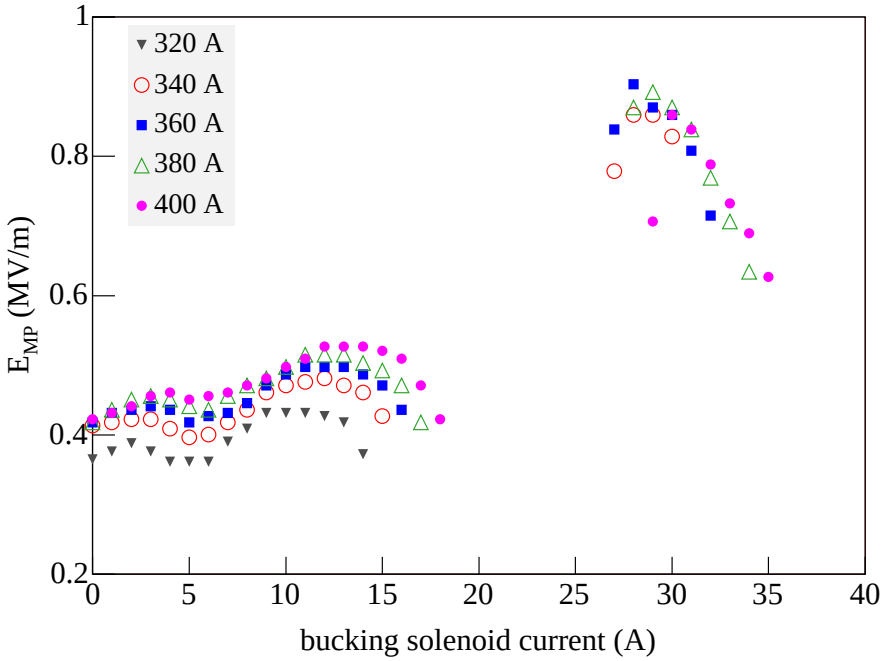

Figure 6.6: Calculated multipacting field E_{MP} for the measurements in Fig. 6.5.

current of 29 A, the peak is narrow. At zero bucking solenoid current, the peak is wide and the tail extends up to 30 μs after the end of the rf pulse which corresponds to the level of the background field. At 13 A, the peak shows an intermediate behavior between the cases of 0 A and 29 A and the peak charge is maximal.

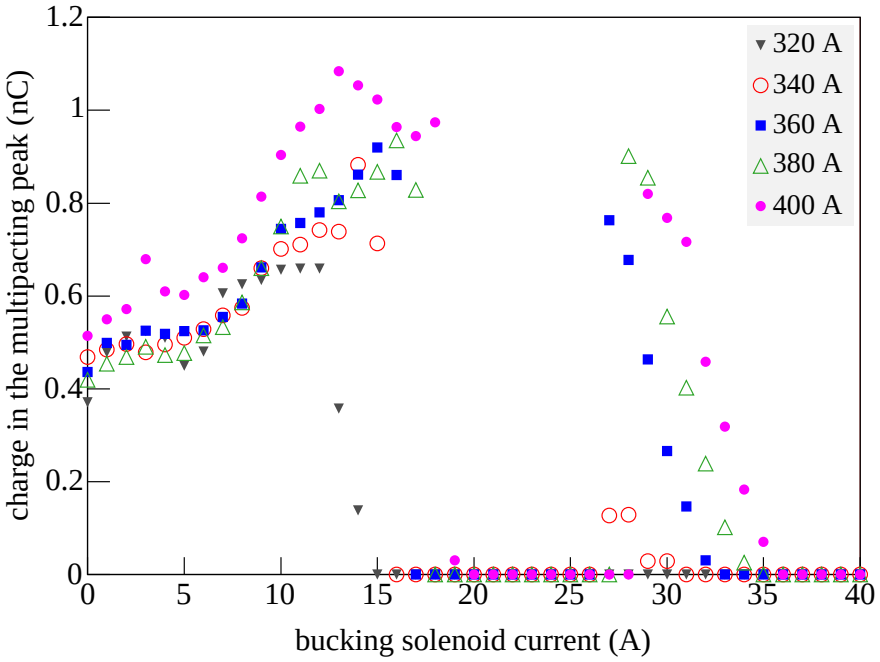

Figure 6.7: Charge measurements of the rear multipacting peak as a function of the bucking solenoid current for several main solenoid currents.

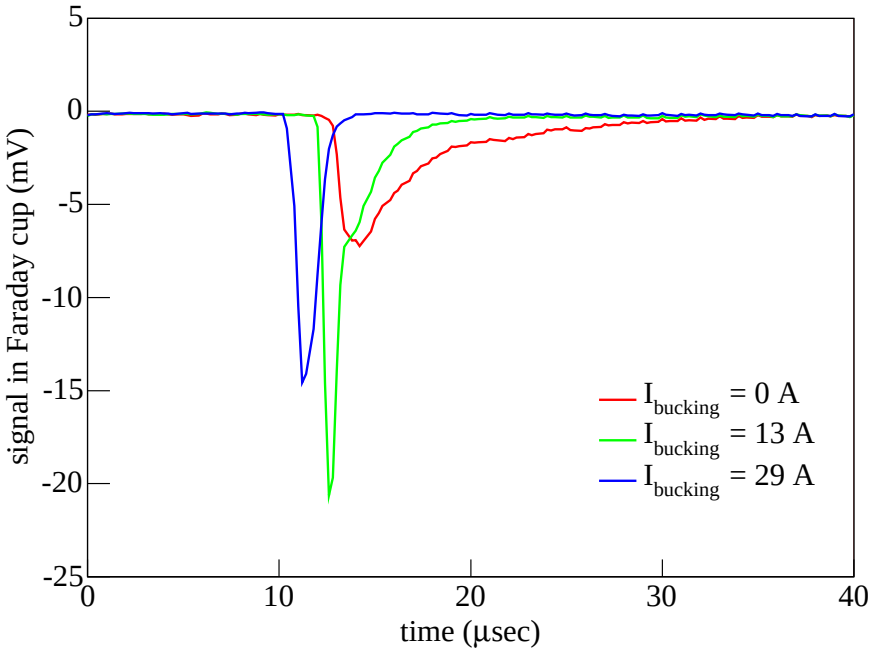

Figure 6.8: Temporal shape of the multipacting peaks.

6.2 Model of the mechanism

When a primary electron bombards the photocathode, it can generate secondary electrons because the Cs_2Te photocathode has a SEY larger than 1 (Sec. 3.3). The number of secondary electrons is described by Eq. 3.12.

The electron multipacting is illustrated in Fig. 6.9. In this simulation, a seed electron starts at an rf phase of 90° and at an rf field strength of 5.0 MV/m. A high rf field has been selected for a better visualization of the electron multiplication process. 400 A of the main solenoid current and 30.5 A of the bucking solenoid current have been selected.

When a seed electron, which is field-emitted from the cathode, starts at 0.04 mm from the electrical center of the cathode in the radial direction, the electron hits the cathode again and generates secondary electrons (1st generation). For a clear illustration, only one secondary electron is shown in the figure. The 1st generation electron moves for several rf cycles and hits the cathode again to produce the 2nd generation electrons. After several generations, the number of electrons can increase exponentially and the multipacting can take place. The multipacting takes place at the front surface of the cathode, therefore it is a single side multipacting.

Detailed processes to produce the multipacting at the cathode will be discussed

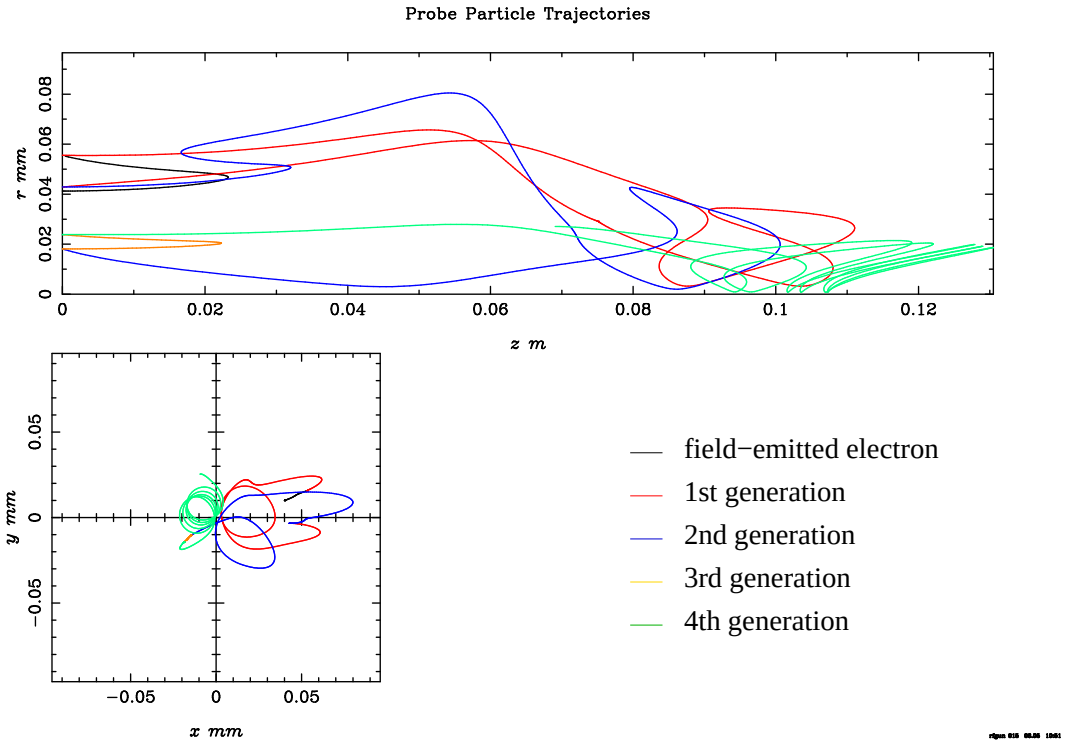

Figure 6.9: One example of electron trajectories for multipacting in the rf gun.

in the following sections. In these discussions, the multiplication is defined as the number of "active" electrons per seed electron after a specified number of rf cycles. Here, "active" means an electron which is not lost by hitting the inactive apertures (Mo or Cu) or dead after producing secondary electrons but an electron which is still able to produce the next generation of secondary electrons.

6.2.1 Electron dynamics at low rf field strength

The equation of the electron motion under the rf field in the rf cavity is described as

$$\frac{d\boldsymbol{p}}{dt} = e\,\boldsymbol{E}_0(\boldsymbol{r})\cos(\omega t) + \frac{e}{\omega}\,\boldsymbol{v}\times[\boldsymbol{\nabla}\times\boldsymbol{E}_0(\boldsymbol{r})]\sin(\omega t), \tag{6.5}$$

where $\boldsymbol{E}_0(\boldsymbol{r})$ is the amplitude vector of the rf field and $\boldsymbol{r}$ is the vector indicating the 3D coordinates of the electron. Due to the shape of the Cu cavity, an analytic approach is not available. In this study, numerical calculations with ASTRA have been made with a 3D rf field profile.

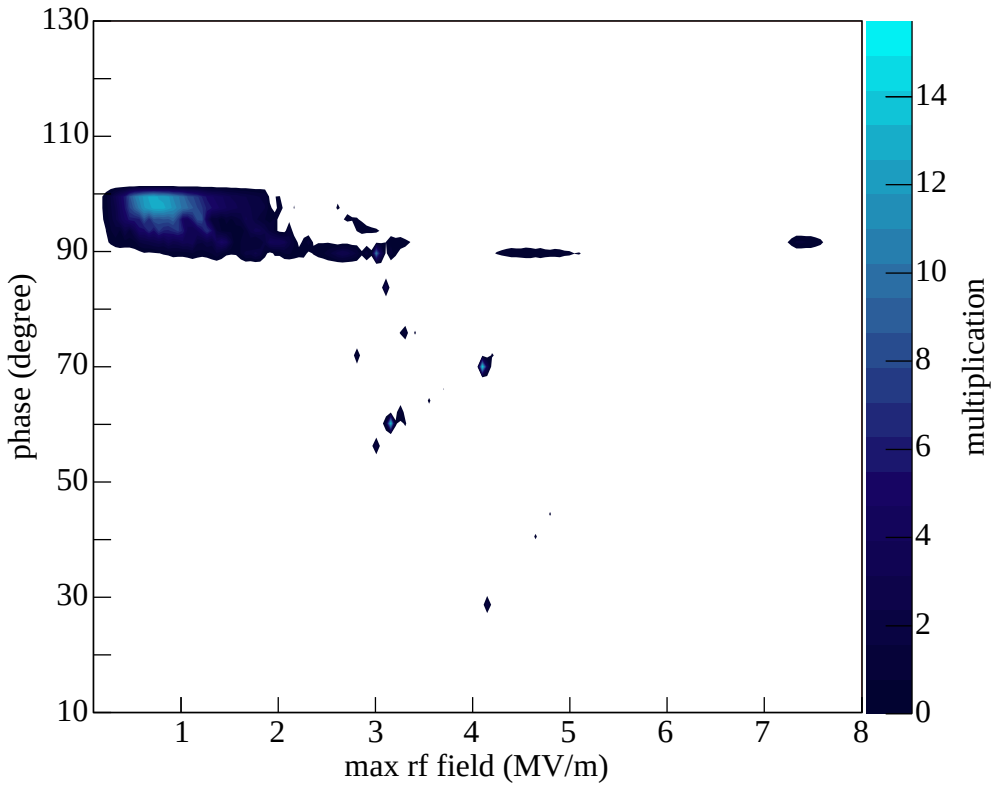

Figure 6.10: Electron multiplication as a function of the maximum rf field and the emission phase without solenoid field. Electron trajectories and secondary electron generation have been tracked for 100 rf cycles.

When the maximum rf field is smaller than about 10 MV/m, electrons starting at an emission phase of around 90° cannot flow out of the cavity due to their big phase slippage. Electrons emitted in this phase range either travel back to the cathode and can generate secondary electrons or they are trapped by the rf field to float back and forth inside the cavity. In the gun cavity, multipacting hardly occurs without solenoid field because the rf trap of electrons is not strong enough to generate the multipacting. Even though no multipacting has been observed without solenoid field, a possible multiplication has been numerically calculated (see Fig. 6.10).

In the Fig. 6.10, the multiplication of electrons in the rf cavity is significantly sensitive to the phase as well as to the amplitude of the gun rf field at the cathode when the electron emission happens. In this simulation, 500 seed electrons have been generated in order to reduce the error in the random generation of the number of the secondary electrons.

6.2.2 Electron dynamics at low rf field strength and solenoid field

With the solenoid field, the equation of motion is modified as

$$\begin{aligned}\frac{d\boldsymbol{p}}{dt} &= e\,\boldsymbol{E}_0(\boldsymbol{r})\cos(\omega t) + \frac{e}{\omega}\,\boldsymbol{v}\,\times[\boldsymbol{\nabla}\times\boldsymbol{E}_0(\boldsymbol{r})]\sin(\omega t)\\ &\quad + e\,\boldsymbol{v}\times\boldsymbol{B}_{\mathrm{sol}}(\boldsymbol{r}),\end{aligned} \tag{6.6}$$

where $\boldsymbol{B}_{\mathrm{sol}}(\boldsymbol{r})$ is the magnetic field generated by the solenoids, which is not homogeneous.

When the inhomogeneous solenoid field is applied, the electrons in the cavity experience a magnetic confinement. In order to follow the energy conservation law, the longitudinal component of the momentum which was acquired from the rf field, is converted into a transverse component in order to satisfy the relation:

$$e\,|\boldsymbol{v}\times\boldsymbol{B}_{\mathrm{sol}}(\boldsymbol{r})| = \frac{m\,|\boldsymbol{v}|^2}{|\boldsymbol{r}|}. \tag{6.7}$$

If the kinetic energy of the electron is low enough, the electron is not able to penetrate through the maximum magnetic field region and is reflected backward (to the cathode) under the influence of the magnetic field (so-called "magnetic mirror"). Due to the backward force induced by the solenoid field, the electrons have higher chance to hit the photocathode and to produce secondary electrons.

When the bucking solenoid is applied, the slope of the magnetic field gradient at the cathode is changed (see Fig. 6.4). Figure 6.11 shows simulation results for the solenoid configuration to compensate the magnetic field at the cathode. The area, where the multipacting can be generated, is larger than that for Fig. 6.10.

Multipacting at TTF1

Between the guns in operation at TTF1 and TTF2 exist two main differences: The type of the rf input coupler and position of the main solenoids. At TTF1, the rf

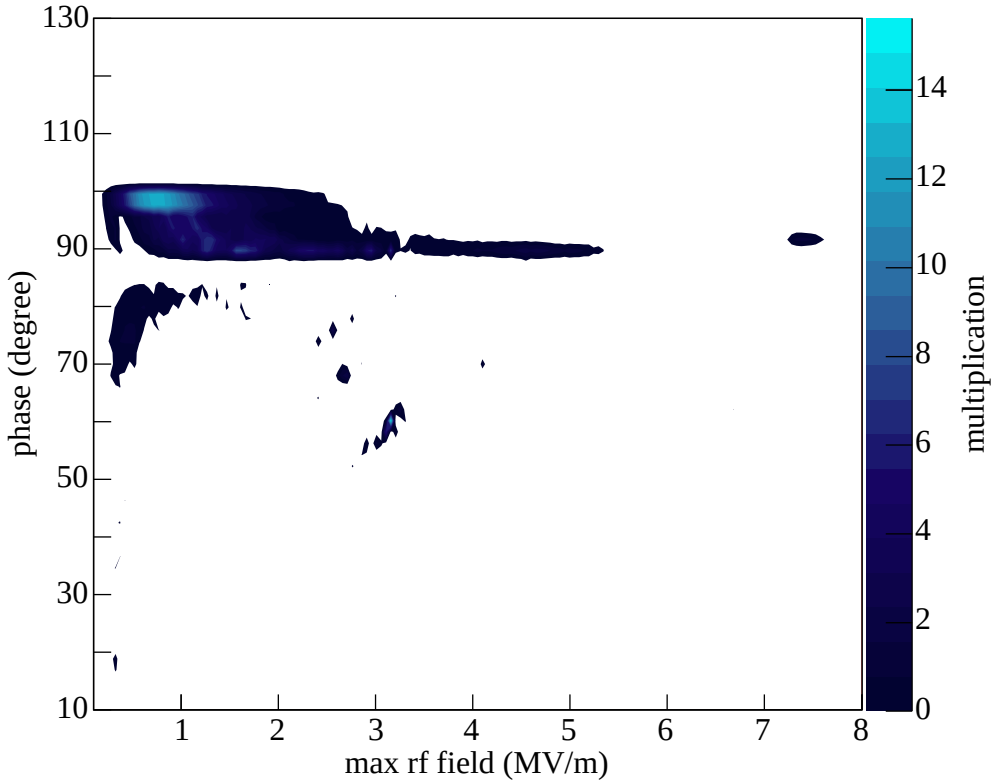

Figure 6.11: Electron multiplication as a function of the maximum rf field and the emission phase when the main and the bucking solenoid currents are set to 400 A and 30.5 A, respectively. Electron trajectory and secondary electron generation have been tracked for 100 rf cycles.

input coupler was installed at the side of the full cell of the gun cavity and two main solenoids were located 0.105 m and 0.2 m downstream from the cathode. At TTF2 and PITZ, the coaxial rf coupler is installed in the forward direction of the full cell of the gun cavity in order to make a cylindrical symmetry in the cavity and the main solenoid position moved to 0.278 m from the cathode in order to adapt the phase space of the beam to the injector booster position.

In Fig. 6.12, the magnetic field distribution at TTF1 is shown together with the rf field distribution and the gun aperture. The magnetic field compensation at the cathode was accomplished with a bucking solenoid with the same size as the main solenoid installed behind the cathode. Because the main solenoid was located near to the cathode, the slope of the solenoid field strength was steeper than at TTF2 and the influence of the magnetic mirror to the multipacting generation could be stronger. A simulation for the multipacting at TTF1 was made with assuming the three solenoid currents to be 250 A. Figure 6.13 shows the multiplication of the electrons, by means of the secondary electron generation at the cathode, as a

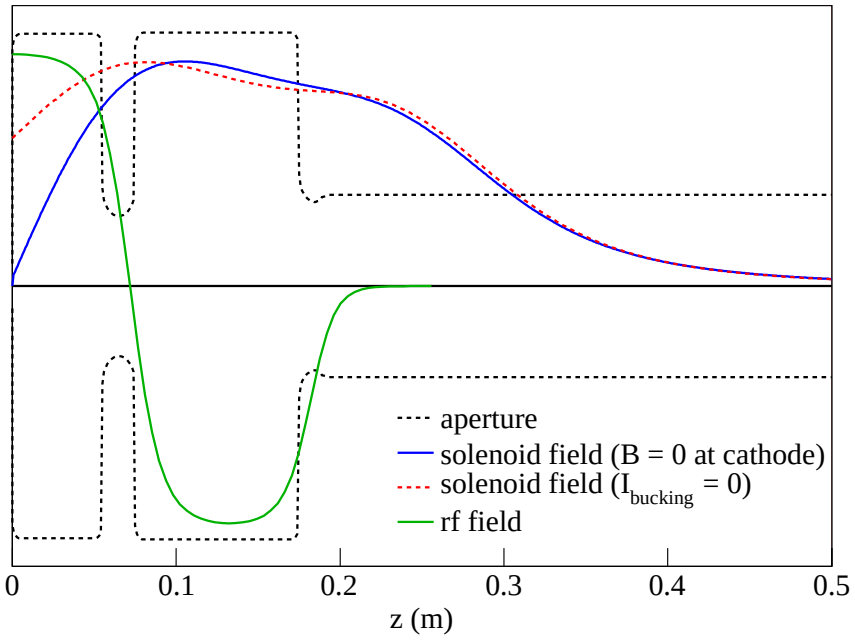

Figure 6.12: The solenoid field and the rf field with the gun aperture at TTF1.

function of the emission phase and the rf field of the seed electron. The area in which multipacting can take place is much larger than in the TTF2 or PITZ case, and the strength of the multiplication is also greater.

6.2.3 Multiplication of the field-emitted electron

The actual multipacting conditions integrate the effects due to the emission phase and the 3D distribution of the electrons, i.e. the 2D transverse and the temporal distribution of the seed electrons. In order to simulate the actual multipacting process occurring in the gun cavity, realistic distributions have to be used for the initial parameters.

For three different solenoid distributions, the multiplication has been numerically calculated as a function of the maximum rf field at the cathode for the conditions at PITZ. For these simulations, the time duration corresponding to 140 rf cycles (0.11 μs) has been used to calculate the electron generation and the dynamics. The main solenoid currents have been selected to be 0 A and 400 A. At 400 A, a maximum solenoid field of 0.235 T is present 0.276 m downstream from the cathode. The solenoid field configuration has been changed by controlling the bucking solenoid current. For the PITZ configuration, the effect of the longitudinal field at the cathode is small because the field of the main solenoid at the cathode is only 5% of the peak field (see Fig. 6.4). Nevertheless, the solenoid field at the cathode has a strong influence on the multipacting.

The simulation results in Fig. 6.14 show that the multiplication is strong at

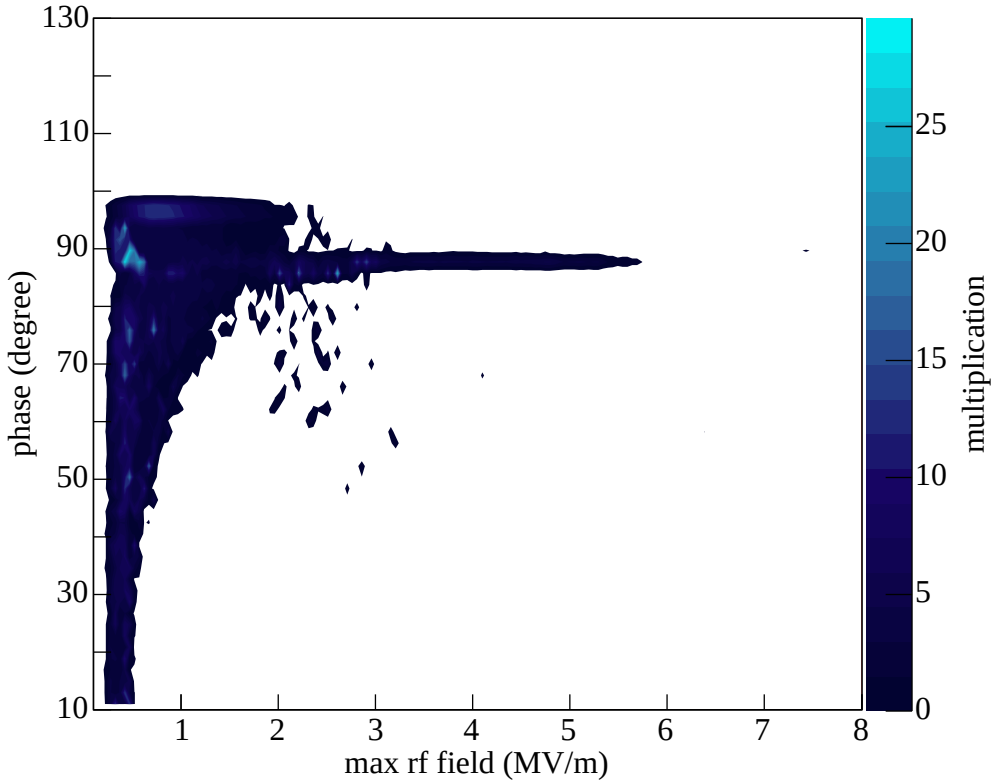

Figure 6.13: Electron multiplication at TTF1. The currents of the three solenoids have been set to 250 A for this simulation. Electron trajectories and secondary electron generation have been tracked for 100 rf cycles.

the compensation condition ($I_{\text{bucking}} = 30.5$ A) and negligibly weak at the other conditions (Fig. 6.14). In these simulation, 1000 seed electrons have been started with the same distribution used for the dark current simulation in Chap. 5. For the calculation of the multiplication, the time corresponding to 140 rf cycles has been used for the electrons tracking.

In Fig. 6.15, 1000 initial electrons have been numerically tracked for the time duration of 300 rf cycles with the rf field amplitude decaying with a decay time of 2.78 μs starting from 0.6 MV/m of the maximum field strength. The solenoid currents have been configured as 400 A for the main and 30.5 A for the bucking solenoids. For this simulation, the parameters for the secondary emission have been chosen as follows: $\delta_{\max} = 20$, $E_{p,\max} = 1$ keV, and $s = 2.2$. The simulation with the above parameters shows, on the average, an exponential increase of the number of electrons. Note, however, that the multiplication takes place in steps separated by many rf cycles. An estimation of the exponential growth rate requires the simulation of many rf cycles and is limited by the available computing power.

In Fig. 6.8, the multipacting peak grows up to the maximum of the peak during

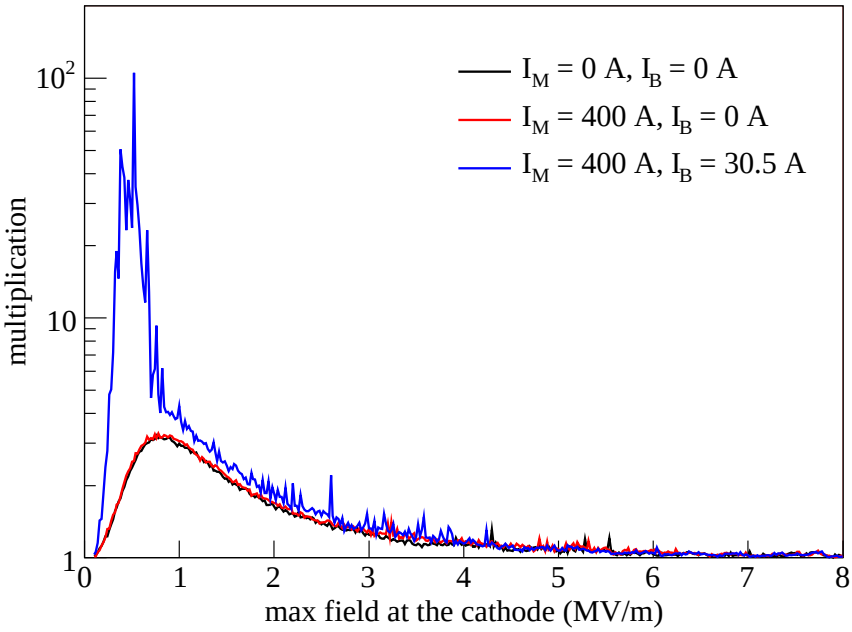

Figure 6.14: Multiplication after 140 rf cycles vs. the maximum field at the cathode for different main (I_{M}) and bucking (I_{B}) solenoids current.

about 1 μs. The time of 1 μs corresponds to 1300 rf cycles of the 1.3 GHz rf frequency. The time is long enough to generate a strong multipacting peak. The decay of the rf field, possibly enhanced by the beam loading of the electrons limits the development of the cascade.

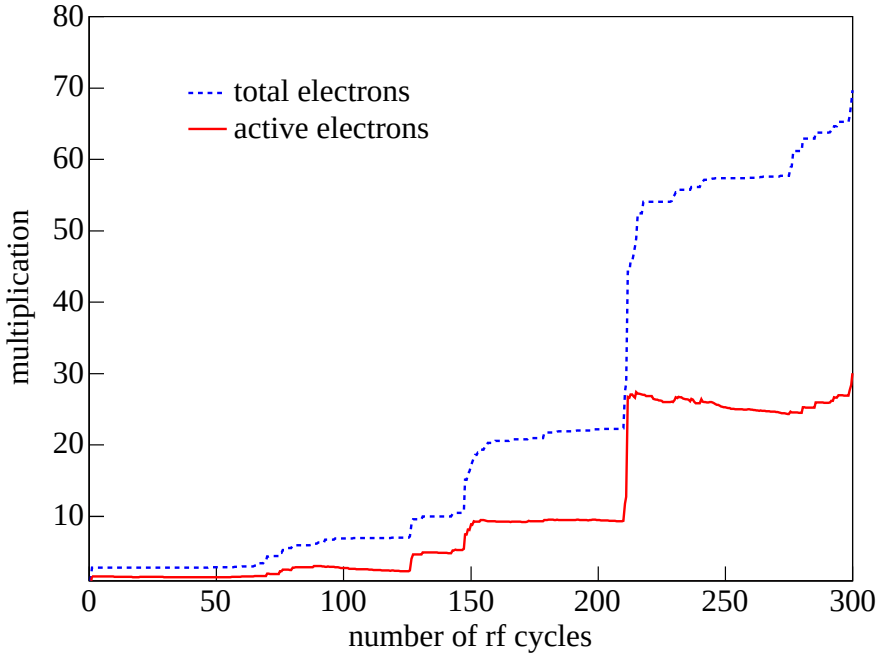

Figure 6.15: Multiplication for 300 rf cycles under the decaying rf field. The term of "total electrons" means the number of electrons which are either "active" or disappeared after hitting an aperture or generating secondary electrons.

Chapter 7

XFEL gun

In this chapter, expectations of the thermal emittance, the dark current, and the multipacting at the rf gun for the European XFEL project are made according to the discussions in the previous chapters.

7.1 Requirements

The parameters of electron beams required for the European XFEL are summarized in Table 7.1.

Table 7.1: Parameters of electron beams for the XFEL (from Ref. [79]).

parameter	value
beam energy	20 GeV
normalized emittance	1.4 mm mrad
electron bunch charge	1 nC
electron bunch length	80 fs
uncorrelated energy spread	2.5 MeV rms

The values in Table 7.1 must be achieved at the entrance of the undulator in order to produce self-amplification of spontaneous emission (SASE) FEL radiation. At the injector, tighter beam parameters are required because the electron beam will be degraded while passing though accelerator components, e.g. bunch compressors. The beam parameters required at the injector have been proposed by Ferrario et al. [80] and are summarized in Table 7.2. In Ref. [80], a constant kinetic energy of 0.55 eV for photoemitted electrons was assumed for the thermal emittance calculation. In order to achieve the beam parameters, the conditions of the rf gun have been optimized by Ferrario et al. [80] and the result is shown in Tabel 7.3.

Table 7.2: Parameters of electron beams for the injector (from Ref. [80]).

parameter	value
electron bunch charge	1 nC
normalized emittance	0.9 mm mrad

Table 7.3: Parameters of the photocathode rf gun for the XFEL (from Ref. [80]).

parameter	value
laser spot size (rms)	0.75 mm
thermal emittance	0.74 mm mrad
laser pulse length	20 ps
maximum field at the cathode	60 MV/m
emission phase	44°

7.2 Thermal emittance

The operating parameters for the XFEL gun were proposed by Ref. [80]: the rms size of the laser spot is 0.75 mm and the emission phase is 44° when the maximum field at the cathode is 60 MV/m.

For the gun parameters proposed in Ref. [80], the thermal emittance $\varepsilon_{\mathrm{meas}}^{\mathrm{therm}}$ can be estimated with the discussions in Sec. 4.1.4 and will be 0.99 mm mrad from Eqs. 4.2 and 4.8 when taking into account the discrepancy parameter η (Eq. 4.10). This thermal emittance is already higher than the emittance 0.9 mm mrad after the gun. Considering the discussion so far, the gun parameters for the XFEL injector must be re-optimized. The thermal emittance may be decreased with selecting a smaller laser spot size or perhaps with a new preparation procedure of the photocathode. For example, when the laser spot size is taken to be 0.45 mm rms, the thermal emittance $\varepsilon_{\mathrm{meas}}^{\mathrm{therm}}$ is expected to be 0.60 mm mrad. If we apply an improved treatment to reduce the surface roughness of the Mo plug and achieve a higher homogeneity of the QE of the emissive film, the discrepancy parameter η may decrease.

7.3 Dark current

Assuming that the same type of gun cavity and photocathode used for the PITZ or TTF2 guns will be used again for the XFEL gun, the dark current at the gun is estimated to be much higher than at the PITZ or TTF2 guns. Using Eq. 3.7, one expectation of the dark current for the XFEL gun has been made with an extrapolation of the measurement at the PITZ gun (Fig. 7.1). The dark current

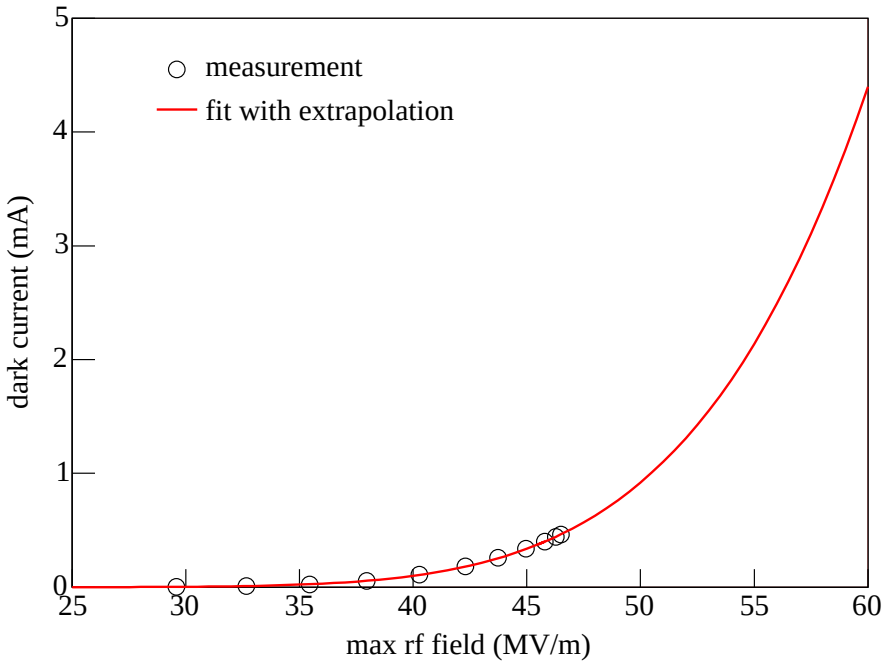

Figure 7.1: Dark current estimation for the XFEL gun with an extrapolation of the measurement at the PITZ gun.

measurement was performed with cathode #43.2 in cavity prototype #1, when both the cathode and the gun cavity were conditioned well (see the measurement in November 2004 in Fig. 5.17). The extrapolaton shows that the dark current at the XFEL gun will be as high as several mA. In this extrapolation, possible decrease of the dark current with rf conditioning was not considered.

Strong dark current may damage vacuum components, e.g. the photocathode, the gun cavity, the diagnostics, and the undulator magnets. A large fraction of dark current emitted at higher gradient can propagate downstream together with the electron beam. The optimum emission phase, satisfying the condition to make minimal transverse emittance, shifts to a higher phase for an increasing rf gradient because the phase slippage becomes smaller for higher rf gradients. The momentum gain of the electron beam for the two rf gradients are shown in Fig. 7.2 together with the normalized intensity distribution of field emission.

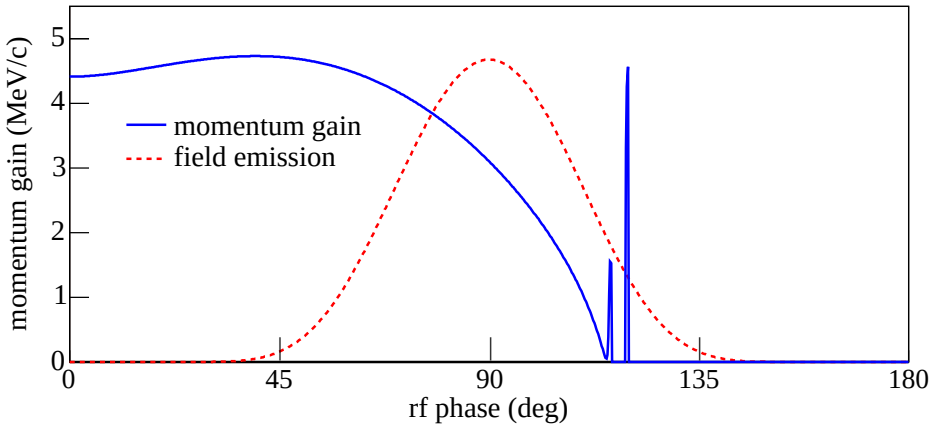

(a) 46.5 MV/m

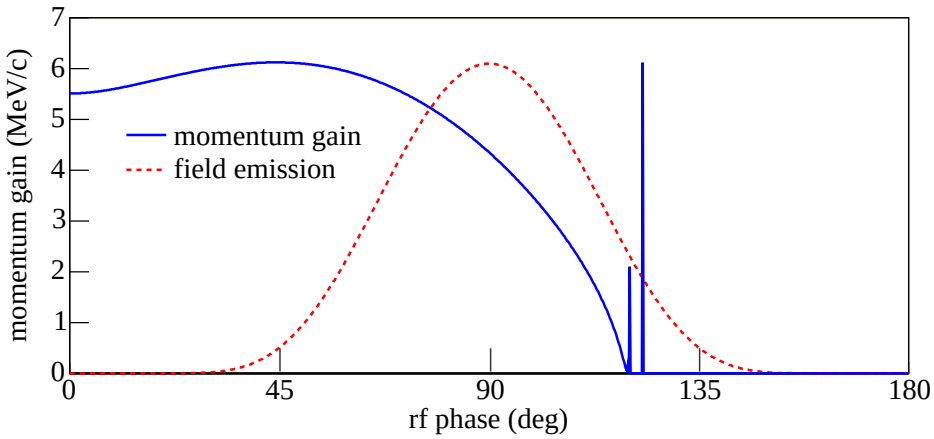

(b) 60 MV/m

Figure 7.2: Momentum gain of the electron beams for two rf gradients as a function of the emission phase. The momenta of a single electron have been plotted together with the normalized intensity distributions of field emission. For the intensity distributions a work function of 4.6 eV and a field enhancement factor of 200 are assumed (see Sec. 3.1).

Compared with the present PITZ gun, the optimum emission phase for the highest momentum gain, i.e. for the smallest transverse emittance, shifts nearer to an rf phase of 90°, where there is a highest chance for field emission. In addition, the emission phase of the dark current becomes broader for higher gradient (see Fig. 7.2). Therefore, a larger fraction of the dark current can overlap with the electron beam in the momentum spectrum (Fig. 7.3). The overlapping part can reach the first acceleration section and can be accelerated together with the electron bunches. This dark current can affect the vacuum components downstream.

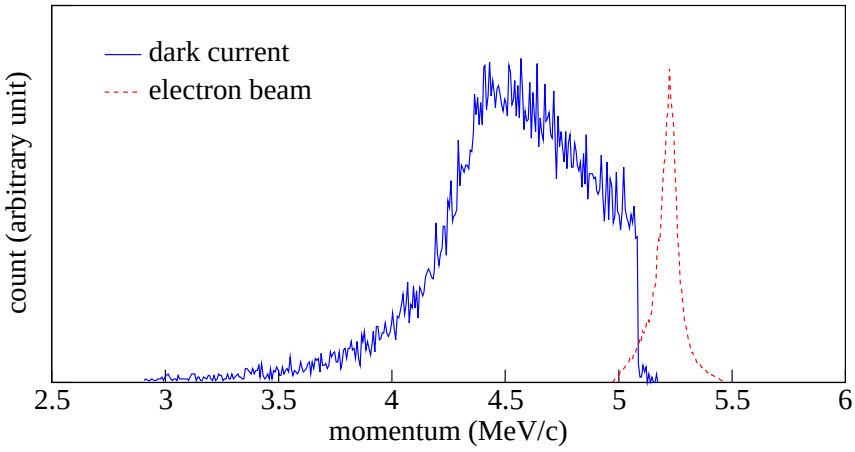

(a) 46.5 MV/m

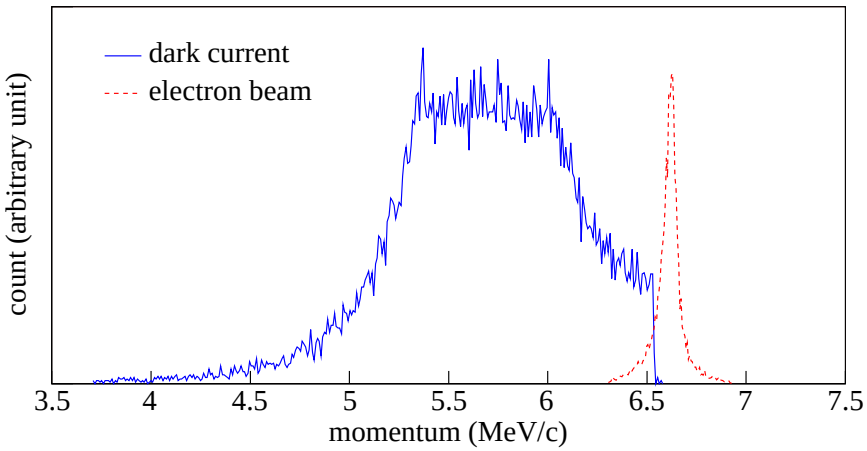

(b) 60 MV/m

Figure 7.3: Simulated momentum spectra of dark current and electron beam for two rf gradients. For the beam simulations, the design parameters of the laser pulse for the XFEL gun have been used [80]: a laser spot size of 0.75 mm rms, a laser pulse length of 20 ps assuming a rise/fall time of 2 ps.

7.4 Multipacting

Since the main solenoid for the XFEL gun will be moved farther from the cathode (0.4 m) [80], the tail of the main solenoid field at the cathode will be small. Therefore, the bucking solenoid current will be decreased for the solenoid field compensation at the cathode. As the result, the multipacting taking place at the cathode will be weaker than for the PITZ gun.

Chapter 8

Conclusion

Electron emission processes from the Cs_2Te photocathode change significantly their properties during the operations of rf gun cavities. Since the strong rf field decreases the potential barrier for the electron emission, or the electron affinity, the electron escape probability and the kinetic energy of the emitted electrons increase with the rf field strength. The increase of the electron escape probability with the field strength called the Schottky effect is modeled in ASTRA as a linear increase with the field strength. The model explains successfully measurements of bunch charge as a function of the emission phases. In order to relate the Schottky effect to the electron affinity variation, an improved model has been used and the coefficients in the equation have been found. With the improved model, the thermal emittance measurement data could be analyzed and the thermal emittance for the XFEL gun has been estimated.

A secondary electron emission algorithm has been modeled and implemented into ASTRA. The secondary emission model explains successfully the electron beam dynamics for electron bunches with low charge and short length. The measurement condition, low charge and short length beam, has been selected in order to reduce the space charge force and to study the dependence on the emission phase. For the normal operation condition of PITZ, an rf gradient over 40 MV/m and an emission phase about 35°, secondary emission does not influence the beam dynamics due to the high gradient. At such a gradient, the primary electron energy is too high to generate secondary electrons when impacting the cathode.

The dark current at the photocathode rf guns has the main origin in field emission from the photocathode and the surrounding backplane. The amount of the dark current depends strongly on the status of not only the cathode but also the gun cavity. After conditioning of the cavities, the dark current has been reduced by about one order of magnitude. The dark current sources have been investigated with the images on a screen downstream. The geometry of the cathode plug has been imaged on the screen clearly and the dimension of the dark current has been scaled by means of moving the laser spot position on the cathode front surface.

The multipacting peaks appear at the beginning and at the end of the rf pulse.

The multipacting appearing at the end of the rf pulse has been measured systematically and analyzed with ASTRA simulation. At very low rf gradient, about $1 \sim 2$ MV/m or even lower, the number of electrons can increase with secondary electron generation at the Cs_2Te photocathode because the cathode has a secondary emission yield greater than one. The solenoid field builds up a magnetic mirror and pushes electrons back to the cathode to incite the multipacting. Thus, the multipacting behavior changes depending on the solenoid configuration.

The European XFEL demands a challenge on the electron beam quality. In order to reach the requirement, a higher rf gradient is necessary. According to the model introduced in this thesis, the optimized gun parameters at present might induce too high thermal emittance due to the large laser spot size. Therefore, an improved optimization should be made with keeping the laser spot size smaller. The dark current at the gun will increase by one order of magnitude compared to the PITZ gun or the TTF guns. More detailed work to characterize the dark current source is on going with a collaboration with INFN Milano-LASA. The multipacting occurring at the cathode will be smaller at the XFEL gun because the main solenoid will be located farther from the cathode and will be less effective to the cathode.

Appendix A

Cathodes parameters

A.1 Specifications

The photocathode used at PITZ and TTF are made at INFN Milano-LASA. When the cathodes are produced, all informations of the preparation processes and the first QE measurement with a UV lamp are recorded at the cathode information website [12]. Some important information of the cathodes is summarized in Table A.1.

Table A.1: Photocathodes used at PITZ since 2003. The thickness t_{Cs_2Te} and the diameter ϕ_{Cs_2Te} of the Cs_2Te coating on the Mo plug front surface are summarized. The QE is measured at 254 nm of the photon wavelength. The "first to last use" indicates when the cathode was used at the first and at the last time.

cathode	type	t_{Cs_2Te} (nm)	ϕ_{Cs_2Te} (mm)	first to last use	QE_{Milan} (%)
34.3	Mo	–	–	Jan. '03 - Apr. '03	–
60.1	Cs_2Te	30	10	Apr. '03 - May '04	4.6
47.3	Mo	–	–	Sep. '03 - Aug. '04	–
61.1	Cs_2Te	20	5	Sep. '03 - Aug. '04	1.4
35.2	Cs_2Te	40	5	Sep. '03 - Aug. '04	11
500.1	Cs_2Te	60	5	Sep. '03 - Apr. '05	9.6
41.1	Mo	–	–	Sep. '04 - Apr. '05	–
43.2	Cs_2Te	30	5	Sep. '04 - Apr. '05	10.7
33.2	Cs_2Te	30	5	May '05 -	7.7
56.2	Mo	–	–	May '05 -	–
58.1	Cs_2Te	30	5	May '05 -	8.4
54.2	Cs_2Te	30	5	May '05 -	7.9

A.2 Aging of cathodes

When a Cs_2Te cathode is stored in the cathode chamber or in the cathode preparation chamber under ultra-high vacuum on the order of 10^{-11}, the QE does not decrease remarkably. When a Cs_2Te cathode is used for gun operation, the Cs_2Te film starts to be contaminated with molecules in the gun cavity and the QE decreases immediately. According to the study by di Bona *et al.* [15], CO_2 and O_2 have a poisoning effect reducing the QE. These molecules can be emitted from the surface of the Cu cavity when high rf power is applied to the cavity surface.

The QEs of two cathodes in the cathode chamber did not change within measurement error during a delivery from Milan to Zeuthen (see Table A.2). For the measurements a UV lamp with a 254 nm band pass filter was used for these measurements. The cathodes have been stored in the cathode chamber under ultra-high vacuum.

Table A.2: QE measurements of two cathodes (#54.2 and #58.1) at Milan (22 December 2004) and at Zeuthen (11 April 2005).

cathode	QE at Milan	QE at Zeuthen
# 54.2	8.1%	7.5%
# 58.1	10.2%	10.5%

In addition to the chemical poisoning effect of the Cs_2Te film, mechanical damages on the Cs_2Te film as well as on the front surface of the Mo plug have been observed (see Fig. A.1 b). The photographies have been taken by a digital camera through a view-port of the cathode chamber. In the cathode chamber, the cathodes are stored for a next use. With a manipulator, the cathodes can be selected and moved from the cathode chamber to the gun cavity.

After several months in use, the Cs_2Te cathodes became damaged mechanically as well as poisoned chemically. Two photographies of cathode #61.1 and #500.1 are shown in Fig. A.2. The photographies were taken after the last use at PITZ. A large part of the Cs_2Te film has disappeared with remaining holes and several pits have been made on the Mo plug (see Fig. A.2).

Figure A.3 a shows a damage of cathode #60.1 after one year use at gun prototype #2 and one week use at gun prototype #1. After two weeks operation at gun prototype #1, the cathode was damaged to a state which cannot be used to produce electron beams with a good quality anymore (Fig. 3 b). When cathode #60.1 was used, conditioning of gun prototype #1 started and the inner surface of the copper cavity was not ready for a stable operation.

Figures A.4 b and c show damages of Mo cathodes. Cathode #47.3 has been used for conditioning of gun prototype #1 and for a high rf power test at the same

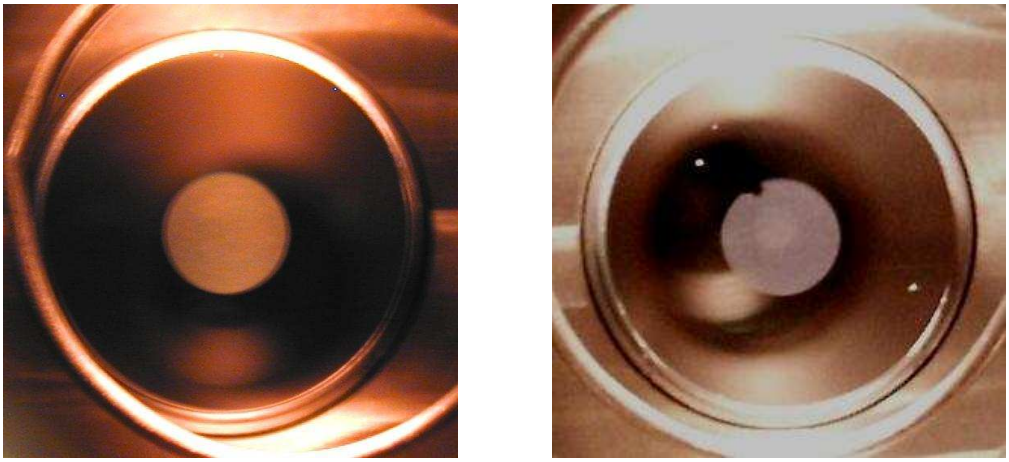

(a) (b)

Figure A.1: Photography of the front surface of cathode #43.2 (a) taken just after the Cs_2Te deposition at INFN Milano-LASA (in May 2004 at Milan) (b) after several months of use for producing electron beams in gun prototype #1 (in February 2005). The mirror-like Mo plug surface reflects the images of the view-port and the flange of the cathode chamber. The metal wire which is visible in the pictures is the anode installed for quantum efficiency measurement in the cathode chamber.

gun. Cathode #41.1 has been used also at the same gun but after the gun had been conditioned.

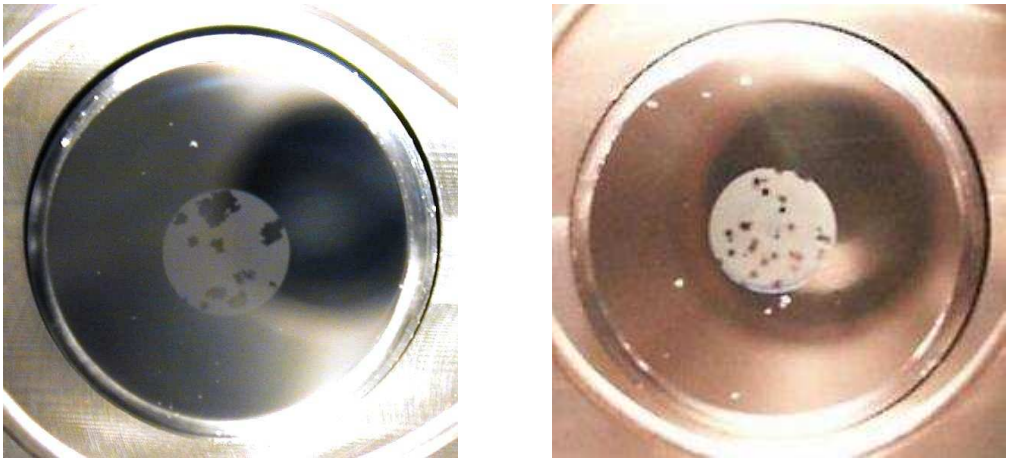

(a) (b)

Figure A.2: Photography of the front surface of cathode #61.1 (taken in October 2004 at Milan) and #500.1 (in February 2005) after the last use at PITZ.

(a) (b)

Figure A.3: Photography of the front surface of cathode #60.1 taken (a) in March 2004 and (b) after the last use. (The second photography was taken at Milan).

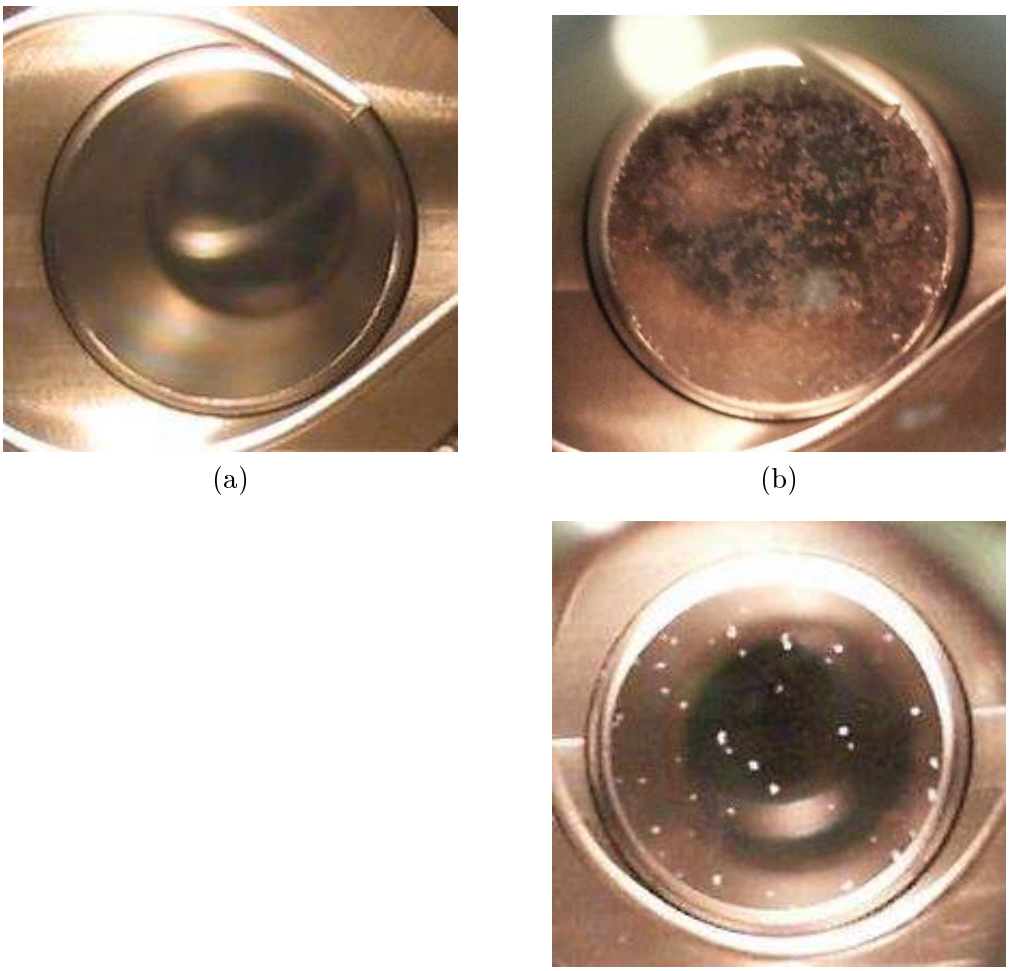

(a) (b)

(c)

Figure A.4: Mo cathode damage; (a) #47.3 when fresh (March 2004), (b) #47.3 contaminated with Copper color material (July 2004), (c) #41.1 mechanically damaged (February 2005).

Appendix B

An approximation of the Nordheim parameter

The Nordheim parameter y is defined by [29]

$$y \equiv \left(\frac{e^3}{4\pi\epsilon_0}\right)^{1/2} \frac{(\beta_{\rm field}E)^{1/2}}{\phi} = 3.795\times10^{-5}\,\frac{(\beta_{\rm field}E)^{1/2}}{\phi}. \tag{B.1}$$

The expression for $v(y)$ is [32]

$$v(y) = 2^{-1/2}\left[1+(1-y^2)^{1/2}\right]^{1/2}\left\{E(k^2) - y^2K(k^2)/\left[1+(1-y^2)^{1/2}\right]\right\}, \tag{B.2}$$

where

$$E(k^2) = \int_0^{\pi/2}\left(1-k^2\sin^2\phi\right)^{1/2}d\phi \quad \text{and} \quad K(k^2) = \int_0^{\pi/2}\left(1-k^2\sin^2\phi\right)^{-1/2}d\phi\,,$$

$$k^2 = 2\left(1-y^2\right)^{1/2}/\left[1+\left(1-y^2\right)^{1/2}\right].$$

In Table B.1, an approximation is made for $v(y)$ with a simpler form, $v_a(y) = 0.9632 - 1.065\,y^2$. This approximation fits well for $y = 0.25 \sim 0.65$, which is the working range of an L-band rf gun (assuming $\beta_{\rm field} \sim 100$). A different approximation can be found in Ref. [30].

Table B.1: Nordheim parameters with an approximation, $v_a(y) = 0.9632 - 1.065y^2$.

y	$v(y)$	$v_a(y)$	$t(y)^2$
0.00	1.0000	0.9632	1.0000
0.05	0.9948	0.9605	1.0021
0.10	0.9817	0.9525	1.0071
0.15	0.9622	0.9392	1.0140
0.20	0.9370	0.9206	1.0224
0.25	0.9068	0.8966	1.0317
0.30	0.8718	0.8673	1.0419
0.35	0.8323	0.8327	1.0530
0.40	0.7888	0.7928	1.0647
0.45	0.7413	0.7475	1.0771
0.50	0.6900	0.6969	1.0897
0.55	0.6351	0.6410	1.1029
0.60	0.5768	0.5797	1.1163
0.65	0.5152	0.5132	1.1301
0.70	0.4504	0.4413	1.1443
0.75	0.3825	0.3640	1.1589
0.80	0.3117	0.2815	1.1733
0.85	0.2379	0.1936	1.1882
0.90	0.1613	0.1004	1.2032
0.95	0.0820	0.0019	1.2182
1.00	0.0000	-0.1020	1.2336

Bibliography

[1] H. Wiedemann, *Particle accelerator physics II*, (Springer-Verlag, 1995).

[2] E. L. Saldin, E. A. Schneidmiller, and M. V. Yurkov, *The physics of free electron lasers*, (Springer-Verlag, 1999).

[3] M. V. Yurkov *et al.*, "Generation of GW Radiation Pulses from a VUV Free-Electron Laser Operating in the Femtosecond Regime," Phys. Rev. Lett. **88**, 104802 (2002).

[4] L. H. Yu *et al.*, "First Ultraviolet High-Gain Harmonic-Generation Free-Electron Laser," Phys. Rev. Lett. **91**, 074801 (2003).

[5] K. J. Kim, "Rf and space-charge effects in laser-driven rf electron guns," Nucl. Instr. and Meth. **A275**, 201 (1989).

[6] B. E. Carlsten, "New photoelectric injector design for the Los Alamos National Laboratory XUV FEL accelerator," Nucl. Instr. and Meth. **A285**, 313 (1989).

[7] K. Flöttmann, A Space Charge Tracking Algorithm (ASTRA), http://www.desy.de/~mpyflo/.

[8] L. Young and J. Billen, in *Proceedings of the 2003 Particle Accelerator Conference, Portland, OR, 2003* (IEEE, Piscataway, NJ, 2003), p. 3521.

[9] F. Stephan *et al.*, in *Proceedings of 26th International FEL Conference and 11th FEL Users Workshop, Trieste, Italy, 2004*, p. 347; more information available at PITZ homepage, http://desyntwww.desy.de/pitz/.

[10] M. Krassilnikov, R. Cee, and T. Weiland, "Impact of the rf-gun power coupler on beam dynamics," in *Proceedings of the 8th European Particle Accelerator Conference, Paris, France, 2002*, p. 1640.

[11] D. Sertore, P. Michelato, L. Monaco, S. Schreiber, J. H. Han, and A. Bonucci, "Review of the production process of TTF and PITZ photocathodes," in *Proceedings of the 2005 Particle Accelerator Conference, Knoxville, USA, 2005*, p. 671.

[12] Information on the photocathode is available at
`http://wwwlasa.mi.infn.it/ttfcathodes/`.

[13] S. Schreiber, P. Michelato, L. Monaco, and D. Sertore, "On the photocathodes used at the TTF photoinjector," in *Proceedings of the 2003 Particle Accelerator Conference, Portland, OR, 2003* (IEEE, Piscataway, NJ, 2003), p. 2071.

[14] P. Michelato, "Photocathodes for rf photoinjectors," Nucl. Instr. and Meth. **A393**, 455 (1997).

[15] A. di Bona, F. Sabary, S. Valeri, P. Michelato, D. Sertore, and G. Suberlucq, "Auger and X-ray photoemission spectroscopy study on Cs_2Te photocathodes," J. Appl. Phys. **80**, 3024 (1996).

[16] I. Will, G. Koss, and I. Templin, "The upgraded photocathode laser of the TESLA Test Facility," Nucl. Instr. and Meth. **A541**, 467 (2005).

[17] I. Will, "Results of the MBI group in August - September," presented at the PITZ cooperation meeting, September 2004 (unpublished).

[18] L. Staykov *et al.*, PITZ solenoids measurements (unpublished).

[19] *818J series energy detectors operator manual*, (Newport corporation, 1997).

[20] Hamamatsu Photonics, `http://www.hamamatsu.com`.

[21] D. Lipka, "Momentum And Momentum spread Analysis (MAMA)," PITZ Note 01-04, 2004.

[22] D. Lipka, *Untersuchungen zum longitudinalen Phasenraum an einem Photoinjektor für minimale Strahlemittanz*, Ph.D. thesis, Humboldt University, 2004.

[23] J. Rönsch, *Selected studies of the longitudinal phase space at the photo injector test facility at DESY Zeuthen*, Diploma thesis, Hamburg University, 2005.

[24] V. Miltchev, *Investigation on the transverse phase space at a photo injector for minimized emittance*, Ph.D. thesis, Humboldt University (to be published).

[25] R. H. Fowler and L. Nordheim, "Electron emission in intense electric fields," Proc. Roy. Soc. (London) A **119**, 173 (1928).

[26] L. Nordheim, "The effect of the image force on the emission and reflection of electrons by metals," Proc. Roy. Soc. (London) A **121**, 626 (1928).

[27] W. Schottky, "Über kalte und warme Elektronenentladungen," Z. Phyk. **14**, 63 (1923).

[28] R. Gomer, *Field emission and field ionization*, (American Institute of Physics, New York, 1993).

[29] R. G. Forbes, "Field emission: New theory for the derivation of emission area from a Fowler–Nordheim plot," J. Vac. Sci. Technol. B **17**, 526 (1999).

[30] R.H. Good and E. W. Müller, *Field Emission*, Vol. 21 of Handbuch der Physik, edited by S. Flügge (Springer, Berlin, 1959), pp. 176-231.

[31] C. A. Spindt, I. Brodie, L. Humphrey, and E. R. Westerberg, "Physical properties of thin-film field emission cathodes with molybdenum cones," J. Appl. Phys. **47**, 5248 (1976).

[32] R. E. Burgess, H. Kroemer, and J. M. Houston, "Corrected values of Fowler-Nordheim field emission functions $v(y)$ and $s(y)$," Phys. Rev. **90**, 515 (1953).

[33] S. K. Sekatskii and V. S. Letokhov, "Electron tunneling time measurement by field-emission microscopy," Phys. Rev. B **64**, 233311 (2001).

[34] J. W. Wang, "Some problems on rf breakdown in room temperature accelerator structure, a possible criterion," SLAC/AP - 51 (1986).

[35] J. W. Wang and G. A. Loew, "Field emission and rf breakdown in high-gradient room-temperature linac structures," SLAC-PUB-7684 (1997).

[36] H. B. Michaelson, "The work function of the elements and its periodicity," J. Appl. Phys. **48**, 4729 (1997).

[37] K. Flöttmann, "Note on the thermal emittance of electrons emitted by cesium telluride photo cathodes," TESLA FEL Reports 1997-01, 1997.

[38] R. A. Powell, W. E. Spicer, G. B. Fisher, and P. Gregory, "Photoemission studies of cesium telluride," Phys. Rev. B **8**, 3987 (1973).

[39] W. E. Spicer, "Photoemissive, Photoconductive, and Optical Absorption Studies of Alkali-Antimony Compounds," Phys. Rev. **112**, 114 (1958).

[40] S. Hüfner, *Photoelectron spectroscopy: Principles and Applications*, 3rd Ed., (Springer, 2003).

[41] T. Boutboul, A. Breskin, R. Chechik, A. Braem, and G. Lion, "Ultraviolet photoabsorption measurements in alkali iodide and caesium bromide evaporated films," J. Appl. Phys. **83**, 7896 (1998).

[42] W. E. Spicer and A. Herrera-Gómez, "Modern theory and application of photocathodes," SLAC-PUB-6306, 1993.

[43] L. Monaco (private communication).

[44] P. Michelato, L. Monaco, D. Sertore, and S. Schreiber, "First energy spectra obtained with a Time-Of-Flight (TOF) electron spectrometer on Cs_2Te photocathodes," in *Proceedings of the 2001 Particle Accelerator Conference, Chicago, IL, 2001* (IEEE, Piscataway, NJ, 2001), p. 2420.

[45] G. Ferrini, P. Michelato, and F. Parmigiani, "A Monte Carlo simulation of low energy photoelectron scattering in Cs_2Te," Solid State Commun. **106**, 21 (1998).

[46] M. S. Tyagi, *Introduction to semiconductor materials and devices,* (John Wiley & Sons, Inc., 1991).

[47] B. E. Foutz, S. K. O'Leary, M. S. Shur, and L. F. Eastman, "Transient electron transport in wurtzite GaN, InN, and AlN ," J. Appl. Phys. **85**, 7727 (1999).

[48] M. A. Furman and M. T. F. Pivi, "Probabilistic model for the simulation of secondary electron emission," Phys. Rev. ST Accel. Beams **5**, 124404 (2002).

[49] A. Shih, J. Yater, C. Hor, and R. Abrams, "Secondary electron emission studies," Appl. Surf. Sci. **111**, 251 (1997).

[50] A. H. Sommer, "Relationship between Photoelectric and Secondary Electron Emission, with Special Reference to the Ag–O–Cs (S–1) Photocathode," J. Appl. Phys. **42**, 567 (1971).

[51] N. Hilleret *et al.*, "The secondary electron yield of technical materials and its variation with surface treatments," in *Proceedings of the 2000 European Particle Accelerator Conference, Vienna, Austria, 2000*, (2000), p. 217.

[52] D. J. Gibbons, *Secondary Electron Emission*, Vol. 2 of Handbook of vacuum physics, edited by A. H. Beck (Pergamon Pres, Oxford, 1966), pp. 299-395.

[53] R. C. Alig and S. Bloom, "Electron-hole-pair creation energies in semiconductors," Phys. Rev. Lett. **35**, 1522 (1975).

[54] J. Schou, "Transport theory for kinetic emission of secondary electrons from solids," Phys. Rev. B **22**, 2141 (1980).

[55] T. Boutboul, A. Akkerman, A. Gibrekhterman, A. Breskin, and R. Chechik, "An improved model for ultraviolet- and x-ray-induced electron emission from CsI," J. Appl. Phys. **86**, 5841 (1999).

[56] G. Diemer and J. L. H. Jonker, "Time delay of secondary emission," Philips Res. Rep. **5**, 161 (1950).

[57] K. I. Grais and A. M. Bastawros, "A study of secondary electron emission in insulators and semiconductors," J. Appl. Phys. **53**, 5239 (1982).

[58] S. A. Schwarz, "Application of a semi-empirical sputtering model to secondary electron emission," J. Appl. Phys. **68**, 2382 (1990).

[59] S. H. Kong, J. Kinross-Wright, D. C. Nguyen, and R. L. Sheffield, "Cesium telluride photocathodes," J. Appl. Phys. **77**, 6031 (1995).

[60] D. Sertore, D. Favia, P. Michelato, L. Monaco, and P. Pierini, "Cesium telluride and metals photoelectron thermal emittance measurements using a time-of-flight spectrometer," in *Proceedings of the 9th European Particle Accelerator Conference, Lucerne, Switzerland, 2004*, p. 408.

[61] G. Suberlucq, "Development and production of photo cathodes for the CLIC test facility," in *Proceedings of 18th International FEL Conference and Users Workshop, Rome, Italy, 1996*, p. II-131.

[62] T. Thon and R. Wenndorff, (private communication).

[63] A. Akkerman, A. Gibrekhterman, A. Breskin, and R. Chechik, "Monte Carlo simulations of secondary electron emission from CsI, induced by 1∼10 keV x rays and electrons," J. Appl. Phys. **72**, 5429 (1992).

[64] S. Schreiber *et al.*, "Measurement of Space Charge Effects and Laser Pulse Length in the TTF RF Gun using the Phase Scan Technique," Proc. FEL 1999, Hamburg, Germany, 2000, p. **II**-69.

[65] C. I. Coleman, "Field-enhancement of photoemission from cesium telluride," Appl. Optics **17**, 1789 (1978).

[66] K. Flöttmann, "Some basic features of the beam emittance," Phys. Rev. ST Accel. Beams **6**, 034202 (2003).

[67] M. Krasilnikov *et al.*, "Beam-based procedures for rf guns," in *Proceedings of the 2005 Particle Accelerator Conference, Knoxville, TN, 2005*, p967.

[68] Y. Huang and Y. Miyahara, "Simulation on the emittance of the rf gun including the Schottky effect," in *Proceedings of the 18th Linac Conference, Geneva, Switzerland, 1996*, p. 872.

[69] Microwave Studio, CST GmbH.

[70] J. Han *et al.*, "Conditioning and high power test of the rf guns at PITZ," in *Proceedings of the 9th European Particle Accelerator Conference, Lucerne, Switzerland, 2004*, p. 357.

[71] J. H. Han, M. Krasilnikov, and K. Flöttmann, "Secondary electron emission in a photocathode rf gun," Phys. Rev. ST Accel. Beams **8**, 033501 (2005).

[72] D. Sertore, S. Schreiber, K. Zapfe, D. Hubert, and P. Michelato, "Dark current at TTFL rf-gun," Proc. FEL 2000, Durham, North Carolina, USA, 2001, p. **II**-19.

[73] U. Klein and D. Proch, "Multipacting in superconductor rf structures," in *Proceedings of the Conference of Future Possibilities for Electron Accelerators, Charlottesville, Va., 1979*, p. N1.

[74] A. L. Gilardini, "Multipacting discharges: Constant-k theory and simulation results," J. Appl. Phys. **78**, 783 (1995).

[75] A. J. Hatch and H. B. Williams, "Multipacting modes of high-frequency gaseous breakdown," Phys. Rev. **112**, 681 (1958).

[76] J. R. M. Vaughan, "Multipactor," IEEE Trans. Electron Devices **35**, 1172 (1988).

[77] W. Hartung *et al.*, "Photo-emission and field emission investigations," presented at the FNPL Advisory Committee, 2002 (unpublished).

[78] K. Flöttmann (private communication).

[79] The beam parameters of the European XFEL are described at `http://xfel.desy.de/`.

[80] M. Ferrario, K.Flöttmann, T. Limberg, B. Grigoryan, and Ph. Piot, "Conceptual design of the TESLA XFEL photoinjector," TESLA FEL Reports 2001-03, 2001.

Acknowledgments

I would like to thank my advisors Jörg Roßbach and Peter Schmüser for their continued encouragement and helpful advice.

I specially thank Klaus Flöttmann for his encouragement and support on numerical calculations and Mikhail Krasilnikov for his helpful discussions. I am indebted to all of PITZ members, Siegfried Schreiber (DESY, Hamburg) and Michael von Hartrott (BESSY) for their experimental support. I thank Paolo Michelato, Laura Monaco and Daniele Sertore (INFN Milano-LASA) for the cathode preparation.

I am very grateful to Klaus Flöttmann, Mikhail Krasilnikov, Jörg Roßbach, Peter Schmüser, Siegfried Schreiber and Frank Stephan for their careful reading of my manuscript and for several valuable suggestions. I am also grateful to Juliane Rönsch for her help to translate the English abstract to the German one.

Finally, I want to thank my family for their patience and encouragement.